



Polyacrylonitrile-derived nanostructured carbon materials

Maciej Kopeć^{a,1}, Melissa Lamson^a, Rui Yuan^a, Chuanbing Tang^b, Michał Kruk^{c,d}, Mingjiang Zhong^e, Krzysztof Matyjaszewski^{a,*}, Tomasz Kowalewski^{a,*}



^a Center for Macromolecular Engineering, Department of Chemistry, Carnegie Mellon University, 4400 Fifth Avenue, Pittsburgh, PA 15213, USA

^b Department of Chemistry and Biochemistry, University of South Carolina, Columbia, SC 29208, USA

^c Department of Chemistry, College of Staten Island, City University of New York, 2800 Victory Boulevard, Staten Island, NY 10314, USA

^d Ph.D. Program in Chemistry, the Graduate Center of the City University of New York, 365 5th Avenue, New York, NY 10016, USA

^e Department of Chemical and Environmental Engineering, Yale University, 17 Hillhouse Avenue, New Haven, CT 06511, USA

ARTICLE INFO

Article history:

Received 2 May 2018

Received in revised form 29 January 2019

Accepted 10 February 2019

Available online 16 February 2019

Keywords:

Polyacrylonitrile

Controlled radical polymerization

Block copolymers

Templated synthesis

Nitrogen-doped nanocarbons

ABSTRACT

An overview on polyacrylonitrile (PAN)-derived carbon nanomaterials is presented. Controlled synthesis of well-defined PAN by reversible deactivation radical polymerization (RDRP) techniques is discussed as a route to tailored carbon precursors of various architectures, such as block copolymers (BCPs) and organic-inorganic hybrids. Primary examples of different approaches to templating include the use of PAN-containing BCPs self-assembled on planar surfaces or in solution to yield: (i) bulk carbon films, (ii) discrete nano-objects and (iii) mesoporous copolymer-templated nanocarbons (CTNCs). Inorganic templates or electrospinning as a viable approach to ordered mesoporous carbons or carbon nanofibers are also discussed. Special attention is devoted to nitrogen doping in PAN-derived partially graphitic carbons and to the evaluation of nitrogen-enriched nanocarbons in energy conversion and storage applications such as supercapacitors, lithium-sulfur batteries, electrocatalysts, solar cells or CO₂ sorbents.

© 2019 Elsevier B.V. All rights reserved.

Abbreviations: AGET, activators generated by electron transfer; AIBN, azobisisobutyronitrile; AN, acrylonitrile; ANT, acrylonitrile telomer; ARGET, activators regenerated by electron transfer; ATRP, atom transfer radical polymerization; BCCDP, 1,4-[2-(carbazole-9-carbodithioate)-2-methyl propionic acid] phenyl ester; BET, Brunauer-Emmet-Teller; BiB, 2-bromoisobutyrate; BPN, 2-bromopropionitrile; bpy, 2,2'-bipyridine; BTBDS, bis(thibenzoyl) disulfide; BTPADS, bis(thiophenylacetoyl) disulfide; CE, counter electrode; CED, 2-cyanoethyl dithiobenzoate; CEDT, cyanoethyl dodecyl trithiocarbonate; CEF, Chain end functionality; C_g, specific capacitance; CNF, carbon nanofiber; CPAD, 4-cyano-4-(phenylcarbonothioylthio)pentanoic acid; CPDB, 2-cyanoprop-2-yl dithiobenzoate; CPDT, 2-cyano-2-propyl dodecyl trithiocarbonate; CPN, 2-chloropropionitrile; CRP, controlled radical polymerization; C_s, surface specific capacitance; CTA, chain transfer agent; CTNC, copolymer-templated nanocarbon; CV, cyclic voltammetry; CVD, chemical vapor deposition; DBTC, dibenzyl trithiocarbonate; DCDPS, 2,3-dicyano-2,3-diphenylsuccinate; DCDPS, 2,3-dicyano-2,3-diphenylsuccinate; DLS, dynamic light scattering; DMAA, dimethylacetamide; DMF, dimethylformamide; DMP, 2-dodecylsulfanylthiocarbonylsulfanyl-2-methyl propionic acid; DMSO, dimethyl sulfoxide; DP, degree of polymerization; DSC, differential scanning calorimetry; EBiB, 2-bromoisobutyrate; EBPA, ethyl α-bromophenylacetate; EC, ethylene carbonate; EDLC, electrical double layer capacitor; EDX, energy dispersive X-ray spectroscopy; EIS, electrochemical impedance spectroscopy; EMIM-BF4, 1-ethyl-3-methylimidazolium tetrafluoroborate; FF, fill factor; FT-IR, Fourier-transform infrared; FTO, fluorine-doped tin oxide; GC, glassy carbon; GISAXS, grazing incidence small-angle X-ray scattering; GO, graphene oxide; GPC, gel permeation chromatography; HER, hydrogen evolution reaction; HOMO, highest occupied molecular orbital; ICAR, initiators for continuous activator regeneration; IMA, iminodiacetic acid; IMA, iminodiacetic acid; IPA, isophthalic acid; K-L, Koutecky-Levich; LiPS, lithium polysulfides; LSV, linear sweep voltammograms; LUMO, lowest unoccupied molecular orbital; MA, methyl acrylate; MALDI-TOF, matrix-assisted laser desorption ionization - time-of-flight mass spectrometry; MALLS, multi-angle light scattering; MBSC, 4-methoxybenzenesulfonyl chloride; Me₆TREN, tris[2-dimethylamino]-ethyl] amine; MMA, methyle methacrylate; MSC, methanesulfonyl chloride; MW, molecular weight; MWCNT, multi-walled carbon nanotubes; MWD, molecular weight distribution; NDC, nitrogen-doped carbon; NMP, nitroxide mediated polymerization; NMR, nuclear magnetic resonance; NPs, nanoparticles; OER, oxygen evolution reaction; OMC, ordered mesoporous carbons; ORR, oxygen reduction reaction; PAA, poly(acrylic acid); PBA, poly(n-butyl acrylate); PCBM, phenyl-C₆₁-butyric acid methyl ester; PCE, power conversion efficiency; PEO, poly(ethylene oxide); Ph-PTZ, 10-phenyl-phenothiazine; PMDETA, 1,1,4,7,7-pentamethyldiethylenetriamine; PMMA, poly(methyl methacrylate); PPh₃, triphenylphosphine; PS, polystyrene; Pt/C, platinum on carbon; PtBA, poly(t-butyl acrylate); RAFT, reversible addition fragmentation transfer; R_{CT}, charge transfer resistance; RDE, rotating disk electrode; RDRP, reversible deactivation radical polymerization; RHE, reversible hydrogen electrode; RI, refractive index; SARA, supplemental activator reducing agent; SAXS, small-angle X-ray scattering; SCK, shell cross-linked micelle; SEC, size exclusion chromatography; SEM, scanning electron microscopy; SG-1, n-tert-butyl-1-diethylphosphono-2,2-dimethylpropyl nitroxide; SI-ATRP, surface-initiated atom transfer radical polymerization; SPAN, sulfurized polyacrylonitrile; SSA, specific surface area; TEM, transmission electron microscopy; TEMPO, 2,2,6,6-tetramethyl-1-piperidinyloxy; TGA, thermogravimetry; TMG3-TREN, tetramethylguanidino-tris(2-aminoethyl)amine; TMSC, trichloromethanesulfonyl chloride; T_p, pyrolysis/carbonization temperature; TPMA, tris[(2-pyridyl)methyl]amine; TPPA, 2,2,5-trimethyl-3-(1-phenylethoxy)-4-phenyl-3-azahexane; V-70, 2,2'-azobis(4-methoxy-2,4-dimethylvaleronitrile); VA-NCTN, vertically-aligned N-doped nanotubes; XPS, X-ray photoelectron spectroscopy; XRD, X-ray diffraction.

* Corresponding authors.

E-mail addresses: km3b@andrew.cmu.edu (K. Matyjaszewski), tomek@andrew.cmu.edu (T. Kowalewski).

¹ Current address: Materials Science and Technology of Polymers, MESA+ Institute for Nanotechnology, University of Twente, P.O. Box 217, 7500 Enschede, the Netherlands.

Contents

1. Introduction	90
1.1. Nanocarbons	90
1.2. Heteroatom-doped nanocarbons	90
1.3. Polymer-derived nanocarbons	91
1.4. Polyacrylonitrile (PAN) as carbon precursor	92
2. Controlled synthesis of PAN	94
2.1. Conventional radical and anionic polymerization	94
2.2. Reversible deactivation radical polymerization (RDRP)	94
2.3. RDRP of acrylonitrile	95
2.3.1. Atom transfer radical polymerization (ATRP)	95
2.3.2. Activator regeneration methods for ATRP	95
2.3.3. Reversible addition fragmentation transfer (RAFT) polymerization	97
2.3.4. Nitroxide-Mediated Polymerization (NMP)	99
2.3.5. Cobalt-mediated radical polymerization (CMRP)	99
2.4. Random copolymerization of acrylonitrile	99
2.5. Synthesis of PAN block copolymers	99
2.5.1. ATRP	99
2.5.2. RAFT and NMP	101
2.6. Grafting from surfaces	102
3. Templating PAN to form Nanocarbons	102
3.1. Nanostructured carbon films	102
3.2. Discrete carbon nanoobjects	106
3.3. Carbon nanofibers	107
3.4. Bulk mesoporous carbons	107
3.4.1. Hard templating	108
3.4.2. Soft templating: copolymer-templated nanocarbons (CTNC)	114
4. Applications of PAN-Derived nitrogen-enriched nanocarbons	116
4.1. Supercapacitors	116
4.2. Li-S batteries	121
4.3. Electrocatalysis	124
4.3.1. Oxygen reduction reaction (ORR)	124
4.3.2. Hydrogen evolution reaction (HER)	125
4.3.3. Dye-Sensitized Solar Cells (DSSCs)	126
4.4. CO ₂ utilization and heavy metal adsorption	126
5. Summary	129
Acknowledgements	129
References	129

1. Introduction

1.1. Nanocarbons

Carbon is not only the main element responsible for the existence of life on Earth, but is also an essential engineering material with countless technological applications. Among the variety of known allotropes of carbon, the sp²-bonded phase (graphite) is stable at ambient conditions, whereas at high pressures and temperatures sp³-hybridized configuration (diamond) becomes thermodynamically favored [1].

Modern carbon science was revolutionized with the discovery of highly oriented pyrolytic graphite (HOPG), carbon fibers from polyacrylonitrile (PAN) and nanocarbons, namely fullerenes [2], carbon nanotubes [3], and graphene [4], which became one of the most studied materials of the past few decades.

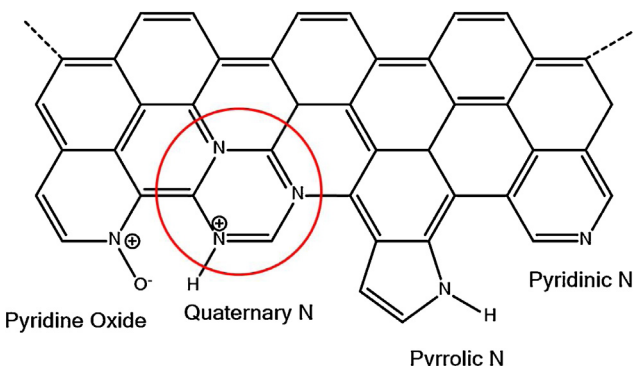
The electronic properties of carbon nanomaterials, i.e. tunable bandgap and excellent conductivity spurred tremendous interest in applications such as solar cells [5,6], transistors and logic circuits, [7,8] supercapacitors or electrodes [9–12]. Furthermore, a unique density of states at Fermi level arises at the zigzag edges of nanographene, which are not observed for armchair edges [1]. The non-bonding character of these states and high HOMO (highest occupied molecular orbital) electron density at zigzag edges can be a source of (electro)chemical activity of nanocarbons [13].

1.2. Heteroatom-doped nanocarbons

Introduction of heteroatoms into the graphitic network significantly alters the electronic properties of nanocarbons. The majority of the recent research has been focused on nitrogen-doped carbons (NDC), however other heteroatoms such as boron, sulfur and phosphorus have also gained considerable attention [14–21].

Nitrogen atoms act as electron-rich defects in graphitic sp² network, providing the ability to tune the material's conductivity and electronic band structure. Usually, the total nitrogen content decreases with pyrolysis temperature (T_p) due to fusion of graphitic domains which removes edge nitrogen functionalities. The maximal nitrogen content in NDC prepared at different T_p , regardless of precursor used was calculated to be 14.32 and 21.66 wt % for NDC's prepared at temperatures of 1000 and 900 °C, respectively [22]. More importantly however, nitrogen can be incorporated in the graphitic network as pyridinic, graphitic (quaternary), pyrrolic, and oxidized species (Scheme 1). The properties of pyridinic and graphitic nitrogens are of particular interest; specifically, edge-site pyridinic N atoms localized at zigzag edges of nanographitic domains also possess non-bonding lone electron pair with the Fermi level shifted more electronegatively, enhancing catalytic activity of NDC [14,23,24].

Indeed, the recent worldwide interest in heteroatom-doped nanocarbons was triggered by the identification of catalytic activi-



Scheme 1. Possible types of nitrogen atoms in N-doped carbons.

ity towards oxygen reduction reaction (ORR) in vertically-aligned N-doped nanotubes (VA-NCTN) by Dai et al. in 2009 [25]. For the first time a metal-free electrocatalyst was shown to surpass activity of the state-of-the-art Pt/C electrodes. Importantly, ORR is a key process behind the fuel cell technology, whose commercial development has been hindered due to the high cost of Pt. VA-NCTN catalyzed ORR via a four-electron mechanism, as desired in fuel cells, as well as provided superior stability and resistance to CO poisoning compared to Pt/C. Hundreds of reports followed this work demonstrating ORR catalyzed by various types of NDC, such as graphene or ordered mesoporous carbons [17,20]. The proposed mechanism suggested partially oxidized carbon atoms adjacent to nitrogen dopants as active sites for adsorption of oxygen molecules. This mechanism has been recently confirmed and carbon sites adjacent to pyridinic and, to a lesser extent, graphitic nitrogen atoms were determined to be the most catalytically active [26].

Successful utilization of NDC in ORR catalysis launched extensive studies on their electrochemical processes catalyzed by NDC in a metal-free fashion; the most prominent examples include hydrogen evolution reaction (HER), [27–29] oxygen evolution reaction (OER) [30], and CO₂ reduction [31–34]. Additionally, NDC materials have been used as molecular supports for metals, such as Fe, Co or Ni, taking advantage on their strong coordination with nitrogen atoms. Such noble-metal-free electrocatalysts were found to exhibit superior performance in ORR [17,35,36] as well as HER [37].

Supercapacitors are another emerging application of NDCs. The pyridinic N-functionalities are able to participate in Faradaic redox reactions, thus introducing pseudocapacitance to the materials which significantly contributes to the overall capacitance [38,39]. N-doped mesoporous carbon-based supercapacitors with capacitance as high as 855 F/g have been reported [40].

Main approaches to synthesize NDC include: 1) chemical vapor deposition (CVD) using nitrogen-rich precursors (e.g. mixture of CH₄ and NH₃) to grow N-doped graphene layers over a solid (typically metal) support, 2) post-treatment by annealing of pre-prepared (nano)carbon with a nitrogen-rich compounds, e.g. NH₃ or melamine, and 3) pyrolysis of nitrogen-containing precursors, such as polymers or biomass [14,15,18,19,41].

1.3. Polymer-derived nanocarbons

Over the past few decades polymers have become widely used carbon precursors [42,43]. Particularly, self-assembly of block copolymers (BCPs) has been intensively investigated due to variety of accessible morphologies, such as spheres, cylinders, lamellae or gyroids. In 2002, it was demonstrated that self-assembled BCPs containing nitrogen-rich polyacrylonitrile (PAN) could be transformed into well-defined nanostructured carbons, which is the

focus of the current review (see Section 3) [44]. Here, a few examples of other polymer precursors to carbon nanomaterials are presented.

In 2004, highly ordered mesoporous nanocarbons synthesized using BCPs were reported (Fig. 1) [45]. The approach involved the preorganization of resorcinol monomers in a well-ordered polystyrene-*b*-poly(4-vinylpyridine) (PS-*b*-P4VP) film. This was followed by the *in situ* polymerization of the resorcinol monomers with formaldehyde vapor to form ordered nanostructured resorcinol-formaldehyde resin (RFR). Upon carbonization, the nanostructured RFR was transformed into a highly ordered nanoporous carbon film whereas the PS-*b*-P4VP template was simultaneously decomposed.

This process was extended to synthesize mesoporous carbons using poly(ethylene oxide)-*b*-poly(methyl methacrylate)-*b*-polystyrene (PEO-*b*-PMMA-*b*-PS) triblock copolymers to template RFR resins [46]. After carbonization and removal of the PEO-*b*-PMMA-*b*-PS the carbon material had a specific surface area up to 900 m²/g and tunable wall thickness, depending on the resol to template ratio. Poly(isoprene)-*b*-polystyrene-*b*-poly(ethylene oxide) (PI-*b*-PS-*b*-PEO) triblock copolymers that phase separate into a gyroidal morphology were used to template phenol-formaldehyde resins [47]. After carbonization and removal of the triblock copolymer template, the carbons also exhibited a gyroidal morphology. Using a solvent processing technique, gyroidal gradients could be formed from PI-*b*-PS-*b*-PEO and gradient carbons were templated [48]. More recently, mesoporous carbon nanoparticles were prepared from PEO-*b*-PS to template nanostructured RFR [49]. Based on the size of the PEO-*b*-PS block copolymer, the size of the mesoporous carbon particles could be tuned. After carbonization and removal of PEO-*b*-PS the carbon nanoparticles with surface areas up to 646 m²/g were obtained. A vast family of carbons based on phenol-formaldehyde resins and other related compositions was synthesized using Pluronic block copolymers (PEO-PPO-PEO) [50–52].

PS-*b*-PVP BCPs were also directly used as carbon precursors, due to the high Flory-Huggins interaction parameter between the two blocks ensuring efficient microphase separation [53–56]. PS-P2VP was employed to obtain inverted micelles with P2VP cores and PS shells, which were crosslinked by UV light and pyrolyzed at 600 °C in argon. SEM and AFM analysis revealed that spherical morphology of the self-assembled film was well-preserved after carbonization. The size of the micelles decreased from 50 nm to 35–40 nm and the overall thickness of the film was reduced from 24 to 7 nm, due to decomposition of the PS segments and yielded arrays of carbon nanodots (Fig. 2). Additionally, by using selective solvents, the morphology of the self-assembled BCP could be reorganized into hexagonal arrays of ‘nanopits’ and also used as precursor to carbon films [53].

A similar strategy was used to prepare carbon-TiO₂ nanoparticle (NP) composite films by combining PS-*b*-P4VP micelles with sol-gel TiO₂ precursors [54]. Upon UV crosslinking and calcination, arrays of TiO₂ NPs embedded in carbon matrix were created. Application of the obtained materials as intermediate layers in a dye-sensitized solar cell (DSSC) significantly increased power conversion efficiency due to improved charge transfer at the TiO₂/carbon composite interface.

Other nitrogen-containing conjugated polymers were also used as NDC precursors [57]. Polyaniline (PANI) due to the presence of phenyl rings can carbonize into graphitic structures resulting in formation of well-defined carbon. A template-free method to polymerize aniline into PANI hydrogel crosslinked with phytic acid, which upon freeze-drying formed an aerogel foam was presented [58]. Carbonization of such aerogel structure resulted in N, P-co-doped mesoporous carbons (NPMC) with surface areas exceeding 1600 m²/g. The obtained NPMCs were then demonstrated to exhibit

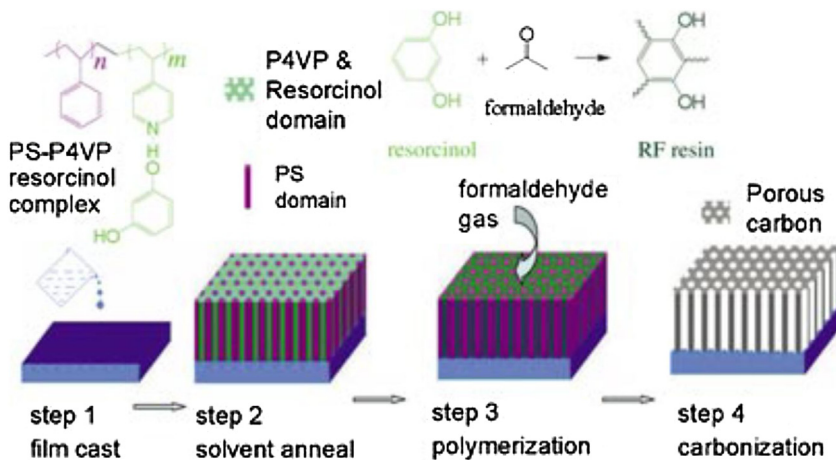


Fig. 1. Preparation of well-defined porous carbon nanostructures. Step 1: film casting of PS-P4VP/resorcinol supramolecular assembly; Step 2: solvent annealing; Step 3: *in situ* polymerization of resorcinol and formaldehyde by exposing the film to formaldehyde gas; Step 4: pyrolysis of the polymeric film in N₂. [45]. Copyright 2004. Reproduced with permission from John Wiley and Sons.

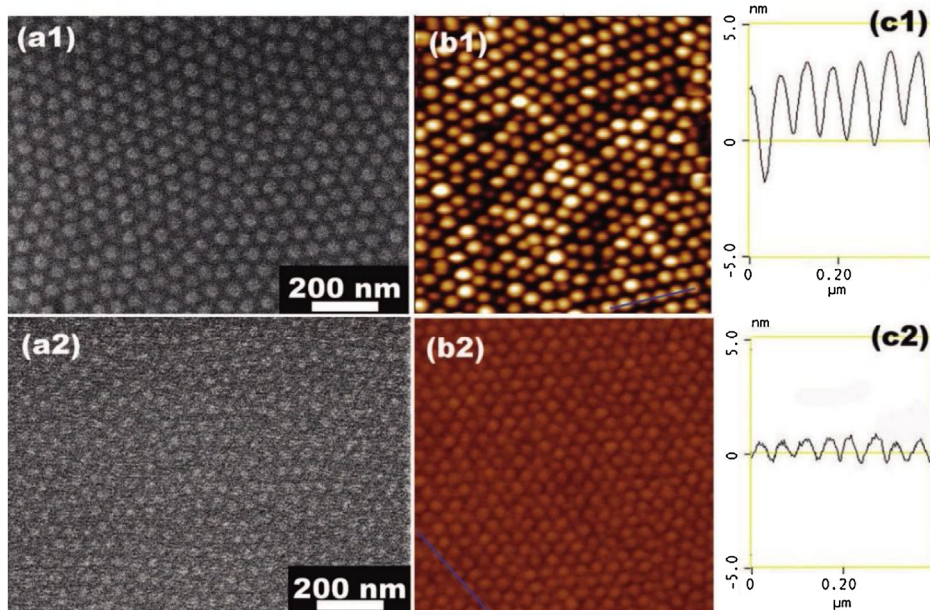


Fig. 2. Reverse PS-b-P2VP micelle films prior to and after carbonization at 600 °C. (a1) SEM image, (b1) AFM topography image, and (c1) apparent topographic AFM profile taken along the line in (b1) of as-casted reverse PS-b-P2VP micelle films; (a2) SEM image, (b2) AFM topography image, and (c2) apparent topographic AFM profile taken along the line in (b2) of a carbonaceous film obtained by stabilization and carbonization of a reverse PS-b-P2VP micelle film. For both AFM images the scan size is 1 μm × 1 μm, and the height scale is 20 nm. [53]. Copyright 2008. Reproduced with permission from American Chemical Society.

excellent performance as bi-functional catalysts in ORR and OER as well as cathodes in rechargeable zinc-air batteries.

Template-free interfacial copolymerization of aniline and pyrrole in micelles with Triton X-100 as a surfactant was utilized to form polyaniline-co-polypyrrole (PACP) hollow spheres. Upon pyrolysis hollow carbon nanospheres (HCN) with outer diameter of 69 nm were obtained and found to exhibit ultrahigh surface area exceeding 3000 m²/g (Fig. 3) [59]. Excellent performance of HCNs as organic vapor sorbents, supercapacitors and cathodes in lithium-sulfur (Li-S) batteries were then shown. This approach was recently extended by employing copolymerization-induced self-assembly of PACP in the presence of PEO-b-PS as a template [60]. Hydrogen bonding between PACP and the PEO block organized the template into micelles that allowed formation of spherical morphologies that upon carbonization yielded nitrogen-doped carbon nanospheres with ultrahigh surface area.

1.4. Polyacrylonitrile (PAN) as carbon precursor

Carbon fibers are commonly used engineered carbons due to their excellent mechanical properties, resulting from the highly oriented graphitic planes aligned along the fiber axis. Outstanding strength, modulus, resistance to high temperatures, as well as low weight make carbon fiber composites superior materials for aerospace and automotive applications [61]. PAN is the most important carbon fiber precursor due to its high carbonization yield, fiber-forming properties and unique thermal chemistry that allows synthesis of large graphitic planes upon pyrolysis. Overall, PAN accounts for 90% of global carbon fiber production.

PAN was first synthesized in 1930 by IG Farben, but was not commercially utilized until the late 50s due to its unusual properties imparted by the presence of nitrile groups [62]. Namely, unlike most vinyl polymers, PAN is semi-crystalline despite being atactic. PAN's crystallinity is therefore driven by the highly dipolar

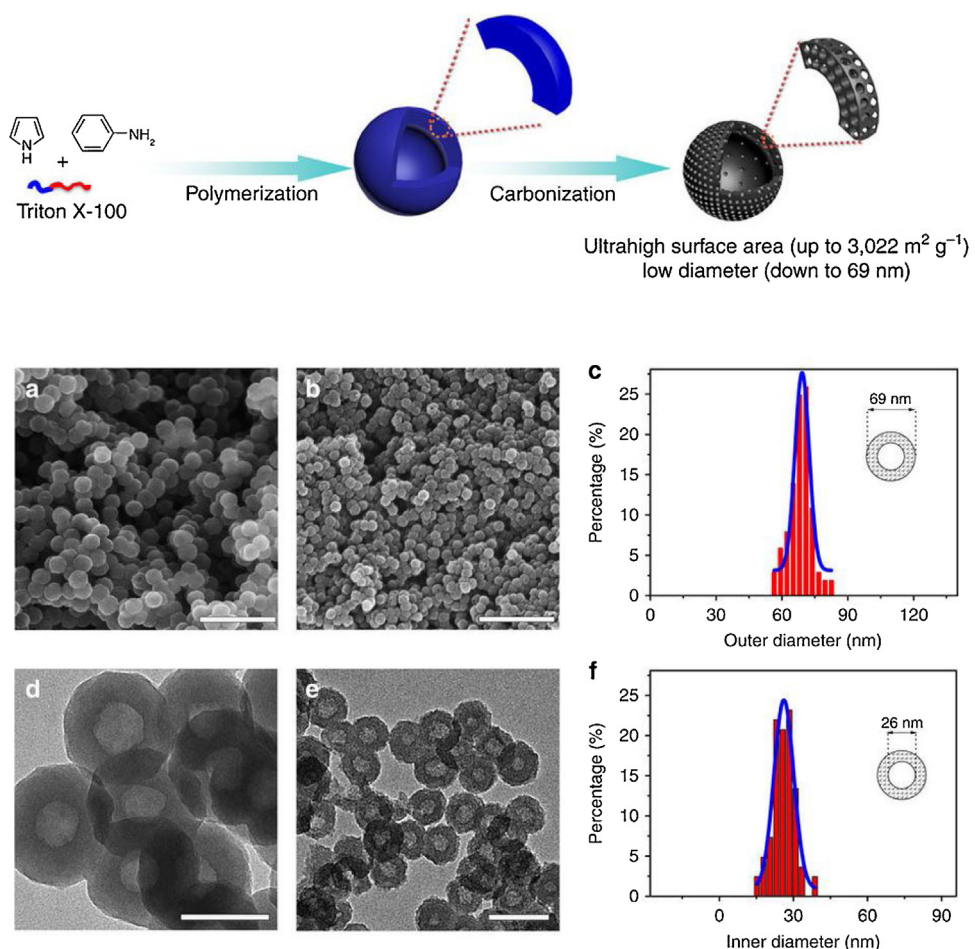
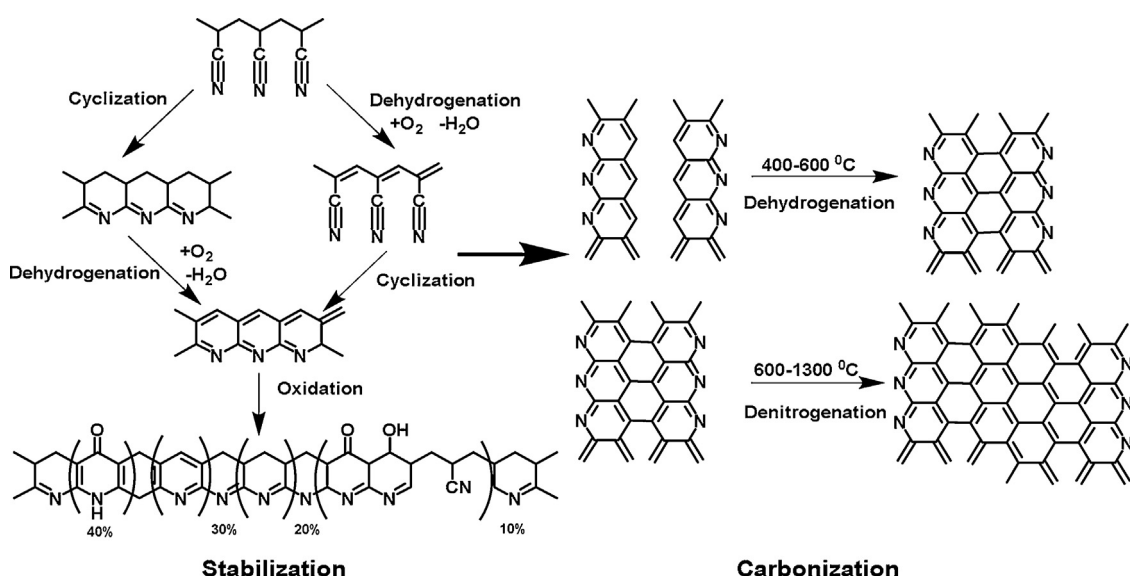


Fig. 3. Design and fabrication of hollow carbon nanospheres (HCNs); SEM images of (a) PACP and (b) HCN-900-20H2R; TEM images of (d) PACP and (e) HCN-900-20H2R; (c) outer and (f) inner diameter distribution histograms of HCN-900-20H2R from analysis of SEM and TEM images, respectively. Scale bars, 500 nm (a,b), 100 nm (d) and 200 nm (e). [59]. Copyright 2015. Reproduced under the Creative Commons 4.0 International license.



Scheme 2. Two step thermal processing of PAN into carbon: oxidative stabilization and formation of a ladder polymer (left); carbonization/graphitization (right). Partially adapted from ref. [61] and [70].

nitrile groups that repel each other within one chain and form dipolar bonds between chains. These interactions force PAN to adopt an extended, all-trans conformation, which results in hexagonal chain arrangement [63–65]. Indeed, a Bragg peak corresponding to hexagonal packing can be observed in the WAXS spectrum of PAN with the inter-helical spacing of 6.13 Å. Additionally, due to the strong nitrile-nitrile interactions, PAN is only soluble in polar organic solvents, such as DMF, DMSO, dimethylacetamide (DMAA), ethylene carbonate (EC), ionic liquids or concentrated aqueous solutions of inorganic salts, e.g. sodium thiocyanate, zinc chloride or zinc bromide [66–68]. Moreover, PAN undergoes degradation at $\tilde{300}$ °C, namely below its melting point. This limited the early attempts to process PAN into carbon fibers due to the low carbon yields. Two step thermal treatment used to prepare high-performance fibers was developed in 1959 and consists of an initial oxidative stabilization at moderate temperatures (200–300 °C), followed by high-temperature carbonization/graphitization under inert atmosphere (Scheme 2) [62,69].

Stabilization is critical to obtain high modulus fibers. A ladder-like, conjugated polymer is formed during this step due to dehydrogenation of PAN and cyclization of the nitrile groups. This cyclized, rigid structure helps to preserve the morphology of the fiber and achieve high carbon yield during graphitization. Although the exact mechanism of the stabilization process is still not fully understood, the presence an oxidative atmosphere is crucial to retain morphology and superior mechanical properties in the resulting fibers. When stabilizing in air, the heat of cyclization dissipates over a broader temperature range, which helps to avoid degradation of morphology due to fast release of heat that occurs under inert conditions [70,71]. Additionally, recent solid-state NMR studies determined that stabilization under air leads to longer conjugated structures, namely six-membered aromatic rings, as opposed to separated rings observed in PAN stabilized under inert atmosphere. Oxygen facilitates dehydrogenation and is incorporated in the cross-linked PAN leading to retention of the highly oriented structures desired for further carbonization [71–73]. Thus, a random copolymer of AN containing a few wt % of different vinyl monomers, such as methyl acrylate (MA), methyl methacrylate (MMA), carboxylic acids (e.g. acrylic or itaconic) or vinyl esters, is typically used as carbon fiber precursor rather than a PAN homopolymer [69]. Acidic co-monomers introduce an ionic mechanism of cyclization of the nitrile groups in addition to the typical radical one occurring in pure PAN, which decreases the onset and peak temperatures of stabilization, whereas vinyl esters act as plasticizers improving solubility of precursors in spinning solutions [74].

Stabilization allows for further processing without melting the fibers and minimizes the weight loss. In the second step, the cross-linked ladder polymer is subjected to pyrolysis in an inert atmosphere at 600–1300 °C, followed by graphitization at 1500–3000 °C. During the carbonization process further dehydrogenation and denitrogenation occurs and larger graphitic domains are formed. The entire process is accompanied by evolution of various gaseous products such as HCN, H₂O, O₂, H₂, CO, NH₃, CH₄ with a typical carbon yield of 50–60% with respect to the original precursor [69].

PAN copolymer precursors for carbon fibers are synthesized by free radical polymerization (FRP). However, the development of controlled radical polymerization (CRP) methods enabled facile synthesis of polymers with controlled molecular weight (MW), molecular weight distribution (MWD) and chain topology. That, in turn, opened a possibility to utilize low MW PAN-containing polymers as precisely tailored precursors to nanostructured carbon materials. This review summarizes the recent progress in the synthesis of well-defined PAN and its copolymers by controlled/living polymerization techniques as well as the use of polymer architec-

tures with various morphologies as precursors for nitrogen-doped nanocarbons. Several applications of PAN-derived NDC in catalysis and energy storage are then discussed to demonstrate versatility of this synthetic approach.

2. Controlled synthesis of PAN

2.1. Conventional radical and anionic polymerization

Commercial PAN and its copolymers are synthesized exclusively by FRP. Due to PAN's insolubility in its own monomer, polymerization of acrylonitrile (AN) is carried out in solution, suspension or emulsion, in the presence of radical initiators, such as azobisisobutyronitrile (AIBN) or peroxides. FRP of AN leads to an atactic polymer, with typical ratio of isotactic:heterotactic:syndiotactic (*mm*:*mr*:*rr*) triads 0.22:0.56:0.22. Highly isotactic PAN was prepared via inclusion polymerization of AN/urea canal complex at extremely low temperatures (77–195 K) with electron beam, γ -ray or UV irradiation to initiate polymerization [75–79]. Recently, completely isotactic PAN was synthesized by initiating the polymerization of AN at 77 K in highly organized urea canals and increasing the temperature to 163–183 K for the propagation step [79]. This allowed long radical lifetime and prevented bimolecular termination and chain-transfer reactions, resulting in the molecular weight increasing with conversion, relatively low dispersity ($D = 1.5$) and completely isotactic PAN (*mm* triads >99%).

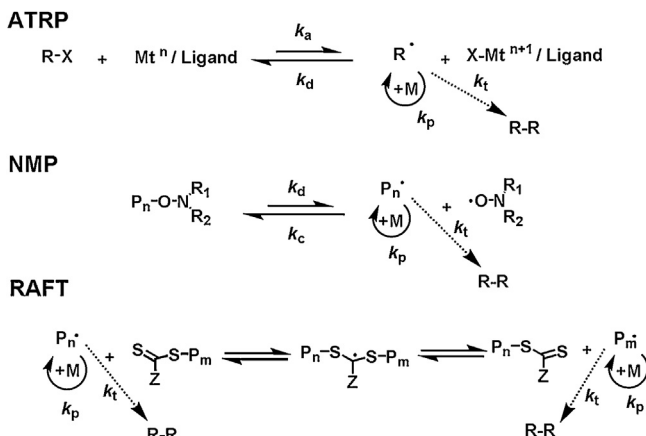
Additionally, FRP was used to synthesize more complex architectures containing PAN. Limited examples include block copolymers, graft copolymers, and spherical nanoparticles (NPs) [80–85]. However, FRP does not provide control over the MW, MWD and functionality; in order to prepare PAN with controlled molecular structure and to synthesize more complex architectures, such as block, graft [86], star [87], and brush copolymers [88], anionic polymerization was utilized. Coordination or anionic polymerization AN was reported using organometallic initiators, including organocupper [89,90], di(organooimido)chromium(VI) complexes [91], methoxy- β -diketone nickel catalysts [92], and cobalt-based catalysts [93] as well as metal-free ammonium methanide initiators [94]. The use of dialkylmagnesium initiators in a water-based system yielded PAN with high MWs and increased isotacticity [95].

Cy₃PCuMe and (Bipy)₂FeEt₂ were used to induce the polymerization of acrylonitrile that exhibited characteristics of an anionic polymerization mechanism [96]. However, compared to PAN prepared via FRP, polymers synthesized by ionic polymerization usually have lower molecular weight and exhibited significant branching that arises from inter- or intramolecular abstraction of methine protons from the polymer backbone by the propagating carbanion [96,97].

2.2. Reversible deactivation radical polymerization (RDRP)

Reversible deactivation radical polymerization (RDRP) methods, also known as controlled/living radical polymerization (CRP) have revolutionized polymer chemistry over the last two decades by providing facile tools to synthesize well-defined, functional polymers, thus enabling the engineering of complex macromolecules [98–100].

All RDRP methods, such as atom transfer radical polymerization (ATRP) [101–106], reversible addition fragmentation chain-transfer (RAFT) polymerization [107–109], and nitroxide-mediated polymerization (NMP) [110–112], rely on a fast dynamic equilibrium between dormant chain ends and active radical species to afford control over the reaction. This equilibrium is strongly shifted towards the dormant state to establish a very low con-

**Scheme 3.** Mechanisms of RDRP Processes: ATRP, NMP and RAFT.

centration of propagating radicals, thus reducing the probability of unavoidable termination reactions (**Scheme 3**). ATRP utilizes transition metal catalysts, most often Cu, that reversibly activate and deactivate growing polymer chains via transfer of a halogen atom, such as chlorine or bromine. Similarly, NMP uses stable nitroxides to reversibly deactivate growing (macro)radicals. RAFT polymerization is based on degenerative transfer and employs dithioesters, trithiocarbamates or xanthates as chain transfer agents (CTA) to establish a rapid exchange between growing (macro)radicals and dormant species. Through the process of reversible activation/deactivation of the chain end the average lifetime of a (macro)radical in a RDRP during the polymerization is extended from seconds to hours or even days. This allows for the preparation of well-defined polymers with predetermined MW, low dispersity, preserved chain end functionality (CEF) and complex architectures such as blocks, stars, bottlebrushes etc. [113,114].

RDRP methods are currently the most widely utilized synthetic routes to polymerize AN [115]. One major consideration when preparing PAN via RDRP methods is the overestimation of the MW of PAN by gel permeation/size exclusion chromatography (GPC/SEC) in DMF based on linear polystyrene (PS) or poly(methyl methacrylate) (PMMA) standards [116,117]. Therefore, ¹H NMR or GPC with a multi-angle light scattering detector (MALLS) should be employed to determine the actual molecular weight of PAN [118–120]. Usually, the MW of PAN determined by GPC/RI using linear PS or PMMA standards, is 2.5–3 times higher than the actual value determined by GPC/MALLS or ¹H NMR [118,119]. However, a remarkably good correlation between MW measured by a RI detector and theoretical values can be obtained using linear poly(ethylene oxide) (PEO) standards [121].

2.3. RDRP of acrylonitrile (AN)

2.3.1. Atom transfer radical polymerization (ATRP)

The first synthesis of well-defined PAN by ATRP with predefined MWs and very low dispersities ($D=1.01$, as determined by MALDI-TOF MS, **Fig. 4**) was reported in 1997 [122,123]. This was achieved using CuX/2,2'-bipyridine (bpy; X = Br or Cl) as the catalyst, 2-bromopropionitrile (BPN) or 2-chloropropionitrile (CPN) as initiators, and ethylene carbonate (EC) as the solvent. Controlled polymerization of AN based on CuBr/bpy, CuCl/bpy, Cu₂O/bpy, and CuO/bpy, in the presence of alkyl, alkylsulfonyl, and arenesulfonyl halides was later reported [124]. CuBr/tetramethylguanidinotris(2-aminoethyl)amine (TMG₃-TREN) was used for a catalyst in EC to successfully synthesize PAN with dispersity $D=1.25$ and $M_n=8000$ [125]. In addition to this “traditional” solvent, 2-cyanopyridine was used to synthesize well-defined PAN by ATRP.

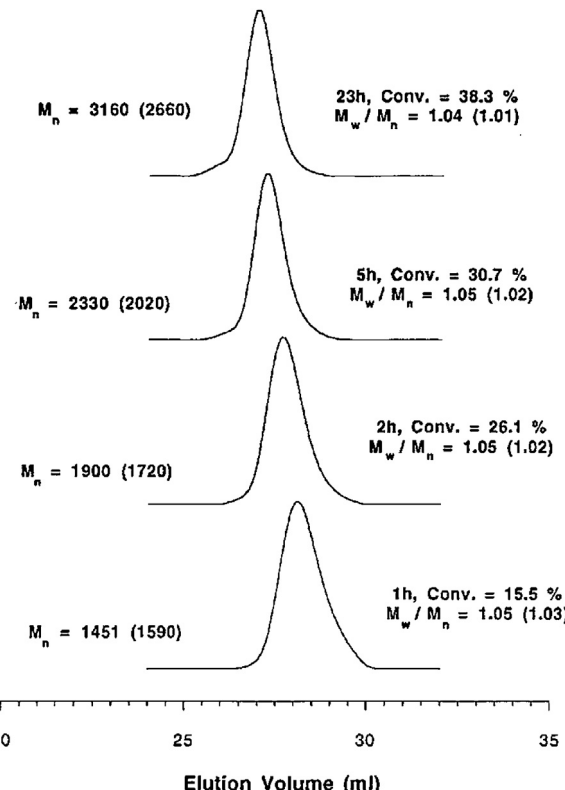


Fig. 4. GPC traces showing the first example of successful ATRP of AN. Conditions: [AN]:[BPN]:[CuBr]:[bpy] = 95:1:0.1:0.3, AN:EC = 1:0.7 (v/v), T = 44 °C. M_n determined by ¹H NMR (MALDI), M_w/M_n by SEC (MALDI). [122], Copyright 1997. Reproduced with permission from American Chemical Society.

The unique feature of this solvent is that it does not contain any easily extractable hydrogens, but at the same time has a high enough polarity to dissolve PAN [126].

Several reverse ATRP routes for controlled radical polymerization of AN were described [127–130]. A hexa-substituted ethane thermal iniferter, diethyl 2,3-dicyano-2,3-diphenylsuccinate (DCDPS), was used as the initiator when CuCl₂/bpy, FeCl₃/triphenyl phosphine (PPh₃), or FeCl₃/iminodiacetic acid (IMA) was the catalyst [127,130,131]. FeCl₃/IMA or FeCl₃/isophthalic acid was used with AIBN as the radical initiator [128,129]. All of the well-defined PAN samples were then used as macroinitiators for chain-extension with AN, confirming high retained CEF. **Table 1** summarizes results of polymerization of AN by normal and reverse ATRP.

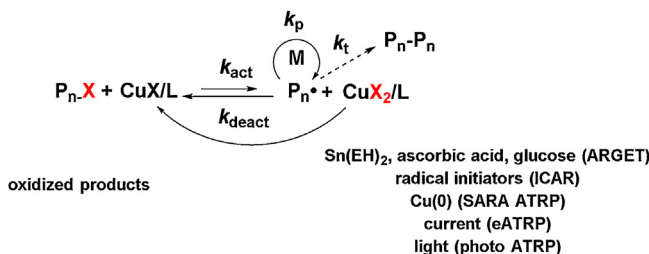
2.3.2. Activator regeneration methods for ATRP

Activator regeneration methods for ATRP employ various reducing agents in order to convert Cu^{II} to Cu^I after termination events, thus allowing a significant reduction in the amount of catalyst needed to conduct an ATRP, typically to the ppm levels (vs monomer). Reducing agents can be chemical (i.e. proceed via electron transfer), such as tin (II) 2-ethylhexanoate (Sn(EH)₂) or ascorbic acid in activators regenerated by electron transfer (ARGET) ATRP, radicals formed from conventional radical initiators (e.g., AIBN) in initiators for continuous activator regeneration (ICAR) ATRP, zero-valent metals in supplemental activators and reducing agents (SARA) ATRP, or physical procedures such as electrical current (eATRP) or light (photoATRP) (**Scheme 4**) [104,106]. Development of activator regeneration techniques has led to more ‘green’ ATRP reactions by drastically reducing the Cu concentration, which also made the purification of synthesized polymers significantly easier. This is especially important for applications of PAN as car-

Table 1

Normal and Reverse ATRP of AN.

Ref.	Catalyst	Ligand	R-X	Solvent	Temp. (°C)	Conv.	M_n	\mathcal{D}
[122,123,132]	CuBr	bpy	BPN	EC	44–65	~90%	<15,000 (NMR)	<1.05 (MALDI)
	CuCl	bpy	CPN	EC	100	60%	5000 (GPC)	1.15
	CuCl	bpy	TMSC	EC	100	68%	5400 (GPC)	1.28
[124]	Cu ₂ O	bpy	BPN	EC	100	73%	8400	1.15
	Cu ₂ O	bpy	MBSC	EC	100	71%	6700	1.37
[125]	CuO	bpy	MSC	EC	100	45%	6900	1.17
	CuBr	TMG ₃ -TREN	BPN	EC	45	~70%	8000 (NMR)	1.25
[126]	CuBr	bpy	BPN	CP	55	50%	3000 (NMR)	<1.1
	CuCl ₂	bpy	DCDPS	Bulk	70	43%	4800 (GPC)	1.17
[127–131]	FeCl ₃	IPA	AIBN	DMF	60	54%	6200 (GPC)	1.18
	FeCl ₃	IMA	DCDPS	DMF	70	38–74%	5500–12300 (GPC)	≤1.25
	FeCl ₃	PPh ₃	DCDPS	Bulk	70	50%	7000	1.16
	FeCl ₃	IMA	AIBN	DMF	60	38%	5200	1.16

**Scheme 4.** Activator Regeneration ATRP.

bon precursor, since any residual transition metal could interfere with the carbonization process as well as influence the performance of prepared carbons.

PAN with MWs as high as 161,000 ($M_{n, GPC}$) and $\mathcal{D} = 1.18\text{--}1.47$ Fig. 5, was prepared by ARGET ATRP [118]. This was achieved using BPN as an initiator, EC or DMSO as a solvent, Sn(EH)₂ or glucose as a reducing agent, and 25–75 ppm of CuCl₂/tris[(2-pyridyl)methyl]amine (TPMA) catalyst. The use of low ppm ARGET ATRP reduced side reactions between the catalyst and growing radicals that limited achievable MW in normal ATRP of AN.

ARGET ATRP was conducted in ionic liquids with 1,1,4,7,7-pentamethyldiethylenetriamine (PMDETA) as a ligand and the reducing agent [133]. In 1-butyl-3-methylimidazolium tetrafluoroborate higher conversion ($M_{n, GPC}$ up to 43,700) and lower dispersities ($\mathcal{D} = 1.25$) were reached than in DMF. Tris[2-dimethylamino)ethyl] amine (Me₆TREN) was also used as both a ligand and the reducing agent in DMSO at room temperature, yielding $M_{n, GPC}$ from 4,300–10,500 and \mathcal{D} values ranging from 1.13–1.32 [134].

AN was polymerized by ICAR ATRP using CuBr₂/bpy as a catalyst, ethyl 2-bromo isobutyrate (EBiB) as an initiator, AIBN as the free radical initiator source, and DMSO as the solvent [135]. At 70 °C the $M_{n, GPC}$ reached 4100 with a narrow MWD ($\mathcal{D} = 1.07$) with 400 ppm of catalyst in the system. At high radical initiator concentrations with 100 ppm of CuBr₂/bpy catalyst, 80% conversion was reached in 3 h, but with a large discrepancy between theoretical and experimental MWs, due to the continuous initiation of new polymer chains by AIBN [136]. Recently, ICAR ATRP of AN was explored using low concentrations of catalyst, namely ≤50 ppm in DMSO, and CuBr₂/TPMA provided the best control. Excellent agreement between theoretical and experimental MW and low dispersities ($\mathcal{D} < 1.3$) were observed when reducing concentration of CuBr₂/TPMA from 50 to 10 ppm. Interestingly, reasonable control over polymerization was maintained after decreasing the amount of catalyst to 1 ppm vs monomer, however experimental MWs were higher than theoretical values. This was likely due to high viscosity, caused by initial rapid increase of MW that suppressed diffusion-controlled radical termination and led to PAN with $\mathcal{D} = 1.41$ in 10 h (Fig. 6).

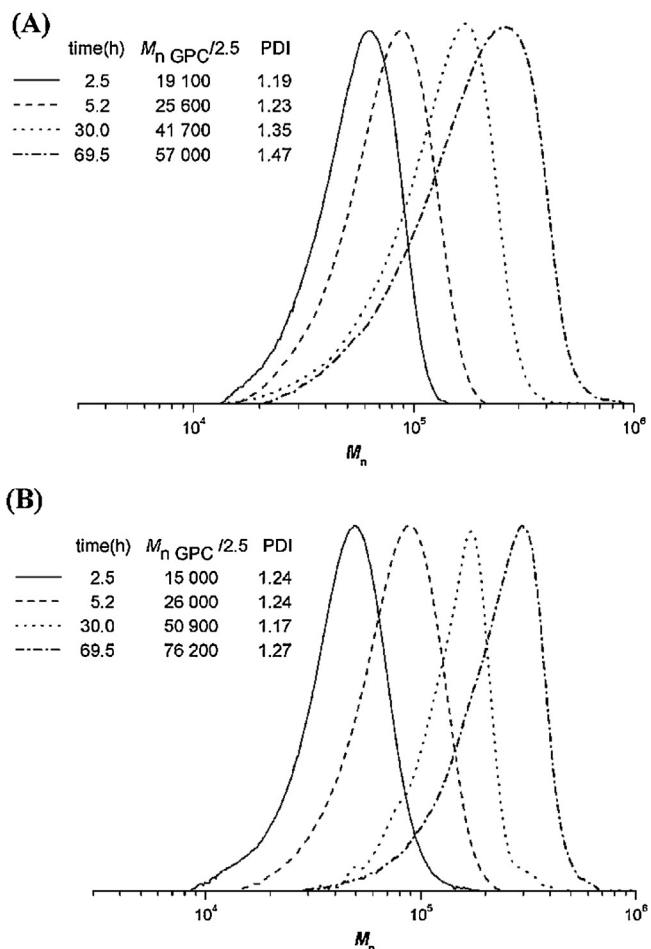


Fig. 5. ARGET ATRP of acrylonitrile with 75 ppm (A) and 25 ppm (B) of copper catalyst. Conditions: (A) [AN]:[BPN]:[CuCl₂]:[TPMA]:[Sn(EH)₂] = 2000:1:0.15:1:1.5:1; (B) [AN]:[BPN]:[CuCl₂]:[TPMA]:[Sn(EH)₂] = 2000:1:0.05:0.55:0.5; AN:EC = 1:2.4 (v/v), T = 65 °C. [118], Copyright 2007. Reproduced with permission from American Chemical Society.

SARA ATRP was also explored for PAN synthesis under low ppm catalyst conditions. Zn(0) powder was used as a supplemental activator and reducing agent, EBiB as an initiator, 5–50 ppm CuBr₂/bpy as a catalyst, EC as a solvent, and the reaction was conducted at 25 °C. Conversion reached above 70%, when 50 ppm Cu-catalyst was used, the $M_{n, GPC}$ reached 28,200 with dispersities remaining below 1.2 [137]. SARA ATRP was conducted by adding Cu(0) powder to a solution of AN, DMSO, ligand bpy [138] or Me₆TREN [139] (ligand), and EBiB [138] or BPN [139] (initiator). The reaction in both cases proceeded slowly, requiring 12 h to reach >90% conversion [138] or

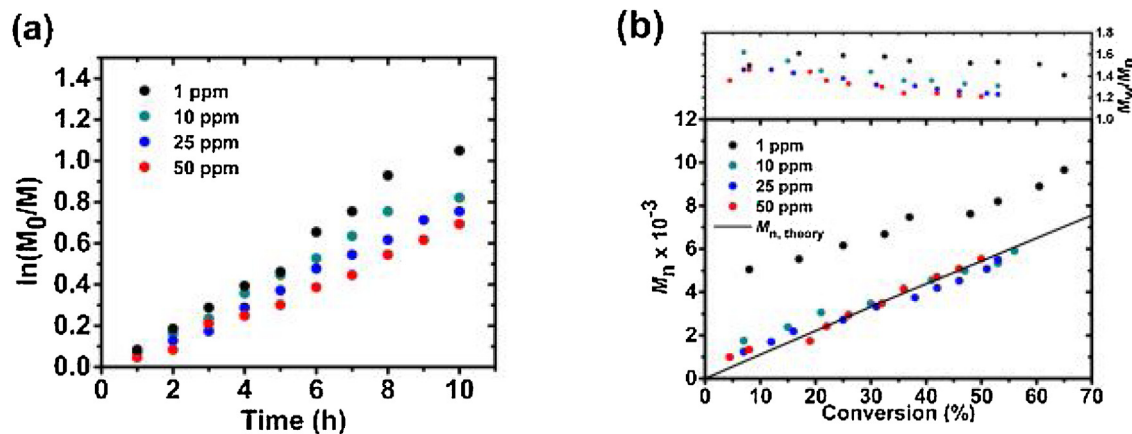


Fig. 6. (a) First-order kinetic plots and (b) MW and MWD evolution in ICAR ATRP of AN with different amount of CuBr₂/TPMA catalyst. [AN]:[BPN]:[AIBN]:[CuBr₂]:[TPMA]=200:1:0.1:*n*:3*n*. AN:DMSO=1:1.25 (v/v), T=65 °C. [121]. Copyright 2016. Reproduced with permission from John Wiley and Sons.

40 h to reach 70% conversion [139], as activation of alkyl halides by Cu(0) was much slower than by Cu(I)-catalyst complexes [140].

The activity of different ligands, namely bpy, PMDETA and TPMA in SARA ATRP of AN conducted in DMSO at room temperature was compared. The most active catalyst, CuBr₂/TPMA, led to pronounced termination and limited conversion, whereas CuBr₂/bpy or CuBr₂/PMDETA allowed synthesis of well-defined PAN ($M_n = 9000$, $D = 1.19$, Fig. 7). Notably, inferior control with the CuBr₂/TPMA catalyst is opposite to what was observed in ICAR ATRP of AN [121]. This activity trend is not typical for low ppm ATRP techniques, as usually highly active, strongly binding ligands are necessary to fully complex small amounts of Cu(II) [141]. However, AN is the most active monomer in ATRP and also exhibits high k_p [142–144]. Thus, due to the high activity of AN and efficient reduction of CuBr₂ by comproportionation with Cu(0), fast activation creates high concentrations of radicals that rapidly terminate. In ICAR ATRP, polymerization rate does not depend on the catalyst used, but only on the decomposition rate of radical initiator [145,146]. Thus, CuBr₂/TPMA improved control in ICAR ATRP by providing faster deactivation, but was too active in SARA ATRP of AN. However, bpy and PMDETA are the most widely used and least expensive ligands, making the SARA ATRP conditions for AN polymerization promising for a potential scale-up.

CuBr₂/TPMA complex has been also used to polymerize AN by electrochemically-mediated ATRP (eATRP) in DMSO with the addition of tetraethylammonium tetrafluoroborate (Et₄NBF₄) as a supporting electrolyte [147]. Polymerization was conducted at 60 °C with the BPN initiator. PAN with MWs up to 90,000 was obtained with good control (MWD 1.07–1.60), however with some considerable deviations from theoretical values. Deviations from linear kinetics at higher conversions (>40%) suggested termination by coupling, similar to that observed in SARA ATRP with CuBr₂/TPMA. This can point out to a possibility of improving linearity by using less active ligands, like bpy or PMDETA.

To further decrease the amount of transition metals, AN was polymerized using metal-free ATRP with 10-phenyl-phenothiazine (Ph-PTZ, Scheme 5), previously reported to mediate polymerization of MMA [148]. This process involves a photoredox mechanism upon excitation of the Ph-PTZ with UV light. In the excited state Ph-PTZ molecule is able to abstract halogen from an ATRP initiator/polymer chain and activate the polymerization [149]. Reasonable control over metal-free ATRP of AN was achieved and yielded PAN with $M_n = 1700$ –4400, but with moderate dispersities ($D = 1.42$ –1.88), indicating slow deactivation of propagating radicals in this system. Preserved CEF of synthesized PAN was confirmed by successful

chain extension with MMA [119]. Table 2 summarizes the results of activator regeneration ATRP and metal-free ATRP of AN.

2.3.3. Reversible addition fragmentation transfer (RAFT) polymerization

Similarly to metal-free ATRP, RAFT polymerization can be used to synthesize PAN devoid of residual metal contamination. The synthesis of PAN by RAFT using 2-cyanoethyl dithiobenzoate (CED) as the CTA, was first reported Scheme 6 [150]. In RAFT polymerization, the choice of both the Z and R groups is crucial to achieve high chain transfer constants [151–153]. When using CED for RAFT polymerization, the CH₃–CH–(CN)[•] radicals effectively initiated the polymerization of AN, as they resemble propagating radicals. The RAFT agent 2-cyanoprop-2-yl dithiobenzoate (CPDB) was an efficient chain transfer agent for the preparation of PAN with controlled molecular weight (below 6000) and narrow MWD ($D \leq 1.10$) [154]. The polymerization rate was proportional to the concentration of AIBN and exhibited negative exponential dependence on the concentration of CPDB. AN was also polymerized using dibenzyl trithiocarbonate (DBTC) as the chain-transfer agent [155]. PAN with $M_{n,NMR}$ up to 8400 and low dispersity (<1.2) was obtained. CPDB was used as a RAFT agent for AN polymerization, resulting in high molecular weight PAN ($M_n > 20,000$) and dispersity as low as 1.05 [156].

High molecular weight (HMW) PAN was also synthesized by RAFT polymerization. 1,4-[2-(carbazole-9-carbodithioate)-2-methyl propionic acid] phenyl ester (BCCDP) was used as a CTA for AN polymerization using DMSO as a solvent [157]. The authors were able to synthesize PAN with molecular weight (M_n) up to 405,100 and dispersities ranging from 1.14 to 1.32. Four CTAs were investigated and cyanoethyl dodecyl trithiocarbonate (CEDT) or 2-cyano-2-propyl dodecyl trithiocarbonate (CPDT) worked well when targeting HMW PAN [158]. Additionally, lowering the amount of radical initiator, relative to the CTA, and decreasing the temperature to 30 °C allowed reaching higher conversions and MW. Zhu et al. recently demonstrated a photoinduced RAFT procedure to prepare HMW PAN (up to $M_n = 286,300$) in the absence of any external radical source in EC. CPDT was shown to undergo a photolysis upon illumination with blue light ($\lambda = 460$ –470 nm) directly forming initiating radicals. Well-defined PAN with low dispersity ($D = 1.06$ –1.23) was synthesized [159].

RAFT polymerization of AN in aqueous media utilizing concentrated solutions of NaSCN (50 wt.%) or ZnCl₂ (60 wt.%), solvents used industrially in fiber technology, was reported. 4-Cyano-4-(phenylcarbonothioylthio)pentanoic acid (CPAD), a CTA widely utilized in aqueous RAFT, provided good control over the reaction

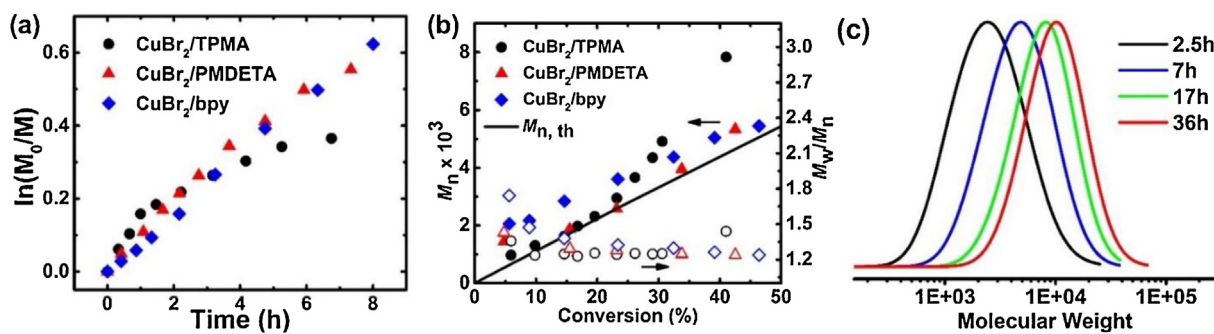
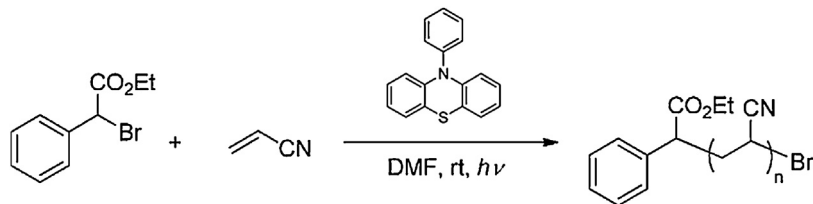


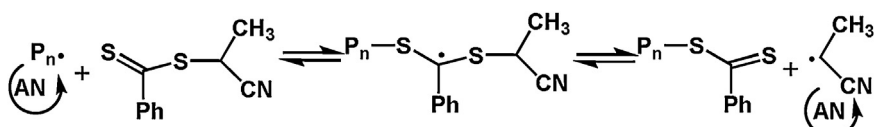
Fig. 7. (a) First order kinetic plots, (b) $M_{n,th}$ and D evolution for SARA ATRP of AN with different catalysts. $[AN]:[BPN]:[CuBr_2]:[L]=200:1:0.01:0.03$, Cu-wire (3 cm × 1 mm), [L] = TPMA, PMDETA or bpy; $V^o_{AN} = 3$ mL, AN:DMSO = 1:1.25 (v/v), rt. (c) GPC traces for conditions $[AN]_0/[BPN]_0/[CuBr_2]_0/[bpy]_0=200/1/0.01/0.03$; Cu-wire (3 cm × 1 mm), $V^o_{AN} = 3$ mL, AN:DMSO = 1:1.5 (v/v). [141], Copyright 2017. Reproduced with permission from American Chemical Society.



Scheme 5. Photoinduced metal-free ATRP of acrylonitrile with Ph-PTZ as the catalyst.

Table 2
Activator Regeneration ATRP and Metal-free ATRP of AN.

Ref.	Method	Catalyst	Catalyst Amount (ppm)	Reducing Agent	R-X	Solvent	T (°C)	Conv. (%)	M_n	D
[118]	ARGET	CuCl ₂ /TPMA	50	glucose	BPN	DMSO	40	69	161,300	1.18
[133]	ARGET	CuBr ₂ /PMDETA	1250	PMDETA	EBiB	[C ₄ mim][BF ₄] ⁻	65	64	43,650	1.25
[134]	ARGET	CuBr ₂ /Me ₆ TREN	250	Me ₆ TREN	EBiB	DMSO	25	22-79	4300-10,500	1.13-1.32
[135,136]	ICAR	CuBr ₂ /bpy	50, 400	AIBN	EBiB	DMSO	60-70	40-86	4100-11,700	1.07-1.38
[121]	ICAR	CuBr ₂ /TPMA	1-50	AIBN	BPN	DMSO	65	42-85	4400-26,200	1.11-1.41
[137]	SARA	CuBr ₂ /bpy	50	Zn(0)	EBPA	DMSO	rt	72	4100	1.53
[139]	SARA	CuBr ₂ /Me ₆ TREN	200	Cu(0)	BPN	DMSO	25	43	44,100	1.25
[141]	SARA	CuBr ₂ /bpy	50	Cu(0)	BPN	DMSO	rt	83	9000	1.19
[147]	eATRP	CuBr ₂ /TPMA	40-160	current	BPN	DMSO/Et ₄ NBF ₄	60	40-73	8000-91000	1.07-1.60
[119]	Metal-free	Ph-PTZ	1000	–	EBPA	DMF	rt	63	4400	1.42



Scheme 6. RAFT polymerization of AN using CED as the transfer agent.

Table 3
RAFT Polymerization of AN.

Ref.	CTA	Initiator	Solvent	T (°C)	Conv. (%)	M_n	D
[150]	CED	AIBN	EC	60	40	4000 (NMR)	1.05
[154]	CPDB	AIBN	DMF	65	50	5600 (NMR)	1.06
[156]	CPDB	AIBN	EC	90	50	26,000 (viscosity)	1.05
[155]	DBTC	AIBN	DMF	60	58	5700 (NMR)	1.18
[161]	BTBDS	AIBN	EC	80	50	39,800 (GPC)	1.50
[161]	BTPADS	AIBN	EC	80	67	38,000 (GPC)	1.53
[157]	BCCDP	AIBN	DMSO	75	60	405,100 (viscosity)	1.32
[158]	CEDT	V-70	EC	30	62	70,300	1.09
[158]	CPDT	V-70	EC	30	63	84,800	1.24
[159]	CPDT	–	EC	rt	56	218,000	1.21
[160]	CPAD	AIBN VA-044	Aq. NaSCN (50 wt. %)	65	>60	6000-60,000	<1.3
[160]	CPAD	V-70	Aq. ZnCl ₂ (60 wt. %)	30	52	22,200	1.38

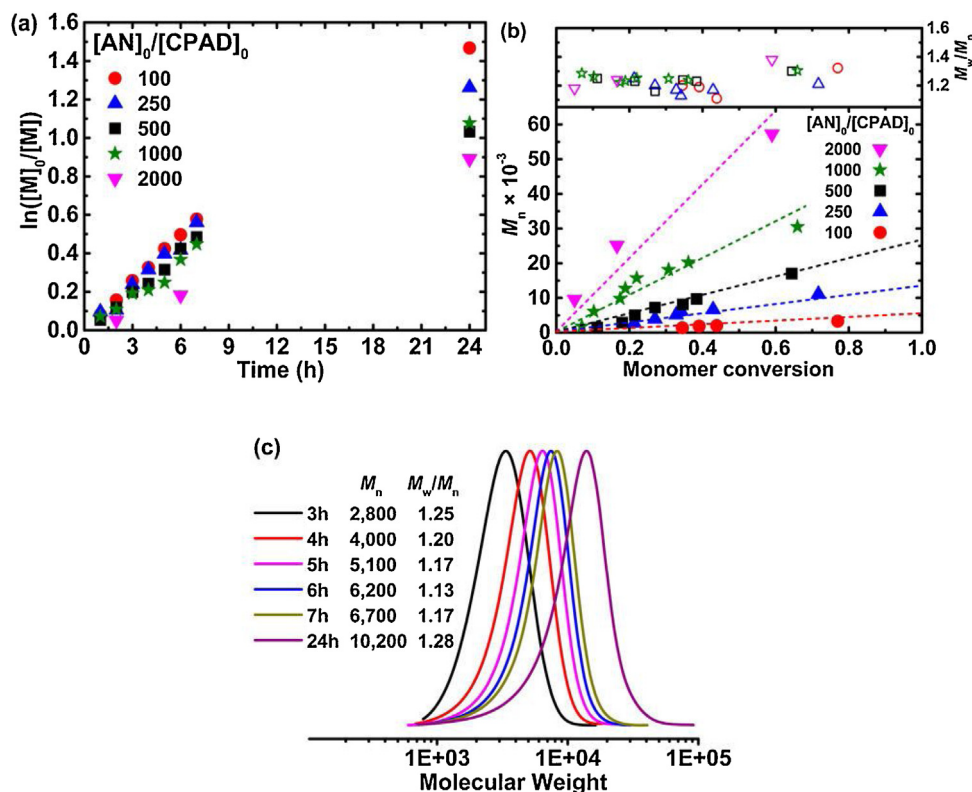


Fig. 8. RAFT polymerization of AN in aqueous NaSCN (50 wt%) (a) First-order kinetic plots and (b) MW and MWD evolution with different targeted DPs. $[AN]:[CPAD]:[AIBN] = DP_{target}:1:0.4$, AN:50 wt % aqueous NaSCN = 1:1.5 (v/v); $T = 65^\circ\text{C}$, 24 h. For targeted DP = 2000, VA-044 was used as the radical initiator at 44°C . (c) GPC traces of PAN prepared using molar ratios $[AN]:[CPAD]:[AIBN] = 250:1:0.4$. [160], Copyright 2016. Reproduced with permission from American Chemical Society.

initiated with AIBN for aqueous NaSCN or V-70 for the aqueous ZnCl_2 solution. Excellent agreement between theoretical and experimental MW and low dispersity ($D < 1.4$) was observed. Well-defined PAN covering a broad range of MWs (ca. 6000–60,000) was obtained (Fig. 8). Macro-CTA synthesized in aqueous NaSCN was extended with AN in the same solvent with excellent chain extension efficiency, as opposed to a macroinitiator formed in a control reaction conducted in DMSO, which showed significant retardation [160]. Table 3 summarizes the results of RAFT polymerization of AN.

2.3.4. Nitroxide-Mediated Polymerization (NMP)

Controlled NMP of AN with 2,2,5-trimethyl-3-(1-phenylethoxy)-4-phenyl-3-azahexane (TPPA) was reported [111]. The molecular weight could be controlled from 4000 to 50,000 with dispersity below 1.2. n-Tert-butyl-1-diethylphosphono-2,2-dimethylpropyl nitroxide (SG1) was used to form PAN with controlled molecular weight and dispersity (Table 4) [132]. However since 2003, there have been no reports on the synthesis of PAN by NMP. Quantum mechanical calculations were used to model 2,2,6,6-tetramethyl-1-piperidinyloxy (TEMPO)-mediated free-radical polymerization of AN [162].

2.3.5. Cobalt-mediated radical polymerization (CMRP)

Controlled CMRP of AN in the presence of bis(acetylacetato)cobalt(II) ($[\text{Co}(\text{acac})_2]$) was reported [163,164]. The reversible equilibrium was established between a free radical polymer chain and $\text{Co}(\text{acac})_2$ and an alkyl-Co(acac)₂ complex. The best level of control was achieved by using organocobalt (III) adduct as the initiator at 0°C in DMSO. The dispersity of the product was as low as 1.1. With V-70 as the initiator, PAN with molecular weight as high as 120,000 was synthesized, which is within the desired MW range of industrial carbon fiber application (Table 5).

2.4. Random copolymerization of acrylonitrile

Numerous reports described the use of ATRP, NMP, and RAFT to copolymerize AN with styrene to produce commercially important poly(styrene-co-acrylonitrile) (PSAN) [120,151,165–172].

Copolymerization of acrylonitrile with other monomers, such as MMA, [173] ethyl methacrylate [174], maleic anhydride [175], itaconic acid (IA) [176], methyl acrylate (MA), *n*-butyl acrylate (BA), *t*-butyl acrylate (*t*-BA) [177], acrylamide [178], and N-isopropylacrylamide (NIPAM) [179] have been studied to improve properties of PAN-derived carbon fibers by controlling their MW, MWD, and comonomer distribution.

Recently, carbon fibers prepared from poly(AN-co-IA-co-MA), a copolymer composition typically used in fiber technology, synthesized by FRP and RAFT were directly compared. Both copolymers had similar M_n of 330,000–340,000 (PMMA standard) and compositions reflecting those for commercial fiber precursors, but different dispersities, namely $D = 1.16$ or 1.95 for the RAFT and the FRP sample, respectively. Fibers were spun from both polymers and carbonized according to commercial procedures in a pilot-scale plant. The solution of the RAFT-based polymer in DMAA exhibited significantly lower viscosity than the control sample, making it easier to process. Furthermore, carbon fibers prepared from the RAFT-made PAN showed improved Young's modulus and tensile strength (Fig. 9) [180]. RAFT polymerization was also used to synthesize acrylonitrile-butadiene rubber (NBR) to obtain polymers with controlled MW and low dispersities ($D \geq 1.2$) [181–183].

2.5. Synthesis of PAN block copolymers

2.5.1. ATRP

RDRP methods are compatible with a wide range of monomers including acrylates, methacrylates, acrylamides, and styrene

Table 4
NMP of AN.

Ref.	Nitroxide	Initiator	Solvent	Temp. (°C)	Conv. (%)	M_n (GPC)	\bar{D}
[111]	TPPA	TPPA	DMF	120	/	55000	1.13
[132]	DEPN or SG1	AIBN	EC	120	90	26,000	1.20

Table 5
CMRP of AN.

Ref.	Mediator	Initiator	Solvent	Temp. (°C)	Conv. (%)	M_n (GPC)	\bar{D}
[163,164]	Co(acac) ₂	V-70	DMSO	30	87	10,100	1.89
[163,164]	Co(acac) ₂	Organocobalt(III) adduct	DMSO	0	<50	24,200	1.14
[163,164]	Co(acac) ₂	V-70	DMSO	30	90	120,000	2.4

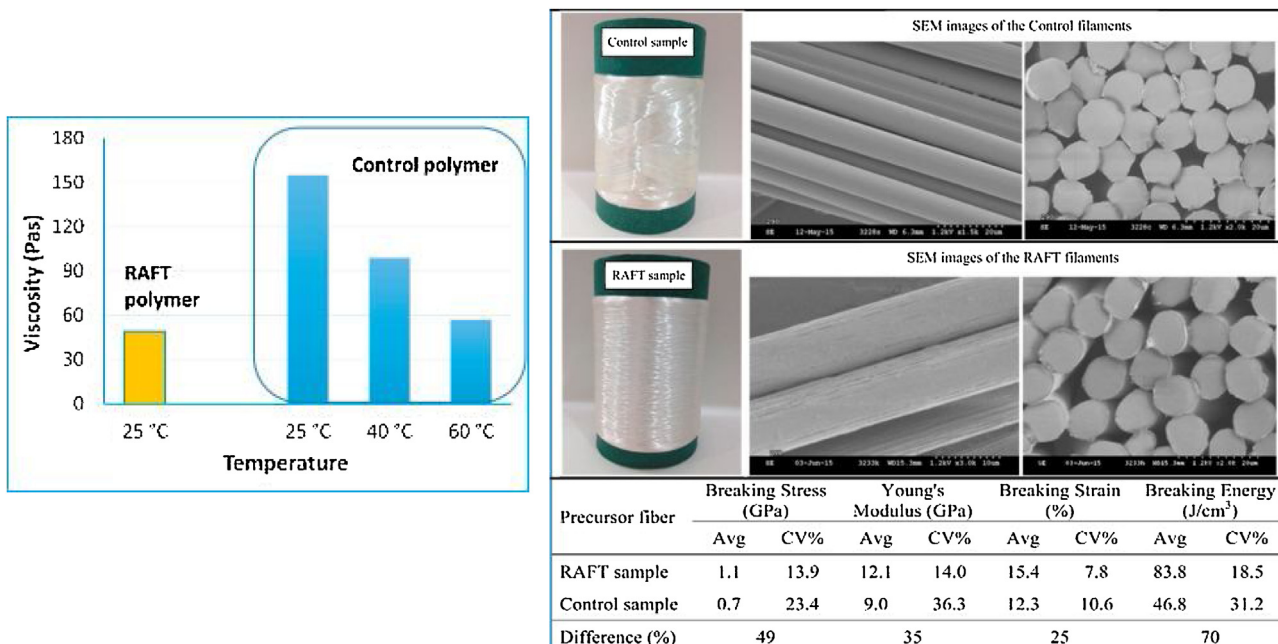
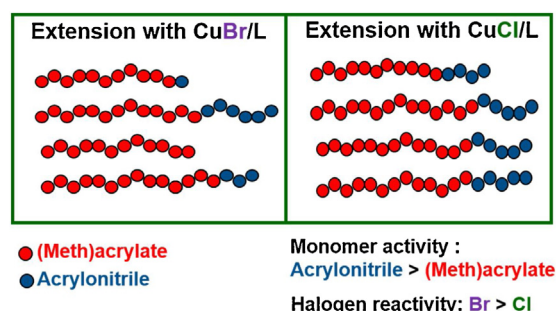


Fig. 9. Top: Viscosity of poly(AN-co-IA-co-MA) synthesized by RAFT and FRP in DMAA (polymer content 15 wt %) measured at different temperatures at a 1 s^{-1} shear rate. Bottom: Spools of the wet-spun precursor fibers, SEM images showing the fiber surfaces and cross sections, and mechanical properties of the precursor fibers. [180], Copyright 2016. Reproduced with permission from Elsevier.

allowing for facile preparation of block copolymers (BCPs) [112,113,184]. Synthesis of well-defined BCPs by any RDRP technique requires high chain-extension efficiency, which depends on the block sequence. Specifically, the more active monomer (i.e. with weaker C-X bond) has to be polymerized first and then extended with the less active one; otherwise a BCP with a broad MWD will form due to slow re-initiation efficiency [101]. For example, in ATRP activity is mostly influenced by the monomer's polarity and decreases in the following order: AN > methacrylates > acrylates/styrenes > acrylamides. Hence, a PAN macroinitiator can be extended with (meth)acrylate monomers and maintain good control over the synthesis of the second block. However, in the reverse sequence of block formation, a (meth)acrylate-based macroinitiator extended with AN usually exhibits poor control. [185]. In order to attain high chain-extension efficiency, the rate of cross-propagation should be comparable to the rate of the subsequent propagation reaction, i.e. the rate of the (meth)acrylate addition to the PAN macroinitiator must be at least the same as the addition of the methacrylate to itself [186].

In ATRP however, chain extension from less active to more active monomer can be achieved with good chain-extension efficiency by employing a halogen exchange technique (Scheme 7) [186–188]. K_{ATRP} depends on the strength of R-X bond and alkyl halide reac-



Scheme 7. Schematic illustration of a chain extension of Br-terminated PAN with (meth)acrylate monomer by ATRP with and without the halogen exchange.

tivity decreases in the following order: I > Br > Cl > pseudohalides. Thus, chain extension from Br-terminated polymer chains using CuCl/L catalyst complex will result in an exchange of Br chain end with a less active Cl. The rate of cross-propagation for a bromine-terminated (meth)acrylate is comparable to the propagation rate for chlorine-terminated AN, due to lower dissociation energy of the C-Br bond than the C-Cl bond [187]. The use of halogen exchange allows a well-defined BCP to be synthesized using ATRP without following the above mentioned block order. In the NMP and RAFT

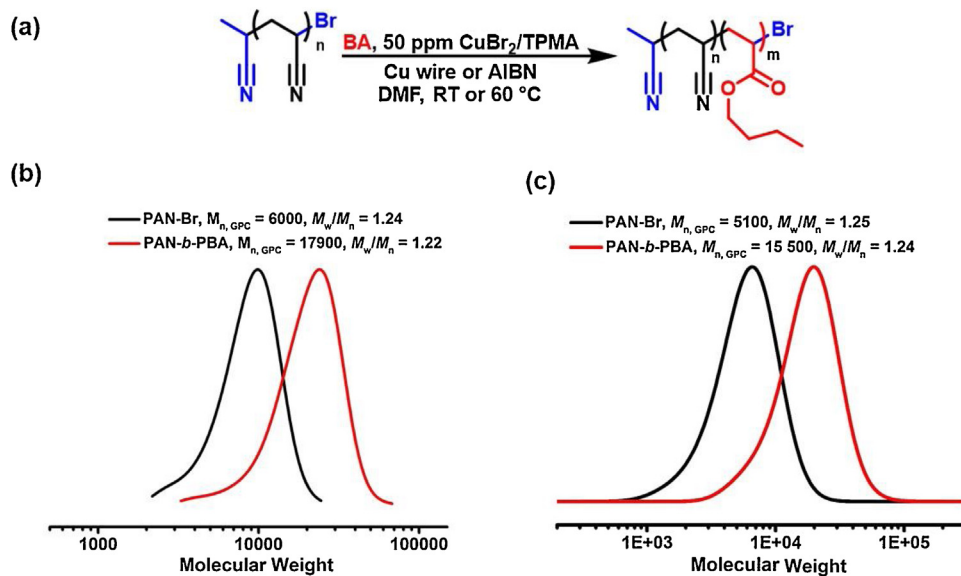


Fig. 10. (a) Reaction scheme of chain extension of PAN macroinitiator with *n*-butyl acrylate by ICAR or SARA ATRP using 50 ppm of CuBr₂/TPMA catalyst; GPC traces for chain extension of (b) (AN)₁₂₄-Br to yield AN₁₂₄-b-BA₇₇ by ICAR ATRP, (c) (AN)₈₆-Br to yield (AN)₈₆-b-BA₃₄ by SARA ATRP. [121][141]. Copyright 2016. Reproduced with permission from American Chemical Society and John Wiley and Sons.

it is difficult to alter this order as similar techniques cannot be introduced [112,184]. An additional issue, when synthesizing PAN-containing BCPs, is PAN's low solubility. Generally, only highly polar solvents, such as DMSO or DMF, can be used as the reaction media [67]. Furthermore, PAN is not soluble in AN and other (meth)acrylic monomers, making synthesis of BCPs difficult due to precipitation of the PAN macroinitiator.

PAN with high CEF can be prepared and chain-extended with BA in homogeneous DMF solutions of to form a BCP. However, PAN macroinitiators with higher MW partially lost solubility, tending to form a heterogeneous system while starting from a poly(*n*-butyl acrylate) (PBA) macroinitiator and using the halogen exchange technique resulted in better control over the polymerization of AN and synthesis of well-defined BCPs [44,132]. Even though the chain-extension from PAN to BA had higher efficiency than the opposite direction, the chain-extension from PBA to AN was more practical, because the low solubility of PAN necessitates a large excess of solvent to ensure PAN does not precipitate during the chain extension. Poly(*t*-butyl acrylate)-*b*-poly(acrylonitrile) (PtBA-*b*-PAN) was synthesized in a similar way, except a Cu^I/bpy catalyst was used for extension of PtBA-Br with AN, instead of CuCl/bpy [189].

PAN-*b*-PS BCPs with relatively narrow MWD ($D = 1.32$) were synthesized using CuBr/PMDTA catalyst and 2-cyanopyridine as solvent for both reaction steps [126]. Poly(2-methoxyethyl acrylate)-*b*-polyacrylonitrile (PMEA-*b*-PAN) was synthesized using CuBr/PMDETA as the catalyst to polymerize MEA in bulk at 60 °C and chain extending it with AN using halogen exchange ATRP (CuCl/bpy catalyst) in ethylene carbonate at 70 °C. Well-defined PMEA-*b*-PAN with $M_{n,NMR}$ up to 29,500 and D values ranging from 1.19 to 1.29 was synthesized [190]. Well-defined PAN-*b*-PMMA BCPs with low dispersities were also synthesized by normal ATRP in DMF [191–193].

One disadvantage of halogen exchange is that it requires high catalyst loadings (>1000 ppm) to provide a sufficient amount of halogen to exchange the macroinitiator chains. Excessive purification techniques are then necessary in order to remove the residual metal catalyst, especially when the polymer is meant to be used as a precursor to carbon materials. Thus, recently conditions were developed to reduce the amount of copper catalyst used in the synthesis of PAN-*b*-PBA BCPs by employing ICAR [121] and SARA ATRP

[141] for chain extension of PAN-Br macroinitiator with BA. Using only 50 ppm (vs monomer) of CuBr₂/TPMA catalyst and excess of DMF, clean chain extension with excellent chain-extension efficiency was observed at 65 °C or room temperature by ICAR and SARA ATRP, respectively (Fig. 10). BCPs with compositions perfectly matching the theoretical values were obtained, as confirmed by ¹H NMR.

2.5.2. RAFT and NMP

The relative reactivity of various classes of monomers is different in RAFT polymerization than in ATRP, as they are mostly influenced by steric effects rather than polarity, as in ATRP. Moreover, in RAFT not only the block sequence should be obeyed, but also the CTA must be suitable for both co-monomers, which makes synthesis of PAN-based BCPs more challenging [184]. For example, dithiobenzoate-terminated PAN extended with BA in aqueous NaSCN formed BCPs with high dispersities, $D \tilde{=} 1.60$. However, this was not due to poor CEF, as the same samples showed excellent chain extension with AN, but because of low activity of dithiobenzoate in polymerization of acrylates [160,194]; Conversely, dibenzyl trithiocarbonate as the CTA was demonstrated to yield well-defined PAN-*b*-PBA with low dispersity ($D = 1.16$) [155]. Poly(acrylic acid)-*b*-polyacrylonitrile (PAA-*b*-PAN) BCPs with different ratios of the two blocks was synthesized using 2-dodecylsulfanylthiocarbonylsulfanyl-2-methyl propionic acid (DMP) as the RAFT agent [195]. Additionally, RAFT polymerization was used to synthesize poly(acrylonitrile-*b*-cysteamid acrylate) (PAN-*b*-PCAA) using (DMP) as a CTA [196].

A combination of RAFT and ATRP was used to synthesize three types of graft copolymers with PAN and poly(*N*-isopropylacrylamide) (PNIPAM): PAN-*b*-PNIPAM, PAN-*b*-(PHEMA-g-PNIPAM), and PAN-*co*-(PHEMA-g-PNIPAM) [197]. Thin films of the PAN/PNIPAM copolymers were investigated to confirm the thermoresponsive nature and the surface wettability of the surfaces.

In NMP, the presence of excess SG1 played an important role in controlling the chain-extension efficiency for PAN-*b*-PBA BCP [132]. The presence of excess SG1 increased the initial rate of deactivation and finally resulted in lower dispersities ($D = 1.18$) of the BCP. However, the cross-propagation from PAN to BA was less efficient than

that from PBA to AN [132]. NMP was not reported for the synthesis of any other PAN containing block copolymers.

2.6. Grafting from surfaces

With the advent of RDRP, grafting polymer chains from various initiator-functionalized materials, such as planar substrates or NPs, has emerged as a versatile way of surface modification and preparation of hybrid particles. Surface-initiated ATRP (SI-ATRP) of acrylonitrile was employed to graft PAN from three different types of mesoporous silica (pore diameter 10–15 nm), namely 2-dimensionally hexagonally ordered with cylindrical pore (SBA-15), face centered cubic (fcc) with spherical pores (FDU-1) and disordered silica [198–201]. The silica surface was first modified with 3-(chlorodimethylsilyl)propyl 2-bromoisobutyrate to introduce initiating sites. PAN was then grafted inside the pores using CuCl/bpy catalyst in DMF at 55 or 35 °C. Gradual filling of the pores was monitored by measuring the area pore size distributions (for PAN in dry state) after each modification step (Fig. 11). Silica was subsequently etched with HF and isolated PAN chains were analyzed by GPC showing very low dispersities 1.06–1.34 and grafting densities 0.17–0.28 chains/nm². PAN grafted on silica surface was then used as a precursor for mesoporous carbons, see Section 3. PAN was also successfully grafted from colloidal silica NPs ($d = 16\text{ nm}$) that were functionalized with 2-bromoisobutyrate (BiB) groups. The silica particles were etched with HF and the PAN chains had degree of polymerization (DP)=280 and D of 1.06 or DP=220 and D of 1.31. The SiO₂-g-PAN was then used to make nanostructured carbon films [202].

Cross-linked PMMA (x-PMMA) synthesized by microemulsion ATRP was used to form ‘all-organic’ particle brushes [203]. After microemulsion AGET ATRP of MMA the active Br-chain ends accessible on the surface of the x-PMMA were chain extended with AN. Dynamic light scattering (DLS) analysis confirmed successful PAN grafting as the size increased from 24 nm to 50 nm. The x-PMMA-g-PAN particles brushes were pyrolyzed to form nanostructured carbon (Fig. 12).

Particle brushes were also synthesized by grafting PAN from Fe₃O₄ particles by surface-initiated RAFT polymerization. The Fe₃O₄-g-PAN particles showed improved solubility. Magnetic carbon fibers were prepared by coaxially spinning the magnetic nanoparticle brushes with PAN homopolymer and then carbonizing the fibers [204]. ATRP of AN from a POSS core that contained eight ATRP initiating sites was reported. Each arm had a low DP (<10) and low dispersity ($D < 1.38$). The POSS-g-PAN hybrids were introduced into Nafion® film and used as methanol fuel cell membranes [205]. In addition, SI-ATRP was used to graft PAN from other polymeric supports, such as cross-linked vinyl benzyl chloride or PVC fibers. These materials were used as sorbents for removal of uranium and other heavy metals from seawater [206–209].

Synthesis of PAN-grafted graphene oxide (GO-g-PAN) via *in situ* FRP was realized by directly polymerizing AN in a DMF dispersion of GO (Fig. 13) [210]. Upon removal of the free polymer from solution, the composites were characterized by atomic force microscopy (AFM) and determined that the thickness of the brushes varied in the range of 1.7–3.7 nm, depending on the molar ratios of monomer/initiator. Successful grafting was confirmed by thermogravimetry (TGA), X-ray photoelectron spectroscopy (XPS), SEM and TEM (Fig. 14). The weight loss visible in TGA below 250 °C was attributed to decomposition of oxygen-containing groups in the GO, before the typical PAN crosslinking/decomposition at 270–280 °C, and the PAN content in the composites was calculated to be 13.8–25.8 wt.%. Interestingly, the composites were found to form lyotropic liquid crystals and were used to wet-spin nacre-mimetic fibers. These fibers were micrometer-scale in diameter and

displayed improved tensile strength and Young's modulus due to the presence of aligned GO sheets.

3. Templating PAN to form Nanocarbons

3.1. Nanostructured carbon films

First reports on using PAN as precursor to ultrathin nanocarbon films date back to the late 1980s. In the pioneering works, Kyotani, Sonobe and Tomita prepared single graphite sheets from PAN carbonized between intercalated montmorillonite lamellae. Such a confinement during carbonization prevented three-dimensional cross-linking and allowed to obtain highly graphitized, two-dimensional structures with large crystallite size (up to 40 nm) [211–213].

Since the early 2000s, well-defined PAN and its copolymers have been used as precursors to various nanostructured carbon materials. The capability of ATRP to prepare a large variety of precisely tailored BCPs combined with the unique carbonization chemistry of PAN was envisaged as a route to nanocarbons with different architectures. Specifically, a series of PAN-containing BCPs were investigated. The developed approach was based on self-assembly of BCPs into various phase-separated morphologies driven by immiscibility of both blocks, described by the Flory-Huggins interaction parameter χ . For symmetrical di-block copolymers morphologies such as spheres, cylinders, lamellae or gyroids are usually observed whereas more complicated structures were described for triblock copolymers [214]. PBA was chosen as a second block due to its high incompatibility with PAN ($\chi = 0.85$) and relatively low decomposition temperature of 400 °C [215]. According to the self-consistent field theory [216], phase separation in symmetrical di-block copolymer systems occurs for $\chi \cdot DP \geq 10.5$, thus the minimal DP required to achieve phase separation in the PBA-*b*-PAN system was calculated to be 13 [215].

In the initial proof-of-concept study, a triblock copolymer (AN)₄₅-*b*-(BA)₅₃₀-*b*-(AN)₄₅ was synthesized by ATRP and a thin film of a DMF solution was deposited onto a silicon wafer. Upon thermal annealing under vacuum at 220 °C followed by pyrolysis at 600–1200 °C, carbon films were formed with spherical morphology corresponding to the annealed copolymer (Fig. 15). At this temperature the PBA block undergoes decomposition while pyrolysis of PAN leads to formation of isolated carbon spheres [44].

The self-assembly of PAN-containing copolymers was further explored by synthesizing a library of PBA-*b*-PAN diblock copolymers with various block ratios [217]. AFM was used to demonstrate the evolution of BCP morphology from spherical via cylindrical to branched as the PAN fraction in the copolymer increased. The PBA-*b*-PAN films were heated under air at 280 °C to stabilize the PAN domains and subsequently heated under nitrogen at 800 °C to convert PAN into carbon and to volatilize the PBA domains. As shown in Fig. 16, the BCP morphologies were preserved upon carbonization and led to carbon films with tunable nanostructure and domain spacing. Importantly, it was demonstrated that phase separation was not retained in films carbonized without an initial stabilization step and resulted in formation of a disordered morphology [215]. The stabilization step was recognized to be crucial for ‘fixing’ the self-assembled morphology by cross-linking the PAN phase before the onset of PBA degradation.

Furthermore, this approach was extended by introducing a zone-casting method to fabricate PBA-*b*-PAN or PAN-*b*-PBA-*b*-PAN films with a long-range lamellar order [218]. Zone-casting deposits a DMF solution of PAN-*b*-PBA onto a moving substrate (Fig. 17). The syringe temperature, deposition rate, and rate of substrate movement were adjustable, allowing for control over film thickness (tens of nanometers to several micrometers) and film size (several square

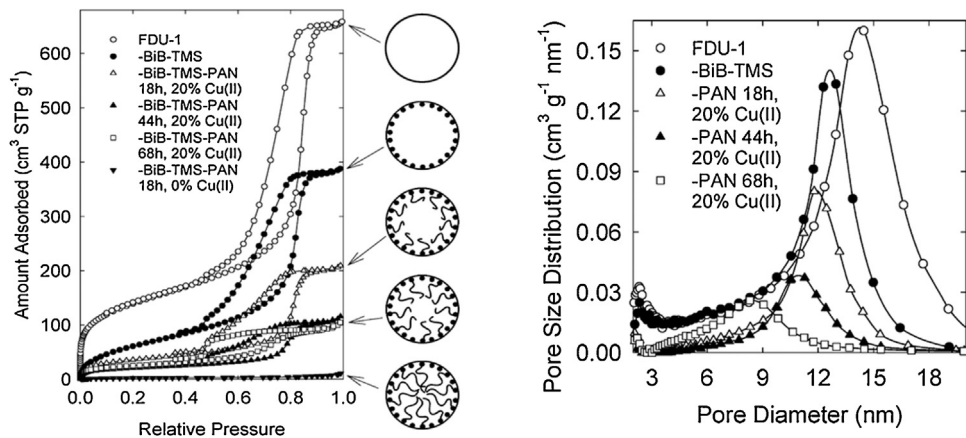
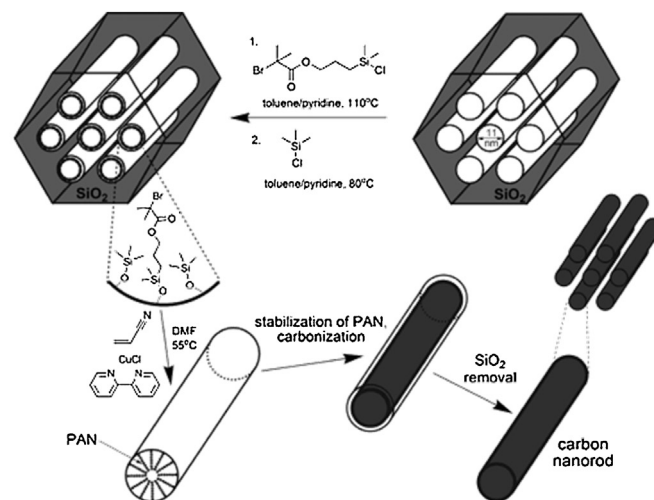


Fig. 11. Top: Synthesis of ordered mesoporous carbon using a silica template precursor formed via surface-initiated ATRP. Nitrogen adsorption isotherms (bottom left) and pore size distributions (bottom right) for FDU-1 silica before and after bonding of 2-bromoisobutyrate groups and trimethylsilyl groups (-BiB – TMS) and after AN polymerization for different periods of time. The schemes illustrate the stage of the synthesis corresponding to the particular adsorption isotherm. [198], [200], Copyright 2016. Reproduced with permission from American Chemical Society.

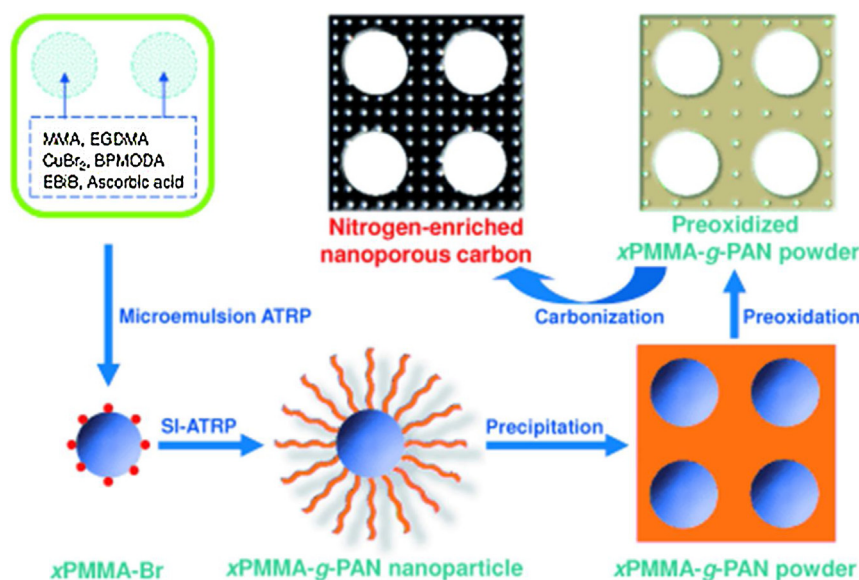


Fig. 12. Templated synthesis of nitrogen-enriched nanoporous carbons using all-organic hairy NPs as building blocks. [203]. Copyright 2014. Reproduced with permission from John Wiley and Sons.

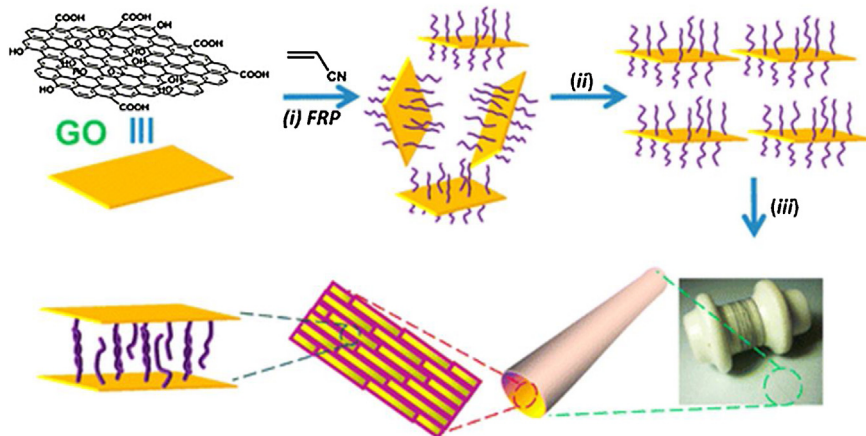


Fig. 13. (i) Synthesis of GO-g-PAN building blocks (ii) Prealignment of GO-g-PAN in lamellar phase in DMF. (iii) Formation of hierarchically assembled continuous GO-g-PAN fibers via wet-spinning. [210], Copyright 2013. Reproduced with permission from American Chemical Society.

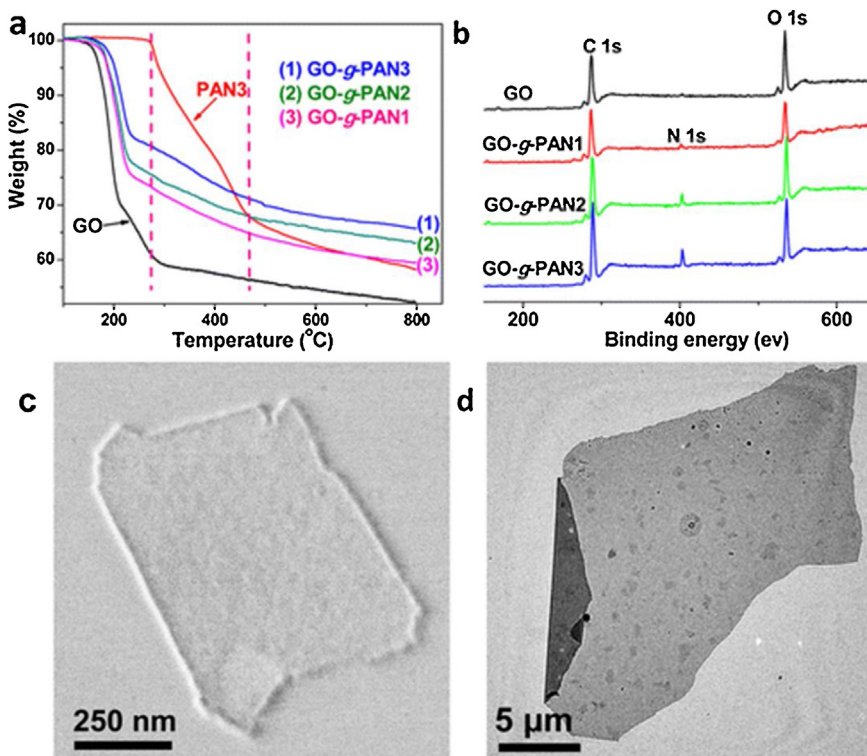


Fig. 14. (a) TGA curves for samples of neat PAN, GO, and GO-g-PANs. (b) XPS spectra of GO and GO-g-PANs. Representative SEM (c) and TEM (d) image of single-layer GO-g-PAN. [210], Copyright 2013. Reproduced with permission from American Chemical Society.

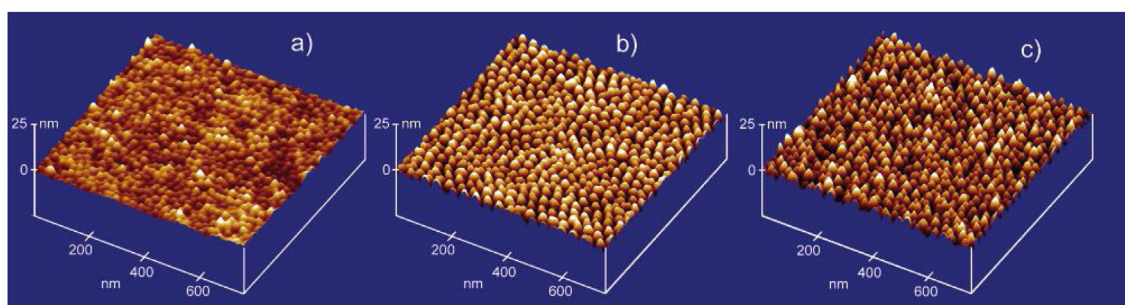


Fig. 15. Tapping-mode AFM images illustrating the effect of thermal treatment on the evolution of nanoscale morphology of ultrathin ($d < 50$ nm) films of $(AN)_{45}-b-(BA)_{530}-b-(AN)_{45}$ triblock copolymer spin-coated onto a silicon wafer. (a) Sample vacuum-annealed for 2 h at 220 °C to equilibrate the morphology; (b) sample heated under nitrogen at 20 °C/min from room temperature to 600 °C and (c) to 1200 °C. [44], Copyright 2002. Reproduced with permission from American Chemical Society.

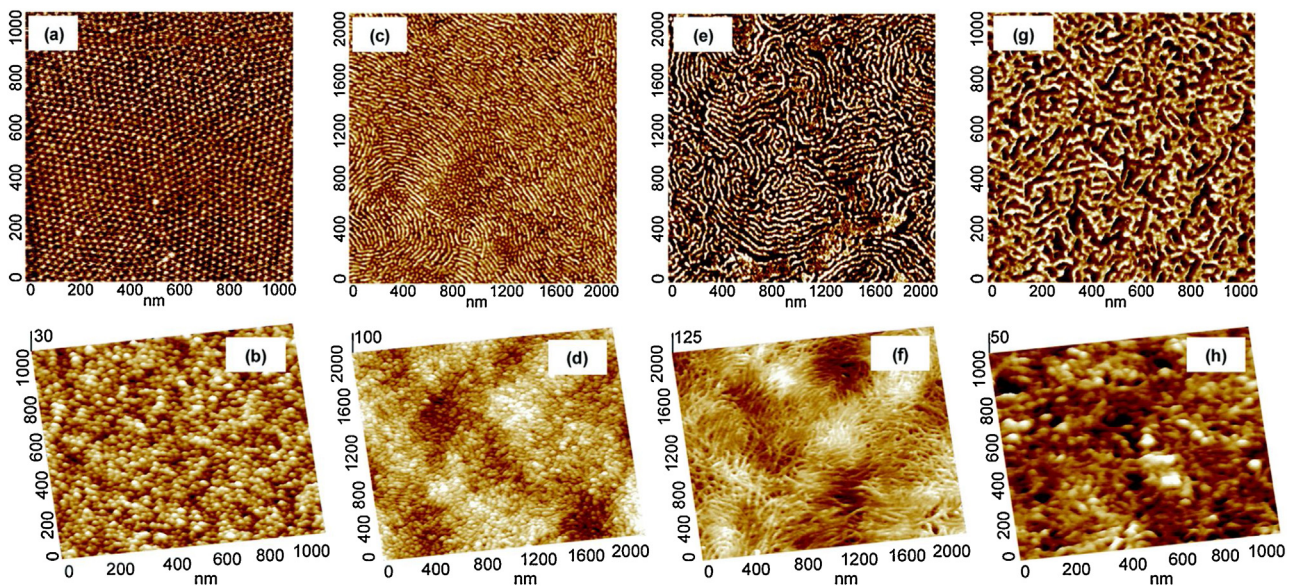


Fig. 16. Tapping mode AFM phase images (top) of thin films of PAN-*b*-PBA block copolymers prepared by drop-casting and height images (bottom) of the resulting carbons after pyrolysis under N₂ at 600 °C. (a) (BA)₂₄₀-*b*-(AN)₃₆ (5.8 wt% PAN); (b) carbon from (BA)₂₄₀-*b*-(AN)₃₆; (c) (BA)₂₄₀-*b*-(AN)₁₀₄ (15.2 wt% PAN); (d) carbon from (BA)₂₄₀-*b*-(AN)₁₀₄; (e) (BA)₂₄₀-*b*-(AN)₁₂₄ (17.6 wt% PAN); (f) carbon from (BA)₂₄₀-*b*-(AN)₁₂₄; (g) (BA)₇₈-*b*-(AN)₁₁₄ (37.7 wt% PAN); (h) carbon from (BA)₇₈-*b*-(AN)₁₁₄. [217], Copyright 2014. Reproduced with permission from Royal Society of Chemistry.

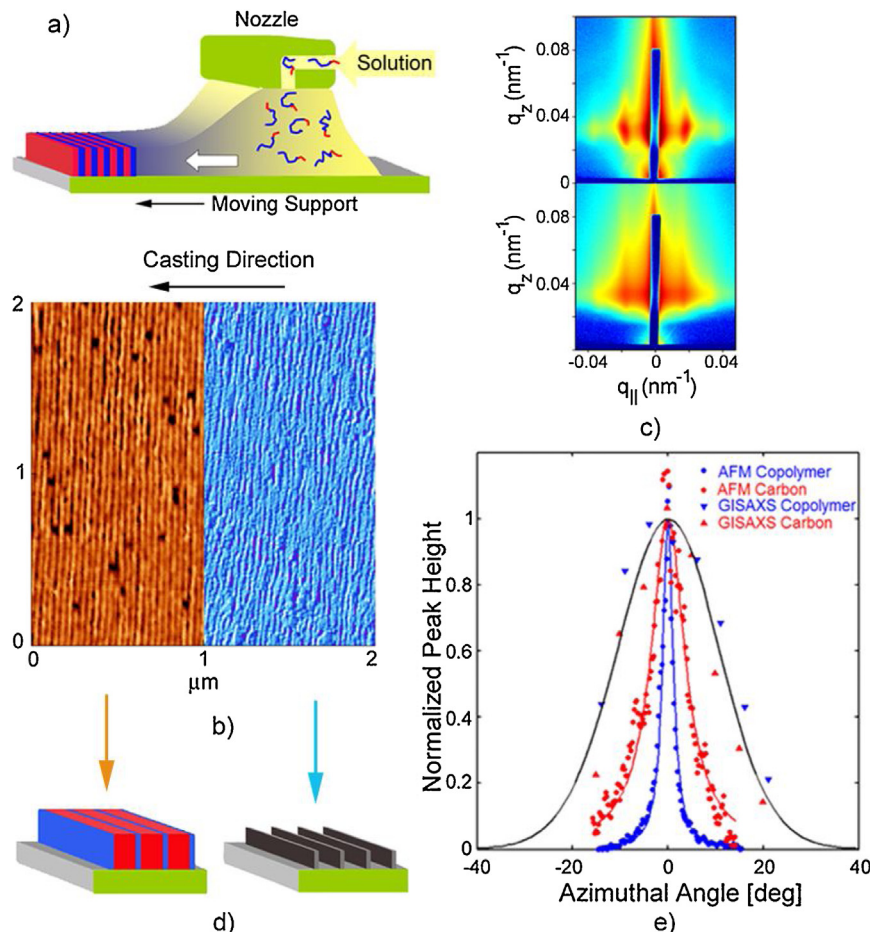


Fig. 17. (a) Long-range order in thin films of PBA₂₄₀-*b*-PAN₁₂₄ BCPS prepared by zone-casting and pyrolysis to form nanostructured carbon; (b) AFM phase images (left: copolymer; right: carbon); (c) GISAXS patterns acquired at 90° to casting direction (top: copolymer; bottom: carbon); (d) schematic illustration of lamellar order (left: copolymer; right: carbon); (e) azimuthal profiles of maxima in 2D Fourier transforms of AFM images and maxima in GISAXS patterns corresponding to the lamellar period. [218], Copyright 2005. Reproduced with permission from American Chemical Society.

cm). A (BA)₂₄₀-*b*-(AN)₁₂₄ precursor was zone-cast from a DMF solution and the resulting film exhibited an edge-on lamellae structure with a domain-spacing (d-spacing) of 36 nm, as determined using grazing incidence small-angle X-ray scattering (GISAXS) and AFM (Fig. 17). The lamellae were oriented perpendicular to the casting direction, indicating that the solvent evaporation front induced the domain formation. Commonly used drop-casting technique afforded PBA-*b*-PAN films with only short-range, locally ordered lamellae. Upon stabilization and carbonization, a lamellar carbon film was obtained that exhibited the same spacing ($d = 37$ nm) as the copolymer film and preserved orientation of lamellae. The remarkable ability of the BCP to retain the orientation upon carbonization was assigned to the oxidative stabilization step which, similarly to carbon fibers, helped to fix the phase-separated lamellar morphology by crosslinking of the PAN phase. However, if removed from the substrate, the d-spacing decreased and carbon orientation was lost due to collapse of the carbon structure.

In a following investigation, phase separation of PAN-*b*-PS copolymers and their transformation into nanoporous carbon films was examined. SAXS analysis of PS-*b*-PAN showed small d-spacing of 12–14 nm, however with disordered morphology [219]. Another early work studied bulk phase separation and carbonization of PCL-*b*-PAN BCPs. At volume fraction $f_{\text{PAN}}^V = 0.6$, the BCP showed lamellar morphology, whereas a hexagonal cylindrical structure was observed for $f_{\text{PAN}}^V = 0.33$, as confirmed by TEM and SAXS. Both thermal and hydrolytic removal of the sacrificial PCL block was attempted, however in the latter case hydrolysis also resulted in etching of the PAN. Mesoporous carbons were obtained upon further pyrolysis at 800 °C, however, the collapse of carbon matrix was observed, suggesting that a careful optimization of the morphology would be necessary for the successful preparation of stable bulk mesoporous carbon by soft templating (see Section 3.4.2) [220]. Very recently, RAFT-synthesized PAN-*b*-PMMA with high MW (>160,000) was used to spin cast ultrathin films, with thicknesses of 6–8 nm [221]. It was shown that adjusting the stabilization temperature between 100 and 300 °C provided control over the surface patterns, however within a limited range (40–50 nm) as only one BCP composition was used. The pore sizes were well-preserved upon carbonization of the films at 800 °C. Additionally, annealing in different solvents, DMF, DMSO, toluene, chloroform was shown to have some influence on pore size of both BCP and carbonized films.

3.2. Discrete carbon nanoobjects

The initial studies, which enabled morphology preservation upon pyrolysis of PAN-based films deposited on solid substrates, were then successfully employed to prepare free-standing carbon materials. Self-assembly of PAN-containing BCPs was investigated in solution as a route to carbon NPs by pyrolysis of PAN-based micelles [222]. The preparation of PtBA-*b*-PAN BCP and subsequent hydrolysis of the PtBA block to PAA yielded a PAA-*b*-PAN amphiphilic copolymer (Fig. 18). Upon micellization in water, the PAA phase was crosslinked with 2,2'-(ethylenedioxy)-bis(ethylamine) to form shell cross-linked micelles (SCKs) with uniform distribution of heights (average height of 9 ± 0.5 nm). The SCKs were then pyrolyzed to form carbon NPs. After carbonization, the carbon nanospheres were observed by AFM with a decrease in height from the SCKs, which can be related to the volatilization of the cross-linked PAA shell and carbonization of PAN block (Fig. 19).

RAFT was used to directly synthesize micelles of PAA-*b*-PAN copolymers in water [195]. The PAN core was cross-linked/loaded with HAuCl₄ by complexation between Au and nitrile groups. HAuCl₄ was subsequently reduced by NaBH₄ to form gold NPs inside the micelles. Interestingly, upon pyrolysis carbon nanocap-

sules were formed and energy dispersive X-ray spectroscopy (EDX) analysis did not detect any signals from gold what was attributed to melting of the NPs and diffusion of molten gold out of the graphitizing micelles. AFM and TEM analysis revealed that the carbon nanospheres have similar size to the initial gold cross-linked micelles, 30–35 nm, Fig. 20.

Taking advantage of strong phase separation in PAN-*b*-PS and PAN-*b*-PMMA copolymers into cylindrical micelles in chloroform/DMF, worm-like carbon nanofibers with 35–50 nm in diameter were prepared (Fig. 21) [223]. The addition of PAN homopolymer to the BCP solution was demonstrated to greatly influence the morphology and led to formation of 'giant' worm-like micelles ($\phi > 100$ nm). Additionally, as in the case of BCP films, it was found that the fibrous morphology was only preserved upon carbonization when oxidative stabilization was performed on the precursors prior to pyrolysis.

An alternative approach to synthesize carbon nano-objects was realized by the use of more sophisticated polymer architectures, namely molecular bottlebrushes. Well-defined molecular brushes containing PAN-based segments in the side chains were prepared by ATRP using a "grafting from" technique [225]. Poly(2-(2-bromoisobutyryloxy)ethyl methacrylate) was prepared by RAFT and used a brush backbone, and a triblock PBA-*b*-PAN-*b*-PtBA copolymer was then grafted as side chains to form the brush. Due to solubility of the side chains in polar DMF solvent, these brushes displayed collapsed, worm-like structures after deposition on surfaces, as observed by AFM. Interestingly, brushes with ABC tri-block copolymer side chains (PBA-*b*-PAN-*b*-PtBA) had a necklace-like structure, which can be attributed to the strong interaction between the terminal PtBA block and inner PBA block. The outer PtBA block was then hydrolyzed to obtain PAA and crosslinked. The brush copolymers were used as template molecules for preparation of nanostructured carbons. Single shell crosslinked brushes exhibited a high stability during pyrolysis to form single carbon nano-objects. Therefore, the shell cross-linked brushes with rigid structures were subjected stabilization at 250 °C and subsequently pyrolyzed at 600 °C. The height of the structures after thermal stabilization was determined to be 11.6 nm. The carbon nanostructures preserved the shape of the original shell cross-linked brushes, although slight shrinking was observed, due to the thermal treatment. The height was relatively low, 5.4 nm, and the rounder shape, compared to typical rod-like structures of bottle brushes, was due to the low aspect ratio of backbone length to the side chain length after shell crosslinking of the brushes. A multilayer carbon was then prepared by depositing a thicker film of the crosslinked brushes (Fig. 22).

PAN-grafted colloidal SiO₂ NPs ($d = 16$ nm) enabled the formation of porous carbon films from individual hybrid nanoobjects [202]. Polymer-decorated, 'hairy' NPs were deposited on the silicon surface as relatively thick films (up to 1 μm) in order to allow surface area measurements. After carbonization the silica NPs were removed by HF etching. Porous carbon film was obtained with $S_{\text{BET}} = 450 \text{ m}^2/\text{g}$ and pore volume of 0.72 cm³/g. The pore size distribution was centered at 13 nm, close to the diameter of the silica templates.

Very recently an interesting method to synthesize PAN/carbon flower particles has been presented [226]. Taking advantage of poor solubility of PAN, acrylonitrile was polymerized by conventional FRP in various non-solvents and shown to form different morphologies upon precipitation. Importantly, when polymerized in a good solvent (DMF), no superstructure was observed. Upon applying the standard stabilization/pyrolysis procedure, carbon flower-like particles were obtained with preserved morphology of the template (Fig. 23). The morphology could be further tuned by copolymerizing with styrene, acrylic acid or MMA and the carbon flowers were

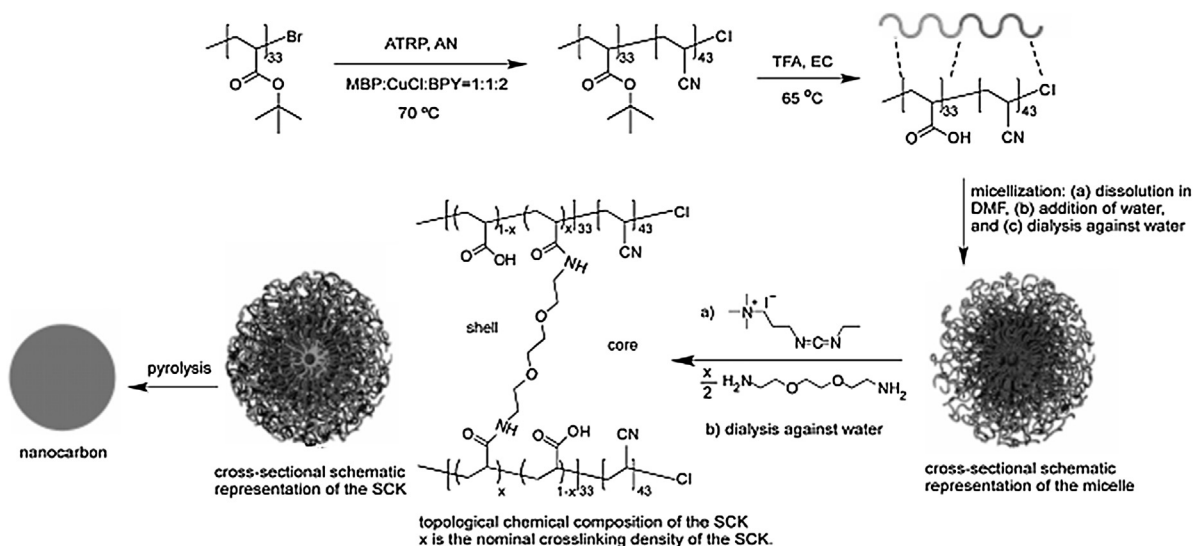


Fig. 18. Illustration of the five-step synthesis of carbon NPs: 1) formation of a diblock copolymer PtBA-*b*-PAN by ATRP; 2) formation of an amphiphilic block copolymer PAA-*b*-PAN; 3) formation of polymer micelles through self-assembly; 4) formation of SCKs after cross-linking of the shell layer of polymer micelles; 5) formation of nanostructured carbon particles through pyrolysis. [222]. Copyright 2004. Reproduced with permission from John Wiley and Sons.

transformed into microporous carbons by activation with CO₂ or NH₃.

3.3. Carbon nanofibers

Carbon nanofibers (CNF) are carbonized PAN or mesophase pitch fibers with diameter 10 nm < ϕ < 1 μm , as compared to traditionally spun micrometer-sized CFs (ϕ > 5 μm) [227–229]. PAN-based CNFs are typically prepared from commercial, high MW polymer via CVD or electrospinning and used as additives in nanocomposites. Besides smaller diameter, other desirable properties exhibited by CNFs include larger specific surface area (SSA) and lower onset temperature of stabilization. Additionally, CNFs can be prepared from PAN homopolymer instead of copolymers used for traditional CFs, and without any post-drawing processing.

ZnCl₂, a well-known activating agent for porous carbons, was used to provide control over the diameter and porosity of electrospun PAN nanofibers [230]. A free-standing, self-sustained web of PAN nanofibers was obtained, which was transformed into a carbon nanofiber of controlled size (Fig. 24) upon stabilization and pyrolysis at 800 °C. The addition of ZnCl₂ led to thinner nanofibers and larger SSA (up to 550 m²/g). These materials were then employed as supercapacitors (see Section 4).

Addition of FeCl₃ as a structure-directing agent during FRP of AN in microemulsion transformed PAN NPs, normally obtained without the salt addition, into nanofibers (Fig. 25) [231]. This effect was caused by coordination between the nitrile groups and the salt. The as-prepared nanofibers were then converted into CNFs by pyrolysis at 900 °C providing highly graphitic (80%) CNFs, with a diameter of 20 nm, which were used as additives to prepare conductive composites in an epoxy-based matrix.

CNFs were also successfully prepared by synthesis and graphitization of PAN inside the nanosized pores of inorganic templates such as sepiolite [232] or anodized aluminum oxide (AAO). By wetting the precursors of nanoporous AAO membranes with solutions of PAN or PS-*b*-PAN and subsequent carbonization, amorphous and porous carbon nanotubes, respectively, were fabricated [233]. Similarly, mesoporous carbon fibers were synthesized from PVAc-*b*-PAN BCPs by compressing them into an AAO membrane, carbonizing, and removing the AAO template [234]. The carbon nanotube's morphology was tuned by changing the block ratios or

the heating rate of pyrolysis and the wall thickness was controlled by changing the concentration of the BCP precursor solution or by using multiple casting/pyrolysis steps.

Electrospun PAN and multi-walled carbon nanotubes (MWCNT) composites with MWCNT loadings up to 35% were demonstrated [235]. The use of electrospinning was crucial to align MWCNTs along the fibers' axis and thus improved the mechanical properties, tensile strength and modulus, of the obtained composite. The composites were then stabilized and carbonized at 850 °C to prepare graphitic nanofibers with embedded MWCNTs.

Recently, 2D carbon mats and porous 3D scaffolds from electrospun PAN were prepared and used as biocompatible supports for human bone marrow-derived mesenchymal stem cells (Fig. 26) [236]. Nanofibers were spun either on a quartz plates (mats) or directly into a water bath (scaffold), followed by carbonization under argon at 800 °C. Biocompatibility and application of carbonized PAN in tissue engineering were investigated for the first time and outperformed traditionally-used CNTs, opening potential applications for the use of PAN in regenerative medicine.

3.4. Bulk mesoporous carbons

Porous carbons are ubiquitous group of materials used in gas purification, water filtration, metal extraction, catalysis and medicine. According to the International Union of Pure and Applied Chemistry (IUPAC), porous materials are divided into three groups depending on the pore diameter: microporous (ϕ < 2 nm), mesoporous (ϕ = 2–50 nm) and macroporous (ϕ > 50 nm). Large-scale production of porous carbons involves direct pyrolysis of precursors, like pitches (petroleum, coal, coal tar, coal chars, mesophase pitch), polymers or biomass. Physical (with CO₂, steam) or chemical (with KOH, NaOH or ZnCl₂) activation is used to generate porosity and surface areas of activated carbon exceeding 500 m²/g [237]. However, carbons prepared by these activation procedures are typically microporous and if they also contain mesopores, the latter exhibit broad size distribution. Synthesis of carbons with well-defined, ordered mesopores is more challenging and can be realized via two main routes, namely hard and soft templating.

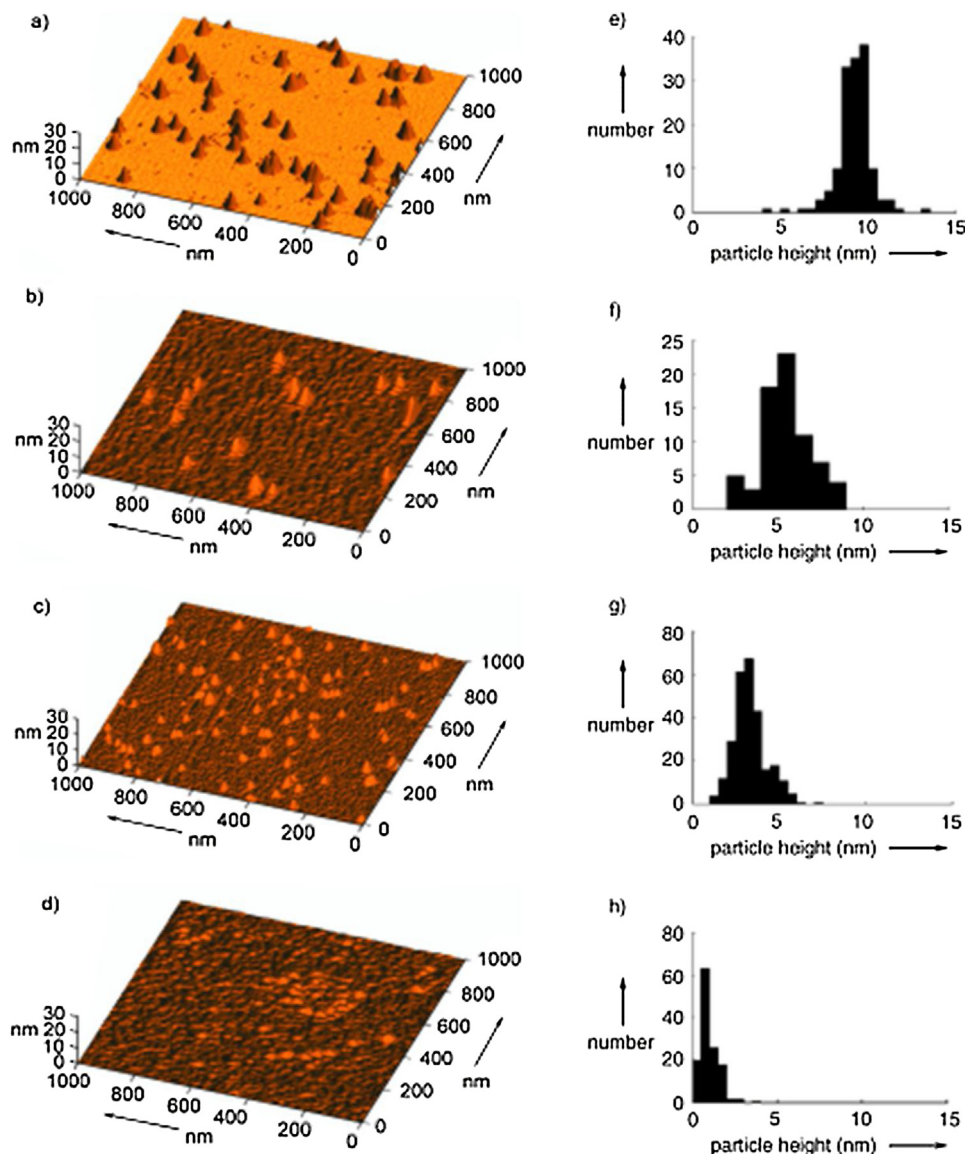


Fig. 19. a)–d) Tapping mode AFM images of NPs: (a) SCKs on mica; (b) NPs stabilized on mica in air at 230 °C for 2 h and (c) after heating under nitrogen at 20 °C/min from room temperature to 600 °C; (d) after pyrolysis of thermally stabilized SCKs on a silicon wafer, obtained by heating under nitrogen at 20 °C/min from 230 °C to 900 °C. (e)–(h) Height distributions of SCKs and carbon NPs determined from AFM images: (e) SCKs; (f) carbon NPs stabilized at 230 °C; (g) carbon NPs pyrolyzed at 600 °C and (h) carbon NPs pyrolyzed at 900 °C. [222], Copyright 2004. Reproduced with permission from John Wiley and Sons.

3.4.1. Hard templating

Hard templating relies on the use of inorganic templates, typically mesoporous silica that are impregnated with carbon precursor and subsequently removed after carbonization to create inverse replica pores [238–242]. First reported fabrication of mesoporous carbon from PAN used mesoporous silica templates, namely SBA-15 with 2-D hexagonal structure of cylindrical mesopores [243]. The template was impregnated with monomer which was then polymerized by conventional FRP. Upon stabilization at 200–250 °C and carbonization at 850 °C or 1100 °C followed by dissolution of the silica with aqueous HF, ordered mesoporous carbon was obtained. Voids with an average diameter of 3.5 nm between 2-D hexagonally ordered carbon nanorods in the structure of CMK-3 mesoporous carbon were observed for a sample stabilized at 250 °C and carbonized at 850 °C. Interestingly, decreasing the stabilization temperature to 230 °C and 200 °C resulted in formation of carbons with bimodal pore size distribution with respective maxima at 3.3 nm and 9.8 nm, the latter attributable to structural defects (Fig. 27). The obtained mesoporous carbons

possessed high SSAs, $S_{BET} > 800 \text{ m}^2/\text{g}$, as determined by nitrogen adsorption.

Three types of commercial colloidal silica were impregnated with AN vapors and polymerized by conventional FRP in an approach termed vapor deposition polymerization (VDP) [244]. Mesoporous carbons were then prepared by carbonization. As expected, the pore size increased from 6.1 nm to 7.3 nm and 9.1 nm for samples templated by larger particles with diameters of 7, 12 and 22 nm, respectively. This indicated less efficient templating than in the previous report, as confirmed by lower SSAs for the obtained carbons. The plausible reason is that the authors did not utilize the oxidative stabilization step to crosslink PAN before conducting carbonization at 900 °C, which resulted in poorly preserved morphology.

In a similar approach, ATRP-initiator-modified SBA-15 or FDU-1 silicas were used to prepare the PAN-grafted silica precursors of the mesoporous carbons [198]. The PAN content was crucial for the formation of well-defined ordered carbons. Samples with high extent of pore filling with PAN, which corresponded to high MW PAN

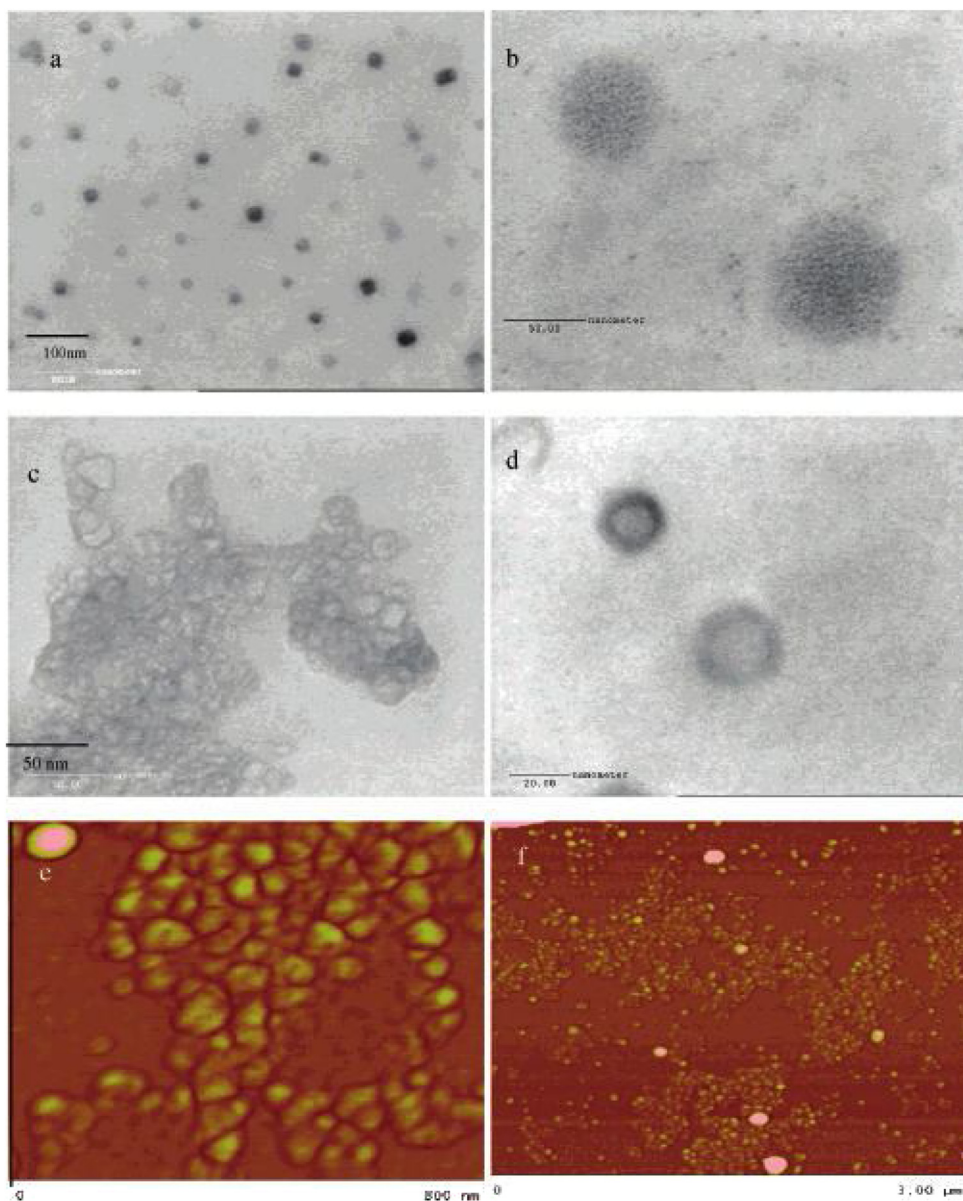


Fig. 20. Transmission electron micrographs of (a) (AA)₄₀-*b*-(AN)₁₂₈ micelles, (b) PAA₄₀-*b*-PAN₁₂₈ micelles after the gold loading of the PAN core, (c,d) carbon nanocapsules after pyrolysis, and (e,f) atomic force microscopy (tapping mode) of the carbon nano-objects deposited onto a silicon wafer. [195]. Copyright 2007. Reproduced with permission from American Chemical Society.

grafted from the silica using long polymerization times (1–2 days), yielded carbons with high SSA and pore volumes, $S_{\text{BET}} > 800 \text{ m}^2/\text{g}$, $1.4\text{--}1.5 \text{ cm}^3/\text{g}$, respectively. Carbons prepared from silica grafted with shorter PAN chains (2–4 h of reaction) had broad pore size distributions and were devoid of long-range periodicity, as seen from SAXS. For ordered samples, the pore size distributions revealed pores of 8–12 nm in diameter for samples stabilized at 300 °C and carbonized at 800 °C demonstrating efficient templating of mesoporous PAN-derived carbons by mesoporous silicas. This approach was later extended to prepare partially-graphitic carbons without the loss of mesoporosity by applying $T_p > 2000$ °C, typically used for carbon fiber synthesis. High temperature pyrolysis resulted in a moderate reduction of SSA (from 840 to 520 m^2/g) and pore volume (1.49 to $0.85 \text{ cm}^3/\text{g}$), however the obtained materials largely preserved the pore diameter, even if the pore size distribution was much broader in most cases. The partially-graphitic structure of obtained materials was confirmed by X-ray diffraction (XRD) and Raman spectroscopy [199]. SI-ATRP was also used to graft PAN

from large-pore (20–30 nm) SBA-15 with cylindrical mesopores and FDU-12 silica (fcc structure) with spherical mesopores [201]. Upon stabilization and pyrolysis, a mesoporous carbon consisting of hollow carbon nanospheres was obtained when FDU-12 template was used. High SSA of $810 \text{ m}^2/\text{g}$, a large pore volume of $1.98 \text{ cm}^3/\text{g}$ and bimodal PSD (reflecting void spaces within the nanospheres and between the nanospheres) were observed (Fig. 28).

Very recently, SI-ATRP was used to graft PAN from very small ($d = 3 \text{ nm}$) organosilica NPs synthesized by reduction of 6-(triethoxysilyl)hexyl α -bromoisobutyrate with ammonia in methanol (Scheme 8) [245]. The NPs were grafted with two different MWs of PAN (namely DP = 90 and 158) as confirmed by TGA measurements. Nanoporous carbons were then obtained from organosilica-g-PAN hybrids by standard procedure of stabilization/pyrolysis, followed by etching the silica with HF. N_2 sorption measurements showed type I adsorption isotherms, indicative of primary micropore filling and secondary micropore filling/capillary condensation (Fig. 29a). High SSAs, namely 467 and $1244 \text{ m}^2/\text{g}$ for

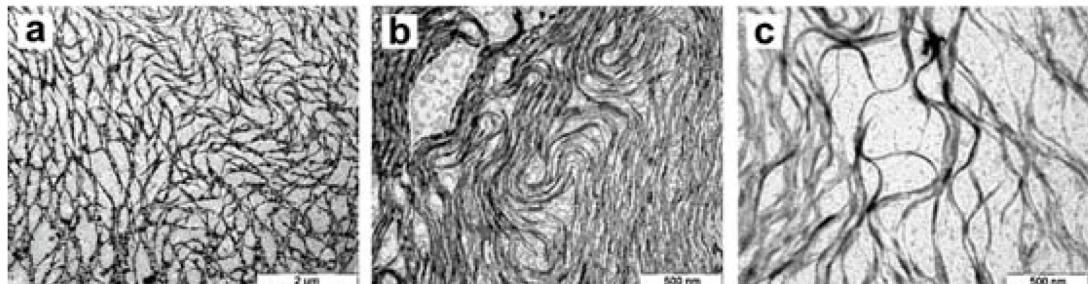
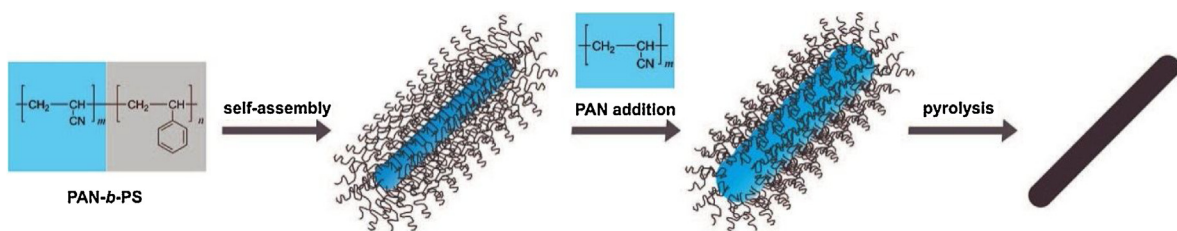


Fig. 21. Fabrication of carbon nanofibers from PAN-*b*-PS BCP templating; TEM images of micelles deposited onto carbon-coated copper grids from 1.0 mg/mL chloroform/DMF (9/1 by volume) solutions. TEM images refer to samples stained with RuO₄: (AN)₂₀-*b*-S₆₁ (a), (AN)₂₀-*b*-S₂₁₀ (b) and (AN)₂₀-*b*-(MMA)₂₆₀ (c). [223], [224]. Copyright 2007, 2008. Reproduced with permission from American Chemical Society and John Wiley and Sons.

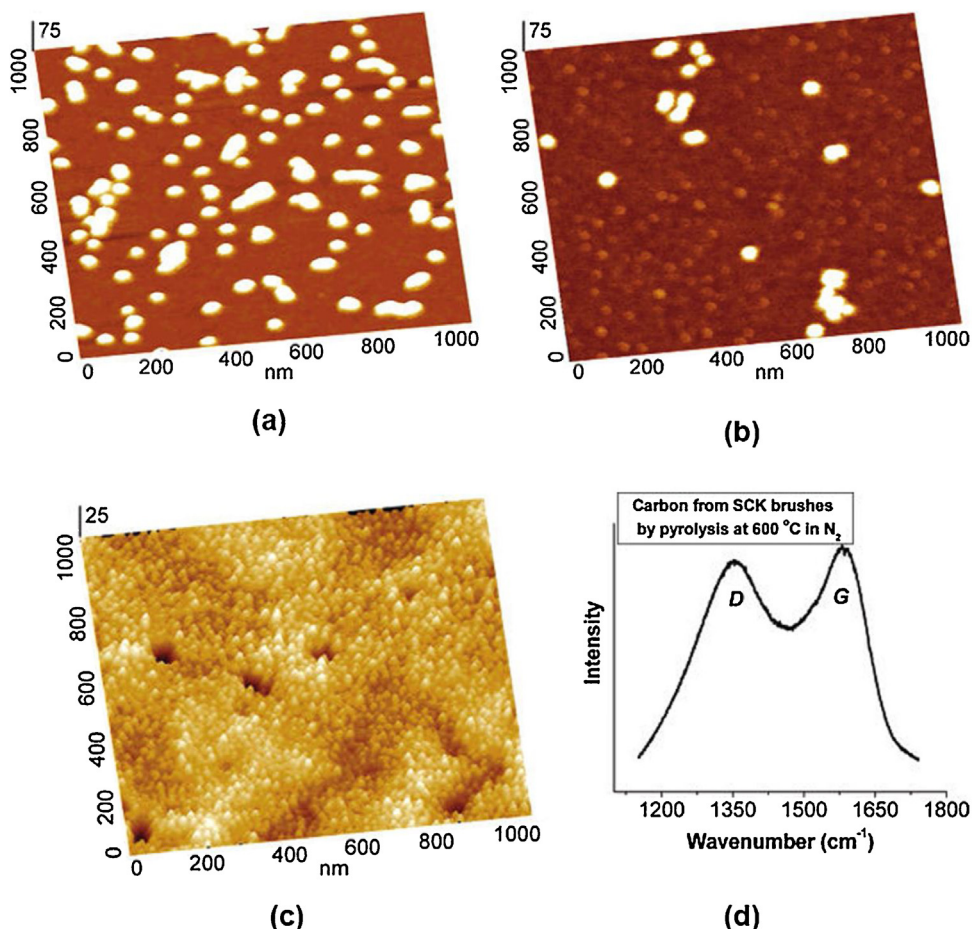


Fig. 22. AFM height images: (a) carbon nanorods by stabilization of molecular brush precursors at 250°C; (b) carbon nanorods by carbonization of stabilized precursors at 600°C. (c) AFM height image and (d) Raman spectrum of multilayer nanostructured carbon from thin film of shell-crosslinked brushes pyrolyzed at 600°C. [225]. Copyright 2007. Reproduced with permission from American Chemical Society.

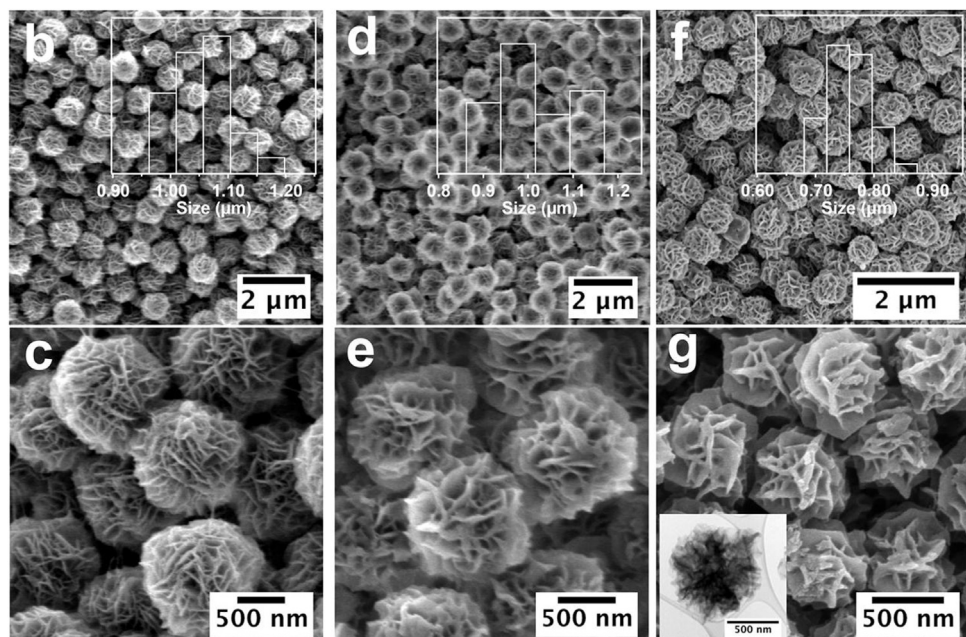


Fig. 23. SEM images of (b, c) PACN flowers (PACN-F), (d, e) stabilized PACN flowers at 230 °C (PACN-F-230C), and (f, g) carbonized PACN flowers formed at 1000 °C (PACN-F-1000C), at different scales, with histogram showing the size distribution. The TEM image of carbon flower was inserted in (g). [226], Copyright 2018. Reproduced with permission from the American Chemical Society.

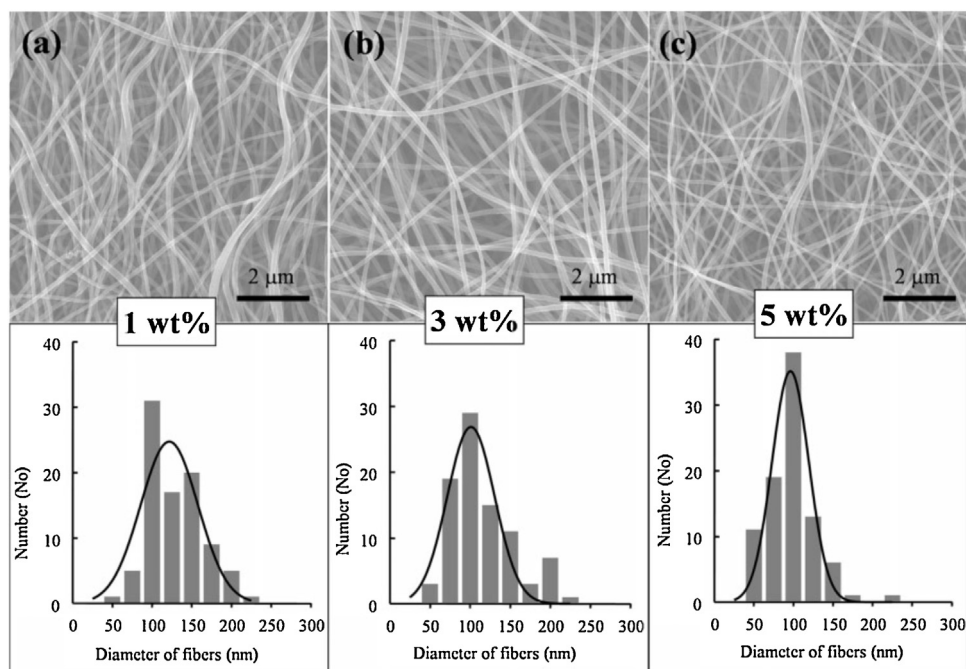


Fig. 24. SEM images of thermally treated nanofibers at 800 °C for 1 h and their corresponding diameter distributions: a) 1, b) 3, and c) 5 wt% ZnCl₂. [230], Copyright 2007. Reproduced with permission from John Wiley and Sons.

NPC-158 and NPC-90, respectively, were observed as well as narrow PSD, positioned exactly at the borderline between the micro- and mesopores range (2.5 nm, Fig. 29b) as further confirmed by TEM imaging. Higher SSA of NPC-90 as compared to NPC-158 was attributed to the larger volume fraction of PAN.

An interesting approach to synthesizing OMC from acrylonitrile telomers (ANT), with DP = 2–10, synthesized 3-mercaptopropionic acid as CTA was demonstrated (Fig. 30) [246]. At such low MW the ANT remained liquid and could be used to infiltrate the SBA-15 silica directly or in acetone solution. Upon stabilization and pyrolysis at

600–1400 °C a mesoporous carbon was obtained. SSA was shown to increase with the addition of acetone to the initial solution used to infiltrate the templates and reached $S_{\text{BET}} = 1011 \text{ m}^2/\text{g}$. The resulting carbon was shown to be doped with nitrogen (up to 10.8%) and sulfur (<1% originating from the CTA) and was used as a catalyst for Pt in methanol oxidation reaction.

In a unique combination of hard and soft templating, PEO-*b*-PAN BCPs were utilized as a supramolecular template to synthesize mesoporous silica from TEOS. The amphiphilic BCP acted as a porogenic surfactant, which decomposed upon calcination in

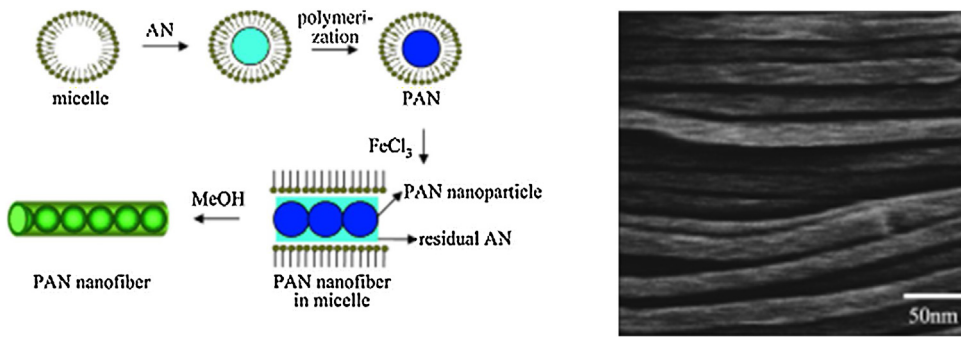


Fig. 25. Left: The overall fabrication scheme for PAN nanofibers by using a salt-assisted microemulsion polymerization. Right: (a) SEM image of carbon nanofibers obtained by heating the PAN nanofibers at a heating ratio of 1 °C/min to 300 °C then continuously 3 °C/min to 900 °C, and holding it at that temperature for 4 h under an N₂ atmosphere. [231]. Copyright 2004. Reproduced with permission from John Wiley and Sons.

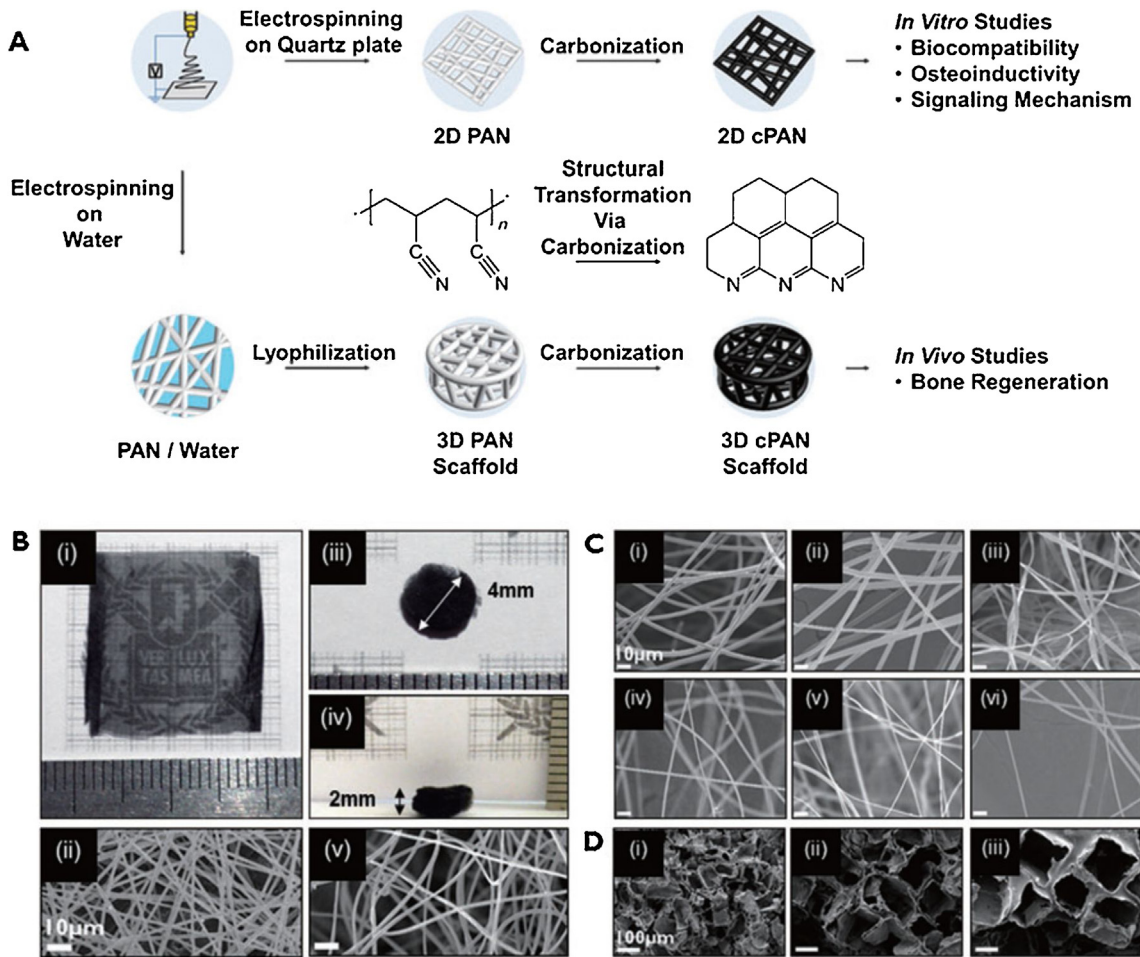


Fig. 26. Preparation and characterization of carbonized PAN (cPAN) scaffolds. (A) Illustration of the fabrication process of cPAN scaffolds. (B) (i) Digital photographs of 2D cPAN mats, (ii) SEM images of 2D cPAN mats, (iii), (iv) digital photographs of 3D cPAN scaffolds from (iii) top view and (iv) side view, v) SEM images of 3D cPAN scaffolds. C) SEM images of pore size-controlled 3D cPAN scaffolds produced by varying the weight percentage of PAN in water. [236]. Copyright 2004. Reproduced with permission from John Wiley and Sons.

air creating cylindrical pores due to self-assembly into rod-like micelles (Fig. 31). The as-obtained silica had a SSA of 600 m²/g. However, when the composite was stabilized in air and pyrolyzed in nitrogen at 800 °C, a mesoporous carbon with cylindrical morphology reflecting the cores of self-assembled micelles was formed after removal of the silica with 3 M NaOH. Nanostructured carbons with surface areas up to 900 m²/g were prepared [247]. Similarly, Wiesner et al. reported the preparation of carbon-TiO₂ composites from PEO-*b*-PAN diblock or triblock copolymers with TiO₂ precur-

sors selectively incorporated in the PEO phase by a sol-gel method. Upon stabilization and pyrolysis under nitrogen at 700 °C, hybrid composites were obtained which, after further thermal treatment under air at 450 °C produced mesoporous TiO₂ [248,249].

A novel method to template NDCs from aqueous solution of PAN has been recently introduced (Scheme 9) [250]. Interestingly, ZnCl₂ was used as both solvent and activating agent to prepare NDCs from PAN, whereas colloidal silica, cellulose nanocrystals or commercial filter paper were used as templates. 60 wt% aqueous solution

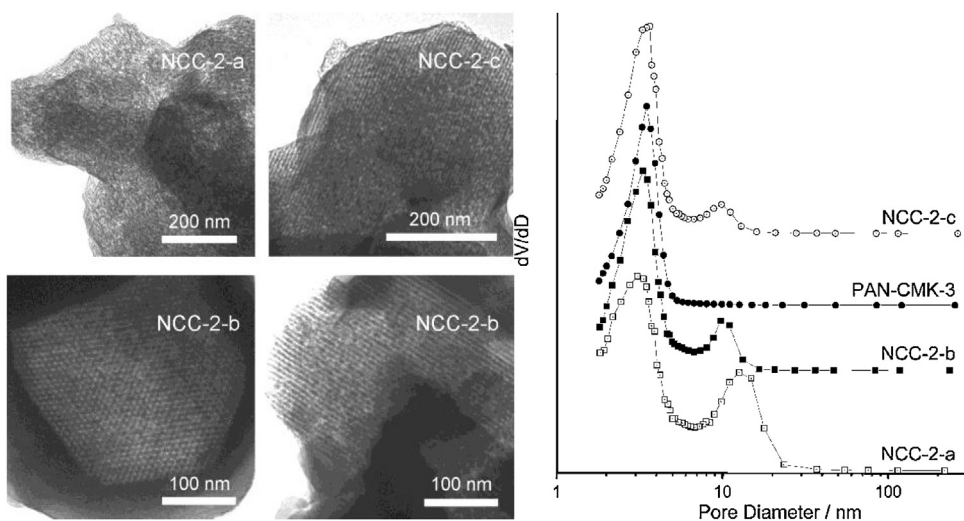


Fig. 27. TEM images of NCC-2-a (stabilized at 200 °C/carbonized at 850 °C), NCC-2-b (230 °C/850 °C), and NCC-2-c (250 °C/1100 °C). Pore size distributions of NCC-2 samples and PAN-based CMK-3. Maxima NCC-2-a: 3.0 and 12.4 nm. NCC-2-b: 3.3 and 9.8 nm. PAN-CMK-3: 3.5 nm. NCC-2-c: 3.5 and 9.9 nm. NCC stands for nanocasted carbon. PAN-CMK is a sample stabilized at 250 °C and carbonized at 850 °C. [243], Copyright 2004. Reproduced with permission from American Chemical Society.

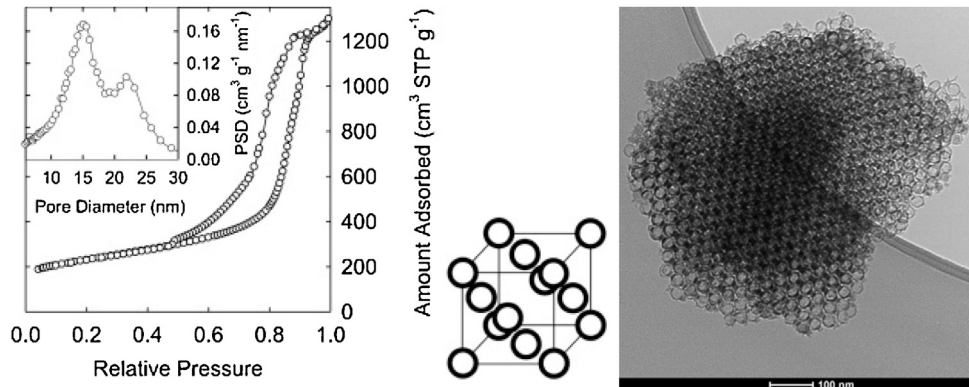


Fig. 28. Nitrogen adsorption isotherm and the pore size distribution of the ordered array of hollow carbon nanospheres (the scheme of the carbon is shown in the center). TEM image of the ordered array of hollow carbon nanospheres. [201], Copyright 2015. Reproduced with permission from Elsevier.

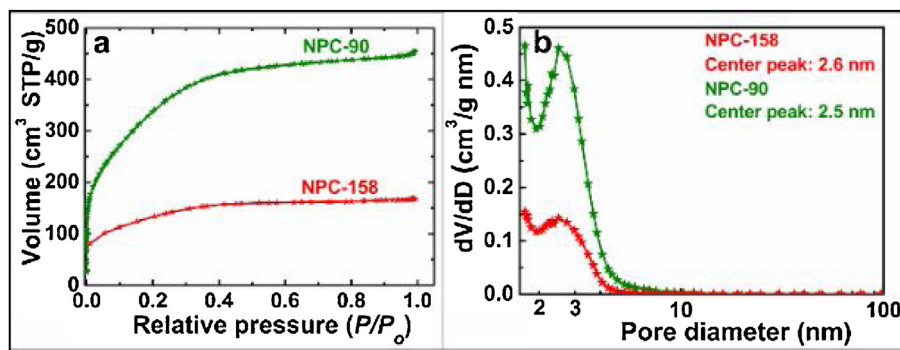
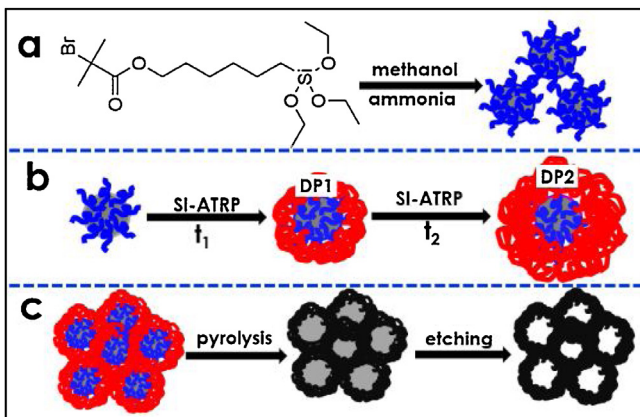


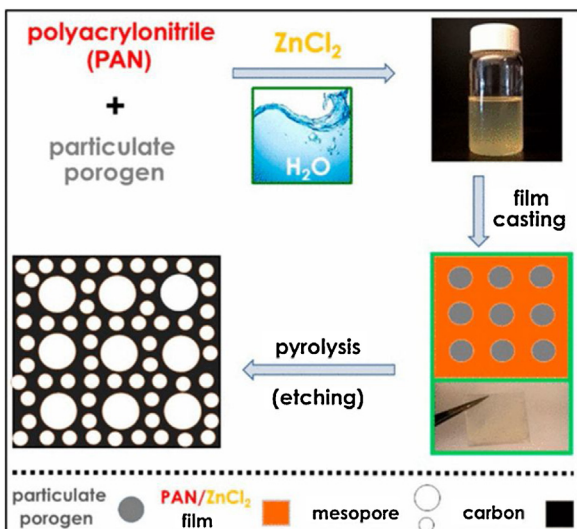
Fig. 29. (a) N₂ adsorption and desorption isotherms and (b) pore size distributions of NPC-158 and NPC-90 prepared from silica-g-PAN with different DPs. [245], Copyright 2018. Reproduced with permission from American Chemical Society.

of ZnCl₂ simultaneously dispersed commercial colloidal silica (~ 10 nm) and dissolved low MW PAN (DP 50). The dispersion was then freeze-dried and carbonized according to the standard procedures to yield NDC with S_{BET} approaching 1800 m²/g. The SSA of the resulting carbons obtained after removing the template with HF was dependent on the silica/PAN ratio and consisted predominantly (80–90%) of mesopores. Two distinct maxima observed in PSD were assigned to activation by ZnCl₂ (~ 2.5 nm) and templating

by silica NPs (10–12 nm). Furthermore, this approach was extended to all-organic templates that can be easily removed during carbonization and do not require HF etching. Mesoporous carbons with S_{BET} of 1366 and 1501 m²/g were obtained when cellulose nanocrystals or filter paper were used as templates, respectively (Fig. 32). Obtained carbons were shown to act as efficient ORR electrocatalysts.



Scheme 8. Preparation of nanoporous carbons from organosilica-g-PAN hybrids by SI-ATRP. [245]. Copyright 2018. Reproduced with permission from American Chemical Society.



Scheme 9. Synthetic route to NDCs templated from aqueous $ZnCl_2$ /PAN solution. [250]. Copyright 2017. Reproduced with permission from American Chemical Society.

3.4.2. Soft templating: copolymer-templated nanocarbons (CTNC)

Despite excellent control over the pore size and surface area, a major disadvantage of hard templating lies in removal of the template, usually performed under harsh conditions, such as washing with quite concentrated solutions of NaOH or HF. Instead of using a template with a predefined shape, soft-templating is based on self-assembly of a biphasic (or multiphasic) system, in which one phase (or more phases) will ultimately serve as a porogen and another one as a carbon source. In the simplest case, a single block copolymer constitutes both the porogen and the carbon source in the form of the phase-separated domains. In many other cases, two or more components are involved, such as a surfactant whose micelles serve as a porogen, and a carbon source, being for instance a cross-linked polymer, which can be carbonized with prior or concomitant surfactant removal. Herein, the focus will be on carbons derived from phase-separated block copolymers, while the surfactant-templated carbons were extensively discussed elsewhere [50–52].

Copolymer-templated nanocarbons (CTNC) were obtained by bulk carbonization of PBA-*b*-PAN BCPs introduced in the previous section (**Scheme 10**) [251–253]. It was anticipated that decomposition of the PBA block in self-assembled bulk powders would create significant porosity. Indeed, the crucial feature of CTNCs

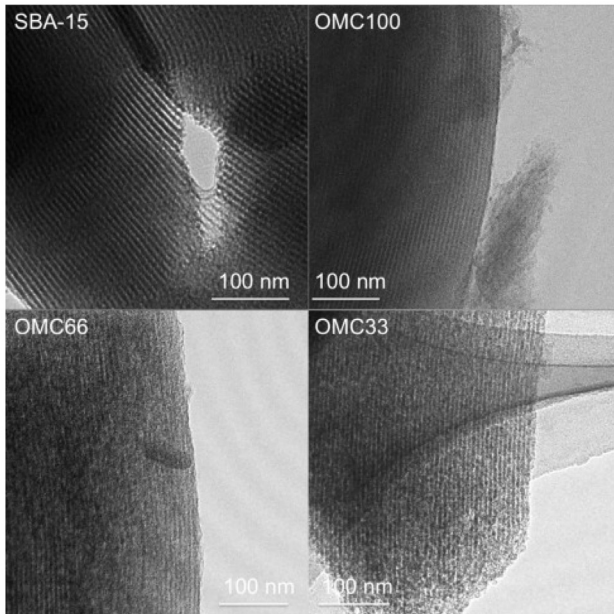
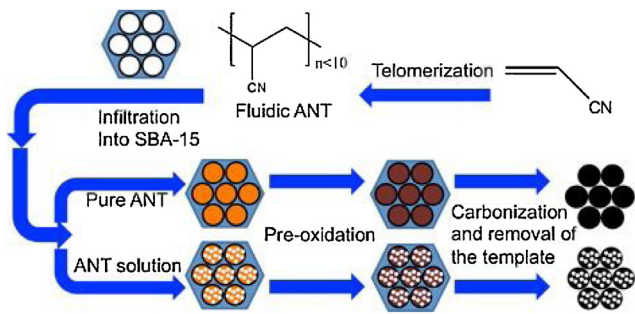
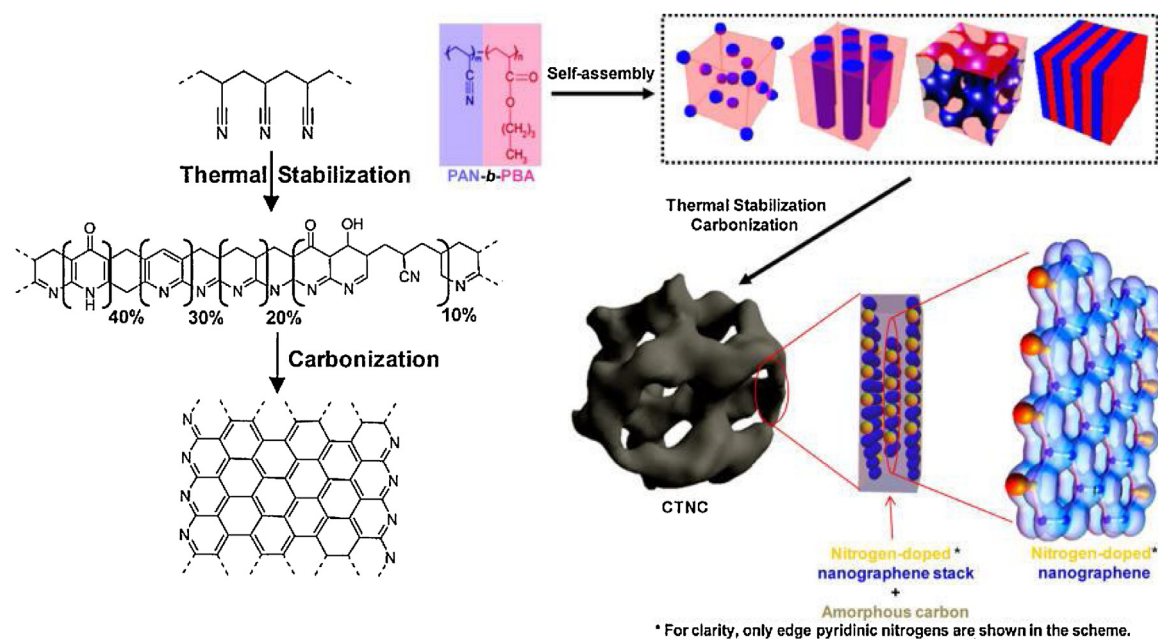


Fig. 30. Schematic illustration of the synthesis of ordered mesoporous carbons (OMCs) by using acrylonitrile telomers (ANT) as the precursor. TEM images of SBA-15, OMC100, OMC66 and OMC33 respectively. The numbers denote the concentration of ANT in the solution used to penetrate SBA-15. [246]. Copyright 2015. Reproduced with permission from Elsevier.

is manifested in the dependence of SSA on the morphology of the precursor copolymer was already demonstrated for thin films (see Section 3.1). The self-assembly and carbonization of PBA-*b*-PAN BCPs was then studied by varying their compositions, i.e. PAN/PBA weight ratio [251]. However, collapse of the carbon structure was evidenced for BCPs with spherical, cylindrical and lamellar morphologies subjected to bulk pyrolysis without the solid support. Only BCPs with a bicontinuous (e.g., gyroidal) morphology, achieved at compositions corresponding to 40 wt% of PAN, resulted in self-supported nanocarbons with good retention of the phase-separated morphology, and thus high SSA ($500 \text{ m}^2/\text{g}$) originating from the removal of the PBA block.

Evolution of the morphology at each step of thermal processing of the $(\text{BA})_{70}-b-(\text{AN})_{99}$ BCP (37 wt % of PAN) to CTNC was followed by small angle x-ray scattering (SAXS, **Fig. 33a**). The as-prepared, precipitated powder did not exhibit any features in its scattering pattern, however upon thermal annealing at $100\text{--}200^\circ\text{C}$ under vacuum, a clear Bragg peak could be observed at $q = 0.27 \text{ nm}^{-1}$, corresponding to the average d-spacing between the PBA and PAN domains of 23 nm. Further thermal stabilization and carbonization yielded a bulk carbon powder with an identical position of the Bragg peak in the scattering pattern (**Fig. 33b**), confirming the successful preservation of the self-assembled, bicontinuous morphology. BJH analysis of the N_2 adsorption isotherm determined the average pore



Scheme 10. Preparation of copolymer templated nanocarbons (CTNCs). [253], Copyright 2012. Reproduced with permission from American Chemical Society.

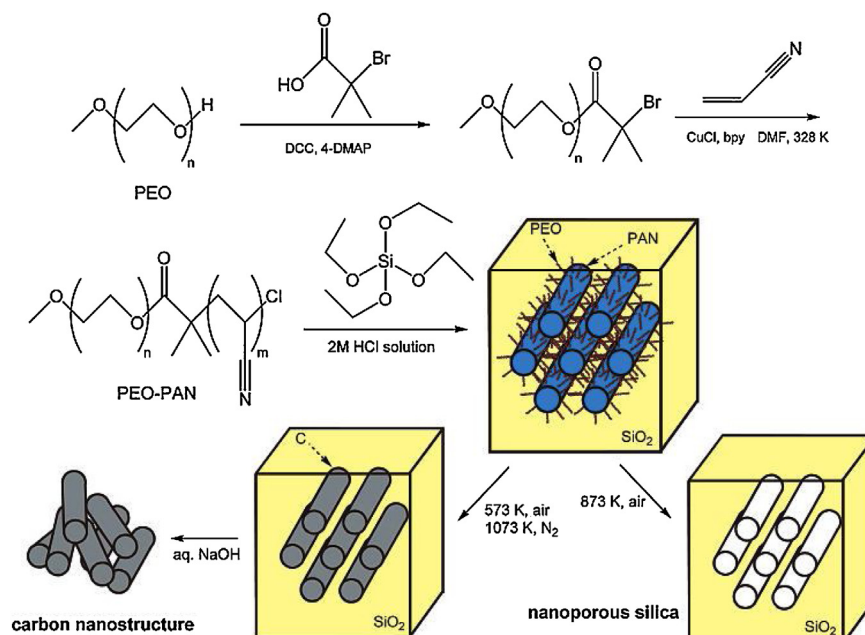


Fig. 31. Synthesis of nanostructured silica/carbon composites, nanoporous silicas, and carbons on the basis of the supramolecular templating of silicas with PEO-*b*-PAN copolymers. [247], Copyright 2006. Reproduced with permission from American Chemical Society.

size in the obtained CTNC to be 13 nm (Fig. 33c), suggesting 10 nm thickness of a nanocarbon wall, which corresponds to the stack of only a few or few tens of graphene layers. The strong (002) Bragg reflection at $2\theta = 25^\circ$ visible in the XRD spectrum of the synthesized CTNC (Fig. 33d), allowed the thickness of a graphitic domain to be estimated to be two-three layers and the lateral size of graphitic domains to 2–3 nm (calculated from the (001) peak at $2\theta = 44^\circ$). However, the mesoporous SA (S_{meso}) accounts only for ca. 50% of the total S_{BET} , whereas the other 50% can be ascribed to micropores (< 2 nm), confirmed by the sharp increase of the adsorption isotherm at very low relative pressures characteristic for micropores. This suggests that the carbon network is inherently microporous and CTNCs have hierarchical structure of micro and mesopores.

Furthermore, PSD in CTNCs can be finely tuned by adjusting overall MW of the precursor BCP while maintaining constant composition. That was confirmed by investigating the carbonization of a series of BCPs with similar composition, (40 wt% PAN) [141]. Mesopores of controlled size between ca. 5–22 nm were achieved by increasing the DP of PAN macroinitiator from 56 to 184 (Fig. 34). However, one limitation of the soft-templated approach arises from the weaker segregation at lower MWs. This was studied by comparing detailed analyses of the same series of BCP precursors and resulting carbons using SAXS, TEM and BET. As expected, an increase in SSA with decreasing the pore size was not observed and S_{BET} values remained <500 m²/g. This was due to the loss of pore connectivity in CTNCs prepared from low MW precursors.

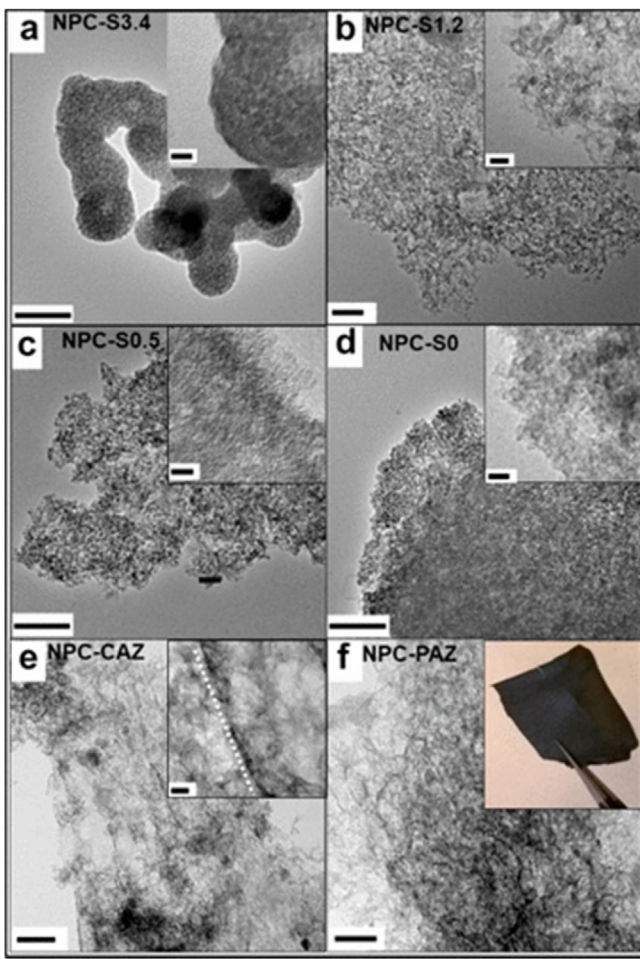


Fig. 32. Representative TEM images of porous carbon prepared at SiO_2/PAN ratios of (a) 3.4, (b) 1.2, (c) 0.5, and (d) without the addition of colloidal SiO_2 NPs, templated from cellulose nanocrystals (e) and filter paper (f) after infiltration with PAN/ZnCl_2 solution. Inset in panel f shows a digital picture of the corresponding free-standing carbon film. Scale bars are 200 nm in main figures and 20 nm in insets. [250], Copyright 2017. Reproduced with permission from American Chemical Society.

Crosslinking of PBA/PAN BCPs during the oxidative stabilization step is responsible for morphology preservation but low MW BCPs can also reach their order-disorder transition (ODT) temperature, disrupting the self-assembled structure. Additionally, as demonstrated using differential scanning calorimetry (DSC), PAN cyclization and PBA decomposition are well-separated when conducted under nitrogen but under air both processes are exothermic and occur at similar temperatures (Fig. 35). Therefore, decomposition of the PBA block before the PAN has fully cross-linked can also lead to the collapse of morphology during carbonization. Thus, slow oxidation at a low temperature ($<300^\circ\text{C}$) should be employed in order to develop the morphology and provide sufficient crosslinking of the PAN phase [141].

Recent studies showed that sulfur can be used instead of oxygen as an effective PAN stabilizing agent, leading to preserved morphology without any collapse upon further pyrolysis [254]. Under the same thermal conditions, sulfur-stabilized nanocarbons show similar SSA and PSD compared to oxygen-stabilized CTNCs. Additionally, sulfur dopants were introduced into the carbon framework without any loss in the total nitrogen content resulting in a N/S co-doped carbon material. The prepared co-doped nanocarbons showed excellent control over porosity by tuning the respective block lengths of the PAN-*b*-PBA precursors, similarly to monodoped CTNC.

One approach to overcome the abovementioned issues could be using different sacrificial block, more incompatible with PAN than PBA, e.g. PMMA. (AN)₄₅₀-*b*-(MMA)₈₉ BCPs, containing 75 wt% PAN were synthesized [191]. With PMMA as the minority phase, cylindrical morphology with hexagonally-packed PMMA cylinders was observed. Upon stabilization and carbonization at 800°C , the nanostructured carbon with high SSA of $860 \text{ m}^2/\text{g}$ and average mesopore size $\tilde{s} 3 \text{ nm}$ were prepared, Fig. 36. However, one disadvantage of PMMA might be its ceiling temperature ($200\text{--}325^\circ\text{C}$) [255], similar to the cyclization temperature of PAN ($200\text{--}300^\circ\text{C}$) [256], which may lead to collapse of the nanocarbon and lower surface areas. Indeed, other reports on mesoporous carbons derived from PAN-*b*-PMMA BCPs showed significantly lower SSAs [192,193].

An interesting approach to CTNC/NPs hybrids by additive-driven self-assembly was demonstrated [189]. Namely, a PtBA-*b*-PAN copolymer (composition $(t\text{-BA})_{112}\text{-}b\text{-}(AN)_{416}$, 60 wt % PAN) was synthesized and mixed with iron (III) oxide NPs ($\phi = 2.7 \pm 0.9 \text{ nm}$) previously modified with hydroxyphenyl groups in DMF. Due to specific hydrogen bonding with nitrile groups, the NPs selectively collected in the PAN phase. As shown by SAXS, a strong Bragg peak was observed in the BCPs annealed with the addition of NPs, suggesting that formation self-assembled morphology was facilitated by their interaction with PAN. Upon increasing the NP loading from 10 to 20 wt%, the narrowing of the Bragg peak indicated more efficient segregation, and shifting to higher q was attributed to decreased d-spacing (Fig. 37). Upon stabilization and carbonization at 800°C , mesoporous carbon/iron oxide nanocomposites were fabricated, with SSA increasing with the Fe_2O_3 content in the precursor, up to $757 \text{ m}^2/\text{g}$. Furthermore, TEM characterization confirmed that Fe_2O_3 NPs remained embedded in the obtained carbon after pyrolysis (Fig. 38).

Very recently another approach to partially overcome the weak segregation issue was proposed. Molecular bottlebrushes with PBA-*b*-PAN side arms instead of diblock copolymers were employed as carbon precursors [257]. In such a system mesoporosity originates from a specific brush topology rather than from self-assembly between the PBA and PAN blocks. However, even though the composition of the BCP-based side arms do not determine the morphology, the DP of the outer PAN block was found to be critical in order to provide sufficient intermolecular cross-linking between the brushes and prevent morphology collapse. Nanocarbons with small mesopores $<10 \text{ nm}$ and S_{BET} up to $420 \text{ m}^2/\text{g}$ were obtained from such bottlebrushes and used as ORR electrocatalysts.

4. Applications of PAN-Derived nitrogen-enriched nanocarbons

4.1. Supercapacitors

Supercapacitors, also termed electrical double layer capacitors (EDLC), can store 10–100 times more energy than conventional capacitors as well as provide a much faster rate of charge/discharge than batteries [258]. Since supercapacitors store electrical charge at the interface between the electrode and electrolyte, high SSA and porosity are critical to achieve optimal capacitance. Hence, porous carbons are the materials most widely used for fabrication of EDLCs and typically achieve surface specific capacitance (C_s), defined as specific capacitance (C_g) divided by S_{BET} , between $5\text{--}25 \mu\text{F}/\text{cm}^2$ [252].

Another method to increase capacitance is to incorporate a redox center that is able to participate in reversible Faradaic processes, thus introducing pseudocapacitance. In carbon materials, this can be realized by doping the graphitic network with heteroatoms, such as nitrogen [259]. PAN is a particularly attrac-

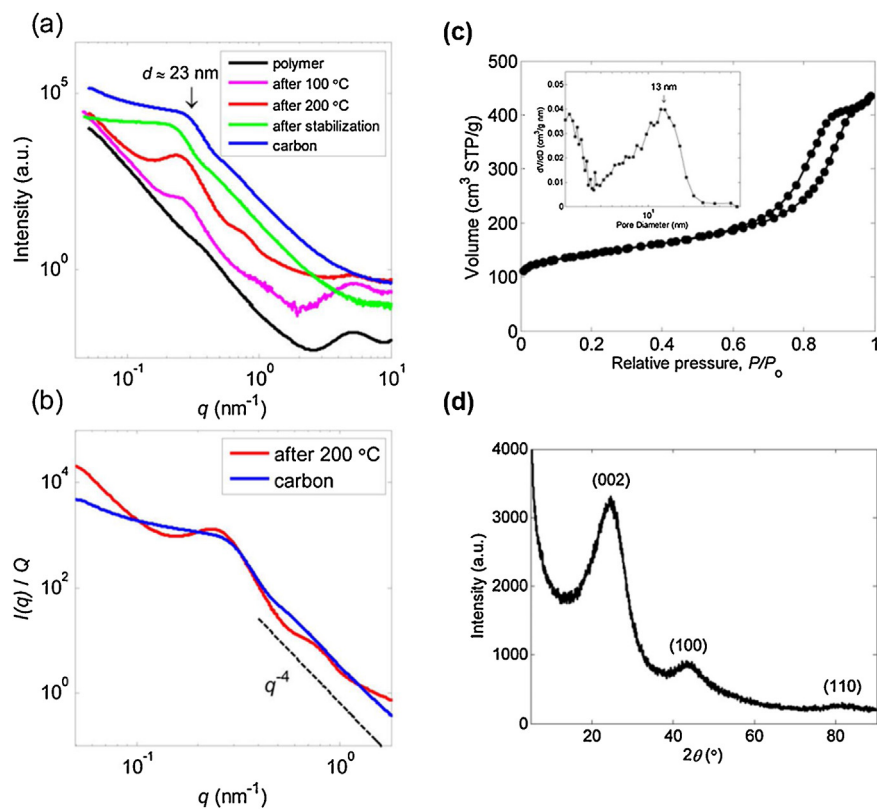


Fig. 33. Structural characterization of CTNC (a) SAXS profiles of a precursor BCP and resulting carbon at various stages of thermal treatment; (b) comparison $(AN)_{99-b-(BA)}_{70}$ annealed at 200 °C (dotted) and its corresponding CTNC pyrolyzed at 700 °C (solid); (c) N_2 adsorption isotherm and pore size distribution (inset); (d) XRD spectrum with distinct (002) and (100) Bragg reflections. [253], Copyright 2012. Reproduced with permission from American Chemical Society.

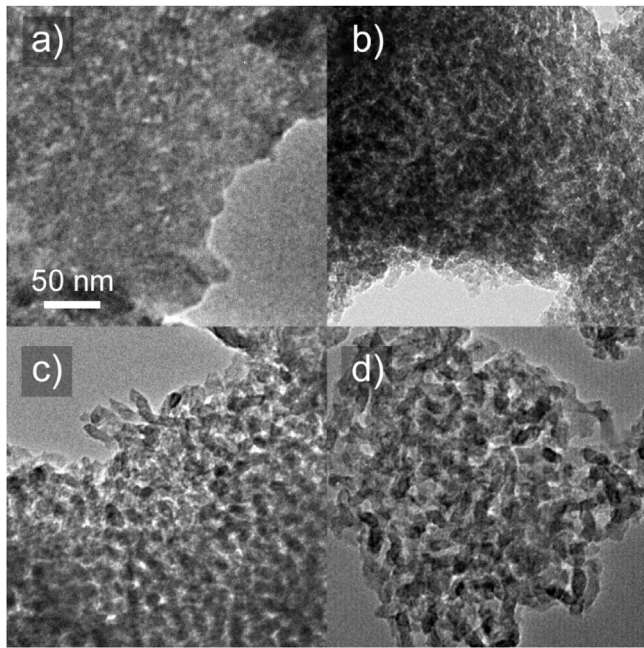


Fig. 34. TEM images of CTNCs prepared by pyrolysis of (a) $(AN)_{70-b-(BA)}_{40}$, (b) $(AN)_{86-b-(BA)}_{54}$, (c) $(AN)_{122-b-(BA)}_{79}$, and (d) $(AN)_{184-b-(BA)}_{124}$. [141], Copyright 2017. Reproduced with permission from American Chemical Society.

tive precursor to NDC due to its high nitrogen content (26.4 wt %) and the well-known carbonization mechanism. For traditional commercial carbon fiber applications, the nitrogen atoms are not desirable, as they act as defects in graphitic basal planes leading

to poorer mechanical properties and they need to be removed by high-temperature (1000–2000 °C) graphitization. Under lower T_p (500–800 °C), graphitic domains do not entirely fuse, resulting in accessible edge-site pyridinic nitrogen atoms [260]. Thus, increasing the T_p attributes the obtained carbon with lower N content but higher conductivity.

The effect of nitrogen functionalities in microporous activated carbons prepared from PAN and its blends with poly(4-vinylpyridine) and coal-tar pitch was investigated [38,39]. A perfect correlation between the N content and increased capacitance was observed in the presence of an acidic electrolyte, 1 M H_2SO_4 , for carbons with comparable SSAs (ca. 750–900 m^2/g) and C_g values up to 176 F/g at 0.1 A/g. N-dopants acted as Faradaic redox sites as well as increased polarity of the carbon surface, making it more accessible to the electrolyte. Specifically, N atoms located on the graphitic edges, namely pyridinic, pyridonic and pyridine oxide were discussed as providing the main contribution to the overall capacitance. Similar capacitance ($C_g = 140$ F/g, $C_s = 25 \mu F/cm^2$) was observed in 6 M KOH electrolyte for $ZnCl_2$ -activated, electrospun PAN-derived nanofibers [230].

Mesoporous NDC were prepared by pyrolysis of PAN/silica-gel composites (NPC-PAN) followed by HF etching, and investigated the influence of T_p on the performance of supercapacitors fabricated with obtained carbons [261]. The S_{BET} of the synthesized carbon was found to greatly depend on T_p , ranging from 268 to 635 m^2/g as the temperature increased from 500 to 800 °C, respectively and was attributed to higher pyrolysis yields at higher temperatures leading to larger silica/pore content. Cyclic voltammetry (CV, Fig. 39a) curves showed near-ideal, rectangular shape for the samples pyrolyzed at 700–900 °C indicating fast reorganization of the electrical double layer at potential switching. On the other hand, NPC-PAN500 and NPC-PAN-600 exhibited lower

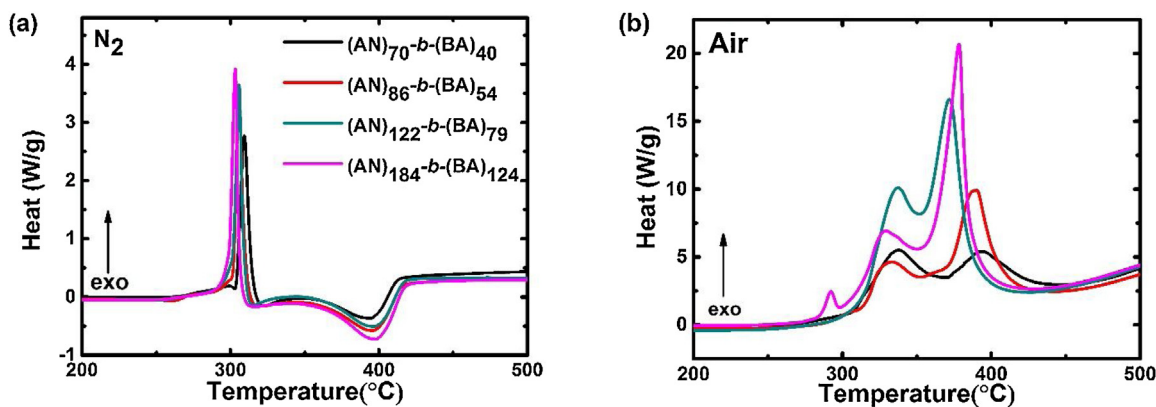


Fig. 35. DSC thermograms of PAN-*b*-PBA BCPs with different MWs and similar composition recorded under (a) nitrogen and (b) air. [141], Copyright 2017. Reproduced with permission from American Chemical Society.

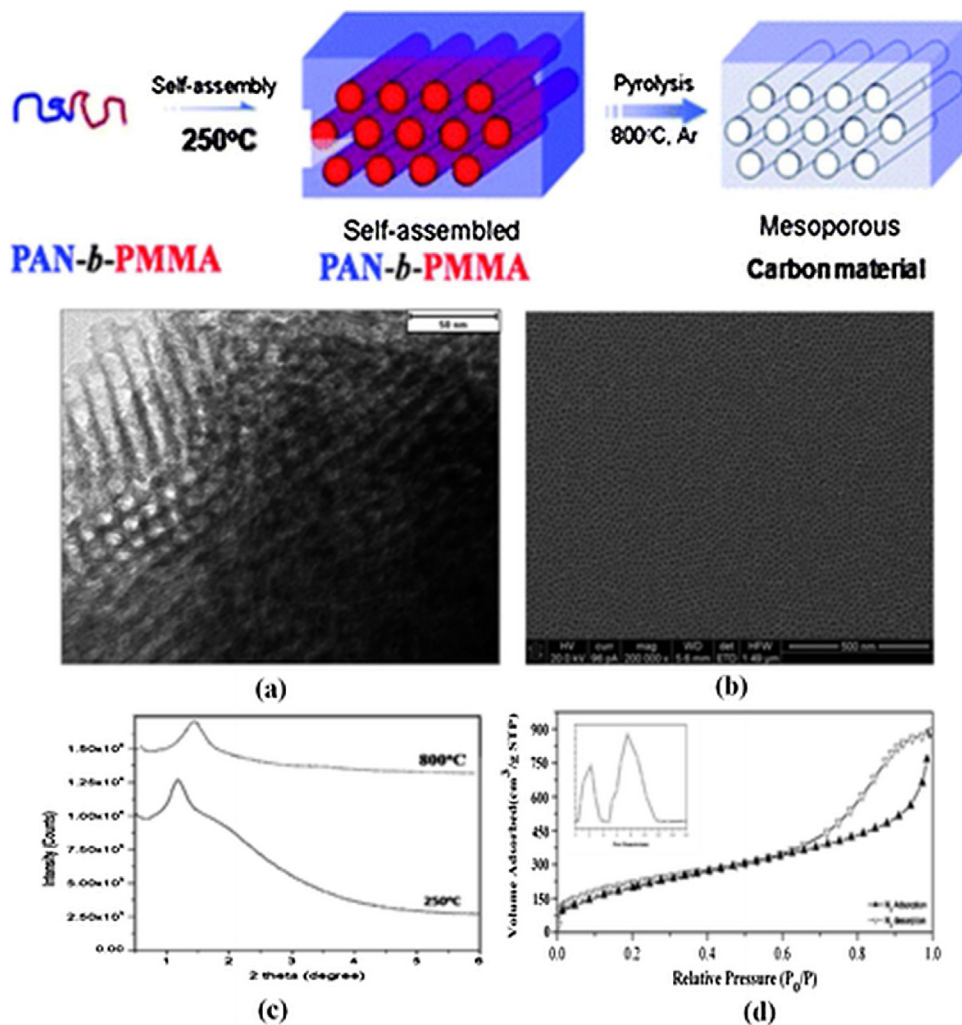


Fig. 36. Microphase separation of PAN-*b*-PMMA diblock copolymer and characterization of mesoporous carbon materials from $(AN)_{450}-b-(MMA)_{89}$ diblock copolymer by pyrolyzed at 800 °C under Ar atmosphere; (a) TEM image; scale bar is 50 nm, (b) SEM image; scale bar is 500 nm, (c) small-angle XRD pattern, and (d) N_2 adsorption–desorption isotherm and pore size distribution (inset). [191], Copyright 2011. Reproduced with permission from Royal Society of Chemistry.

capacity caused by their lower S_{BET} and conductivity. Galvanostatic discharge curves were then recorded to demonstrate that NPC-PAN800 discharged over the longest time (Fig. 39b), and its C_s was calculated to be 33 $\mu\text{F}/\text{cm}^2$, as compared to 26 $\mu\text{F}/\text{cm}^2$ for NPC-PAN900. Since both NPC-PAN800 and 900 had similar S_{BET} (635 and 608 m^2/g , respectively), the better performance resulted from

its higher N-content. Similar to previous reports, edge-site pyridinic and pyrrolic N atoms were shown to be mainly responsible for the pseudocapacitance effect.

Porous structure of CTNCs, soft-templated from bicontinuous PBA-*b*-PAN BCPs makes them promising materials for application as EDLC. Detailed analysis of composition and N dopants of a CTNC

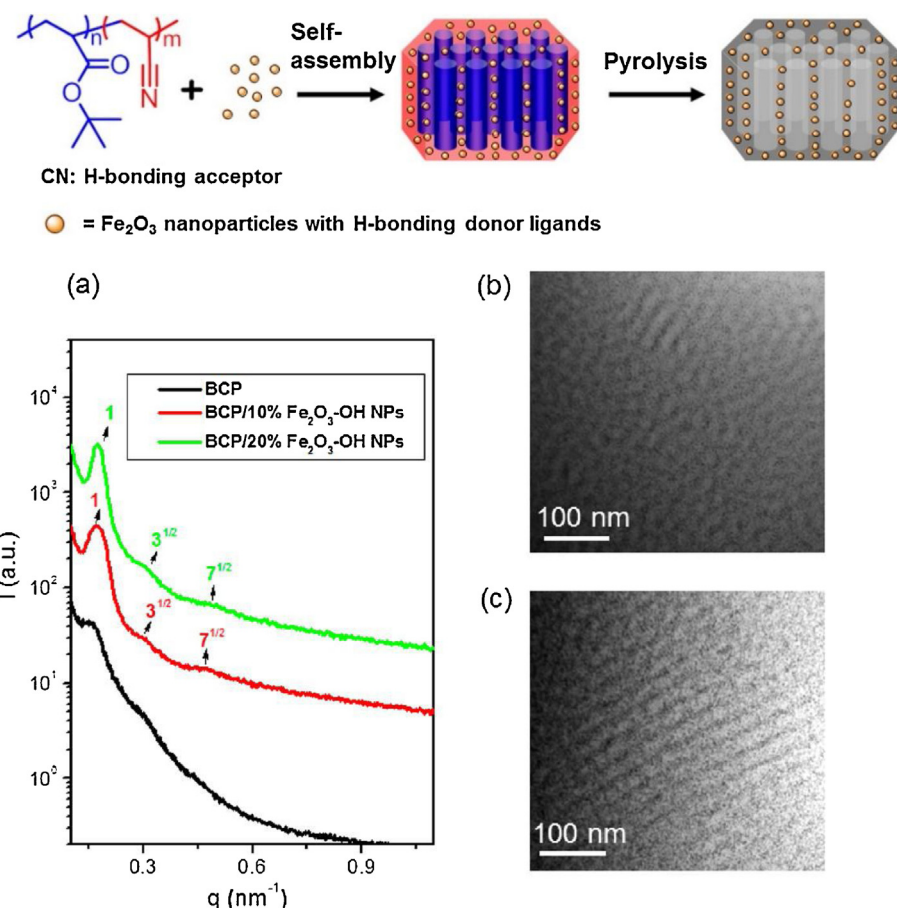


Fig. 37. Top: Schematic of the preparation of mesoporous carbon/iron oxide nanocomposites using additive-driven self-assembly. Bottom: (a) Overlay of SAXS profiles of the PtBA-*b*-PAN block copolymer and its blends with Fe_2O_3 -OH NPs before carbonization. TEM images of the blend of the BCP with (b) 10 wt % Fe_2O_3 -OH NPs and (c) 20 wt % Fe_2O_3 -OH NPs before carbonization. All of the samples are annealed at 150 °C for 2 days. [189]. Copyright 2014. Reproduced with permission from American Chemical Society.

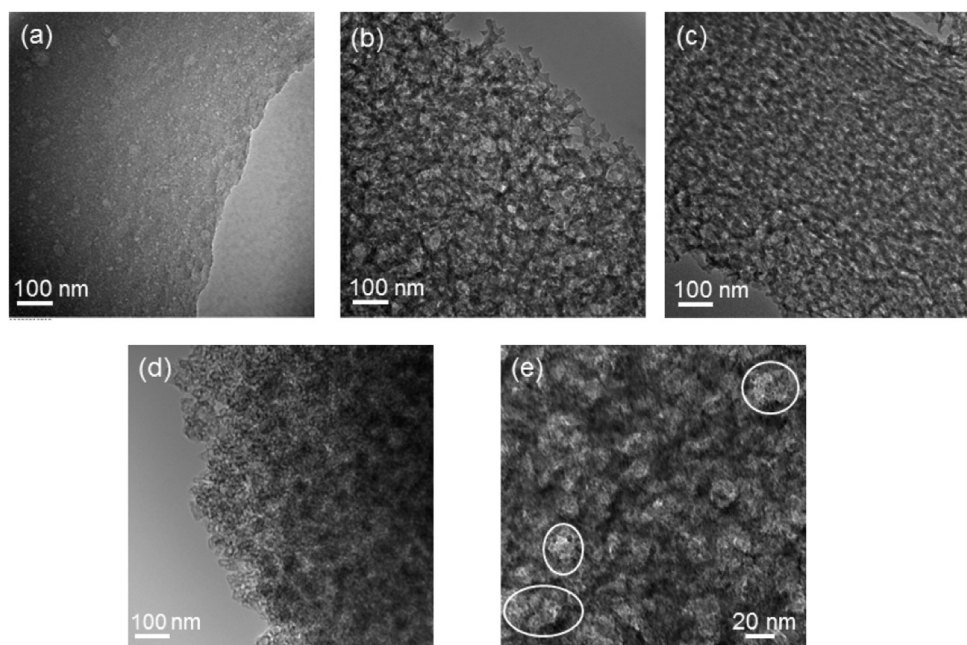


Fig. 38. TEM images of various PAN-based materials after carbonization (a) PAN homopolymer, (b) PtBA-*b*-PAN BCP, (c) BCP/10% Fe_2O_3 -OH NPs, and (d, e) BCP/20% Fe_2O_3 -OH NPs, the highlighted circles in panel e shows that the individual NPs remain intact after carbonization. [189]. Copyright 2014. Reproduced with permission from American Chemical Society.

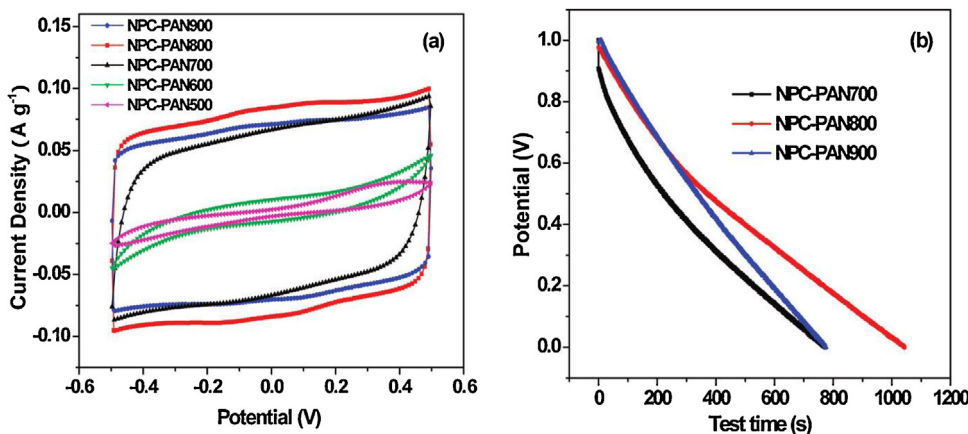


Fig. 39. (a) CV curves of the NPC-PANx samples at the scan rate of 1 mV/s and (b) their discharge curves at the current load of 0.1 A/g. [261], Copyright 2010. Reproduced with permission from American Chemical Society.

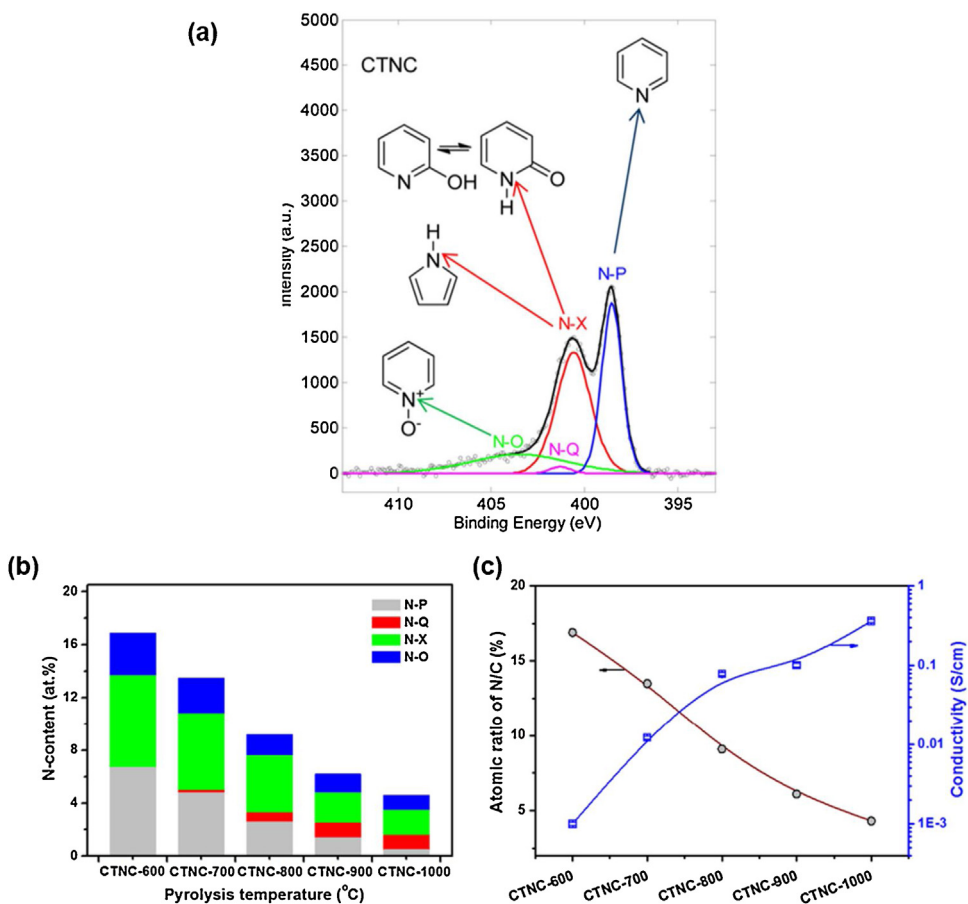


Fig. 40. Nitrogen doping in CTNCs: (a) High resolution N 1s peaks in XPS of CTNC corresponding to different types of doped N atoms. (b) Nitrogen-bonding distributions in carbon framework. N-P; pyridinic N, N-Q; quaternary N, N-X; pyrrolic N (or pyridonic N); N-O; pyridinic N-oxide. (c) Atomic ratio of N/C in carbon framework and their conductivity as a function of T_p . [253], [262]. Copyright 2012. Reproduced with permission from American Chemical Society and Royal Society of Chemistry.

sample prepared at 700 °C was performed by high-resolution XPS (Fig. 40a). Deconvolution of the N 1s band allowed determination of the abundance of every nitrogen species and revealed the presence of 35% pyridinic (N-P, 398.5 eV), 43% pyridonic + pyrrolic (N-X, 400.6 eV), 20% pyridine oxide (N-O, 403.5 eV) and 2% of quarternary (N-Q, 401.3 eV), thereby indicating that as much as 78% of all nitrogen dopants were edge-site functionalities. Further detailed investigation revealed that increasing T_p from 600 to 1000 °C resulted in a familiar trend of decreasing the nitrogen

content (from ca. 18 to 4 at. %) and drastically improved conductivity. In addition, a higher fraction of N-Q and lower concentration of edge-site N atoms was recorded for samples pyrolyzed at the highest temperatures, as expected due to fusing of graphitic planes (Fig. 40b and c) [253,262].

Excellent performance of CTNCs in supercapacitor devices was confirmed by recording CV and galvanostatic charge/discharge curves in 1 M H₂SO₄ and the results displayed nearly rectangular and triangular shapes (Fig. 41a and b). C_g was found to be

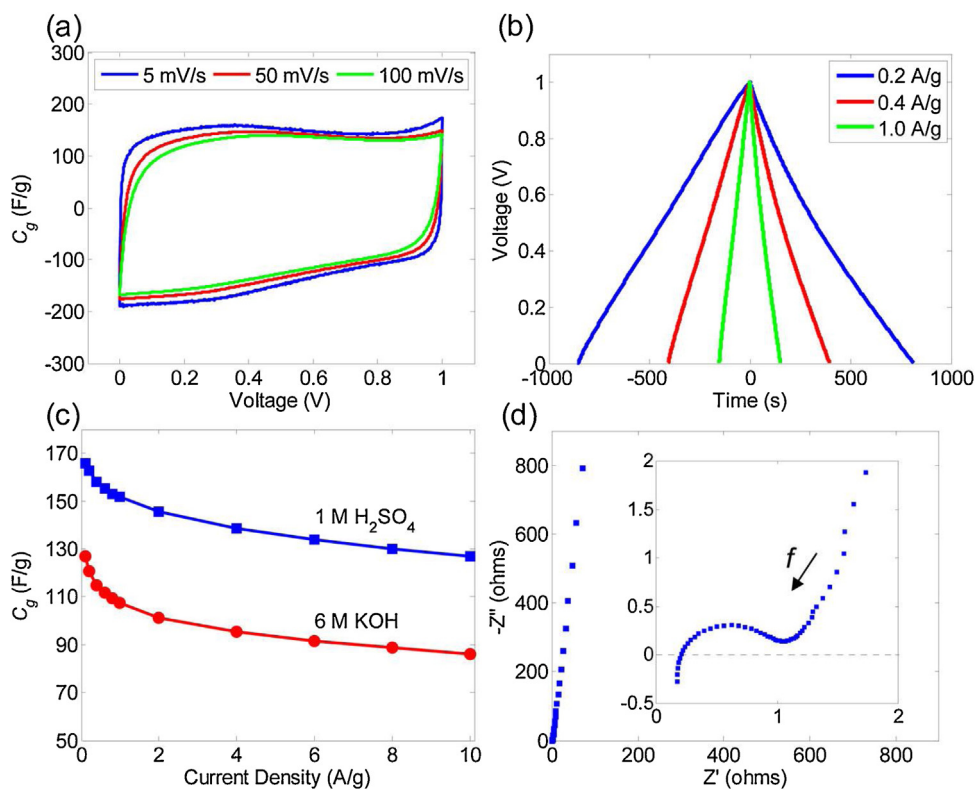


Fig. 41. Characterization of supercapacitors built with CTNC electrodes: (a) cyclic voltammetry curves; (b) galvanostatic charge – discharge curves; (c) relationship between C_g and current density; (d) Nyquist plot using a sinusoidal signal of 5 mV over the frequency range from 105 Hz to 10 – 3 Hz at open circuit potential. Plots a, b, and d show results obtained by using 1 M H_2SO_4 as an electrolyte. [253]. Copyright 2012. Reproduced with permission from American Chemical Society.

166 F/g at 0.1 A/g, corresponding to $C_s = 33 \mu\text{F}/\text{cm}^2$ and retained 77% (127 F/g) at 10 A/g (Fig. 41c). In addition, 85% of capacitance was maintained after 14,000 charge/discharge cycles at 2 A/g, and the electrochemical impedance spectroscopy (EIS) pointed to a relatively low contribution from the resistive component to the device impedance (Fig. 41d) [253]. Furthermore, activation of CTNC with CO_2 or KOH resulted in significantly increased SSA (1140 and 2570 m^2/g , respectively). However, the procedure did not improve the capacitance, since the N content in activated CTNC was dramatically decreased, to ca. 5 and 1 at. %, respectively. This supported the importance of pseudocapacitance contribution to the overall capacitance of N-doped-carbon-based EDLCs. Notably, nanocarbons prepared from PAN-*b*-PMMA BCPs [192,193], self-assembled Fe_2O_3 /PAN-*b*-PtBA composites [189], activated PAN/CTNC composites [263], PAN nanofibers [264–267] as well as PAN/ H_3PO_4 -derived P/N-doped carbons [268] were also used to fabricate supercapacitors.

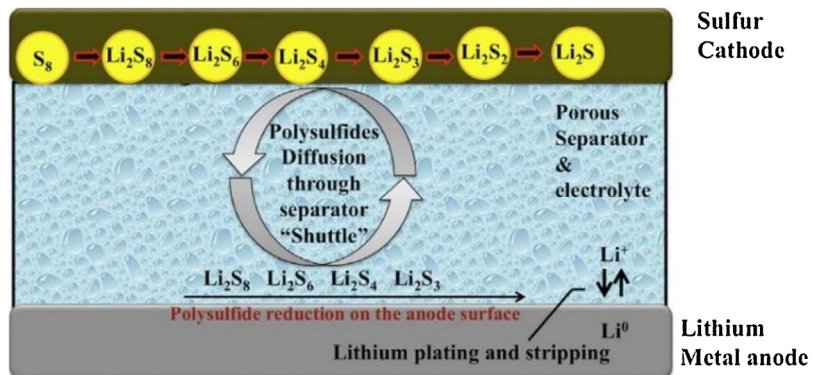
It should be emphasized that despite their moderate S_{BET} (ca. 500 m^2/g), CTNCs can produce supercapacitors with $C_s = 33 \mu\text{F}/\text{cm}^2$, typically achieved at much larger SSA values. This can be attributed to the fact that N-dopants, specifically pyridinic, are preferentially exposed on the pore walls of the CTNC during the thermal treatment. This is due to the partial crystallinity of PAN domains, which results in two types of interfaces between the PAN and PBA phases, namely covalent and non-bonded. Based on the XPS measurements discussed above, most of the N atoms in CTNC were found to occupy zigzag edges. Those N-atoms were also preferentially exposed due to removal of the non-bonded interface during the decomposition of the PBA block. Clearly, bicontinuous morphology of the precursor PBA-*b*-PAN BCP helped to expose the highest fraction of the edge N dopants. Such an exposure of N sites was postulated to be responsible for the remarkable electrochemical activity of CTNC [252,269].

Synthesis of N/S co-doped CTNC can be realized by using sulfur as a stabilizing agent. Interestingly, as sulfur is a less oxidizing than oxygen, more electrocatalytically active pyridinic nitrogen were also preserved in addition to sulfur atoms, showing improved performance in supercapacitors [254]. CTNCs containing 8.8 at. % of S and 8.2 at. % of N were synthesized with pyridinic N content of 51% were obtained and exhibited improved performance as supercapacitors in alkaline media, compared to mono-doped CTNC.

4.2. Li-S batteries

Li-ion batteries have revolutionized energy storage in recent decades. However, while Li-ion batteries are inexpensive, efficient and ubiquitous, they still suffer from many drawbacks, the most pronounced being relatively low capacity. Among multiple alternatives, rechargeable lithium-sulfur (Li-S) battery remains the most attractive candidate due to its high theoretical energy density (2600 Wh Kg^{-1}) and specific capacity (1672 mAh g^{-1}), assuming a complete reaction, $16Li + S_8 \rightleftharpoons 8Li_2S$. Additionally, the low cost of sulfur (\$0.02/g), its abundant reserves and availability provide additional motivations for developing Li-S batteries [270].

However, despite the considerable advantages of Li-S batteries, several key issues have so far hindered their practical application. First, the insulating nature of sulfur ($5 \times 10^{-30} \text{ S/cm}$ at 25°C) and sulfides greatly limits the electron transfer process and efficient utilization of active cathode materials. Therefore, conductive additives are needed to compensate for the poor conductivity. Secondly, sulfur undergoes around 80% of volume expansion after lithiation, and such a large volume change can adversely affect or even cause collapse of the whole conductive network, resulting in unstable and short-term cell performance [271]. Most importantly, a series of intermediate lithium polysulfides ($LiPS$, Li_2S_x , $3 \leq x \leq 8$) are generated during the redox reaction. These LiPS are highly sol-



Scheme 11. Illustration of polysulfides dissolution and shuttling process in a Li–S battery during the recharge process. [270], Copyright 2015. Reproduced with permission from Elsevier.

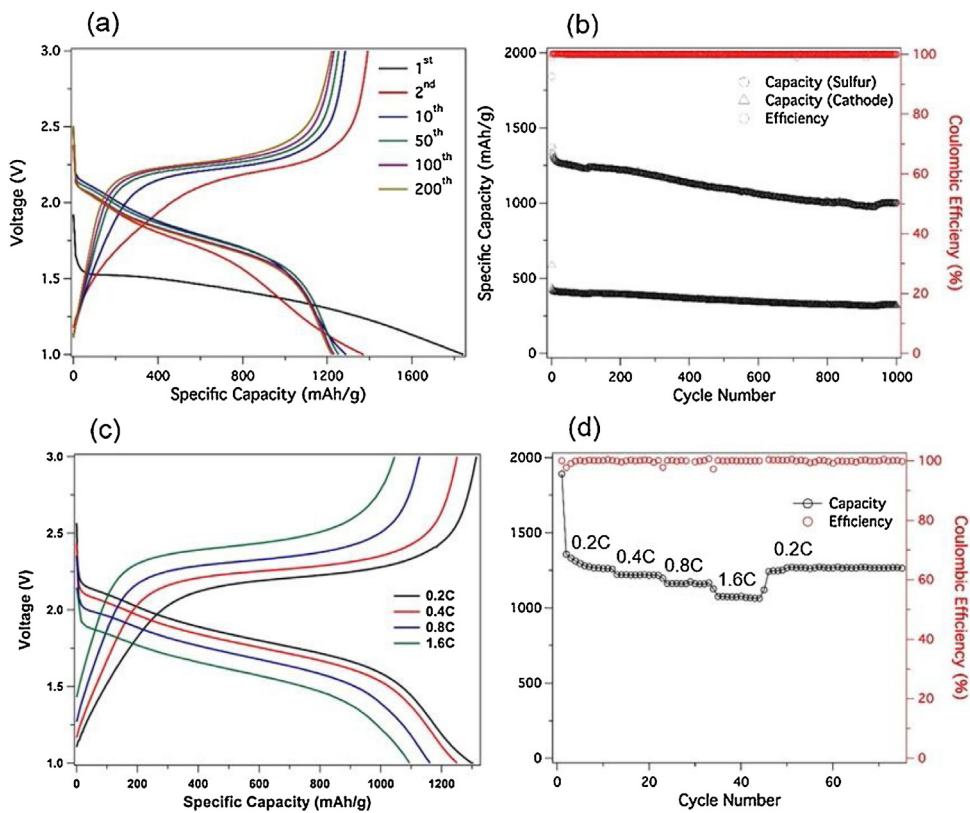


Fig. 42. (a) Electrochemical discharge and charge curves of SPAN450 at various cycles. The tests were performed at 0.4 C for both charge and discharge in the potential range of 1–3 V vs Li/Li⁺. (b) Capacity and Coulombic efficiencies versus cycle number for SPAN450. The black circles report capacities relative to the weight of the active sulfur species in the cathode, whereas the data represented by black triangles are the corresponding capacities based on the overall cathode mass. (c, d) Rate performances of the SPAN measured at various C-rates. The C-rates were same for both charge and discharge in each cycle. [278], Copyright 2015. Reproduced with permission from American Chemical Society.

uble in commonly used electrolytes and may result in increased viscosity and decreased ionic conductivity of the electrolyte. Moreover, dissolved LiPS continuously shuttle between the cathode and anode during the charge/discharge process, depleting the sulfur, consuming the electric energy, and reducing the battery capacity. **Scheme 11** illustrates the LiPS shuttle phenomena in the recharge process. All of these abovementioned effects do not allow to reach the theoretical capacity, with the best performing Li–S cells rarely exceeding 60% of the theoretical value [270].

To overcome these shortcomings and achieve better performing Li–S batteries, considerable efforts have been devoted to designing cathodes that can either kinetically/physically constrain sulfur into conductive porous carbonaceous materials or thermodynamically

sequester it by chemical bonding. Among numerous architectures, PAN is a promising candidate as common carbon precursor and also due to its plentiful nitrile groups, which can strongly associate with LiPS through coordination bond-like interactions. First reported carbonized sulfur/PAN (SPAN) composite reached specific capacitance of 850 mAh/g_{composite} in the first cycle, and 600 mAh/g_{composite} after 50 cycles [272,273]. Significantly, no LiPS shuttling was observed and the utilization of sulfur achieved 90%. SPAN was obtained through co-pyrolysis of commercial PAN and S at 300 °C. The remarkable performance of SPAN was attributed to its mixed molecular structure where sulfur was non-covalently embedded into the cyclized PAN chain. However, such structures were further clarified experimentally pointing to the existence of C-

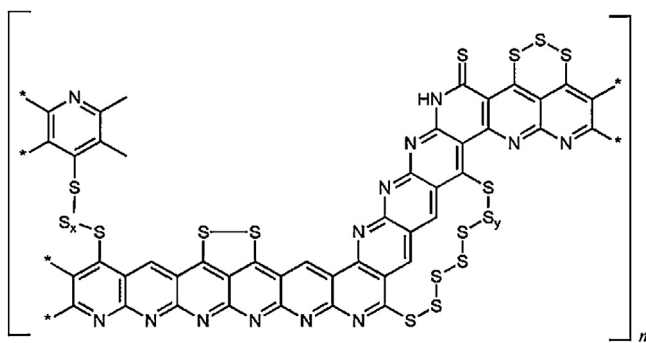


Fig. 43. Proposed structure of SPAN, containing all relevant functional groups ($0 < x < 6$; $y = 1,2$). [275]. Copyright 2011. Reproduced with permission from American Chemical Society.

S_x -C covalent bonds. (Fig. 44) [274,275]. Due to the existence of such thermally unstable sulfur bridges, sulfur content in SPAN is greatly influenced by the synthesis temperature. Lower temperature is usually needed to retain more electrochemically active sulfur in SPAN, while higher temperature is critical to achieve higher C-rate capabilities as well as cycle stability due to improved conductivity originating from higher graphitization degree of PAN [276]. Varying the sulfur/PAN ratio in the initial mixture can also help adjust the sulfur content in SPAN composite [277]. SPAN pyrolyzed at 450°C was used as the cathode and exhibited capacitance of over $1000 \text{ mA h/g}_{\text{composite}}$ even after 1000 cycles with very little fading and 100% Coulombic efficiency (Fig. 42). No LiPS shuttling was observed as the sulfur was covalently linked to the carbon backbone containing pyridinic-N atoms, and proposed to exist only in S_3/S_2 forms [278]. An even higher specific capacity of up to $1630 \text{ mA h/g}_{\text{composite}}$ after 100 cycles was reported with an over five-electron redox reaction mechanism [279]. However, this value was measured using a much lower current density. Remarkably,

the discharge capacity of the first cycle can reach values larger than the theoretical capacity of sulfur. This was explained by the additional Faradaic processes occurring due to the presence of pyridinic N atoms in SPAN (Fig. 43) that introduce pseudocapacitance and contribute to the overall capacity.

PAN can also be mixed with Li_2S as cathode materials. The use of Li_2S obviates the need of metallic lithium anodes, and avoids the volume expansion problem existing in most sulfur cathodes. Due to the interaction between lithium ions and nitrile groups, Li_2S was uniformly distributed in carbon matrix by dissolving with PAN in DMF before pyrolysis [280]. A reversible capacity of approximately $900 \text{ mA h g}^{-1}_{\text{Li}_2\text{S}}$ was achieved, approaching the theoretical capacity of Li_2S (1166 mAh/g). In addition to Li_2S and pristine sulfur, PAN can also be mixed with other materials to achieve better cathode design. A novel PAN-S@MWCNT composite with a robust core-shell structure was prepared by grafting poly(AN-co-IA) from the MWNCT by conventional FRP and subsequently pyrolyzing the obtained composite with S [281]. The rough and thin PAN shell increased the interaction area with sulfur, while the evenly distributed MWCNTs endowed the system with increased conductivity and stability. All of these contributed to the slow rate of capacity fading, stable specific capacity at 600 mA h/g after 50 cycles, as well as excellent rate capability. Using a similar synthetic route, the same group also developed SPAN/reduced-GO composite, which showed similar improvement as the PAN-S@MWCNT system [282]. PAN@carbon nanofiber interlayer with high conductivity and sustainable porous structure enabling strong trapping of LiPS was synthesized [283]. As a result, the sulfur cathodes delivered superior rate capability and cycle stability, 710 mAh/g after 200 cycles.

Recently, fibrous SPAN pyrolyzed from commercially PMMA/PAN textile fibers at 550°C was also tested as cathode for Li-S batteries, and found to show even better performance compared to particulate SPAN, namely perfect initial capacitances of $1672 \text{ mA h g}^{-1}_{\text{sulfur}}$, higher rate capabilities up to 8C, and

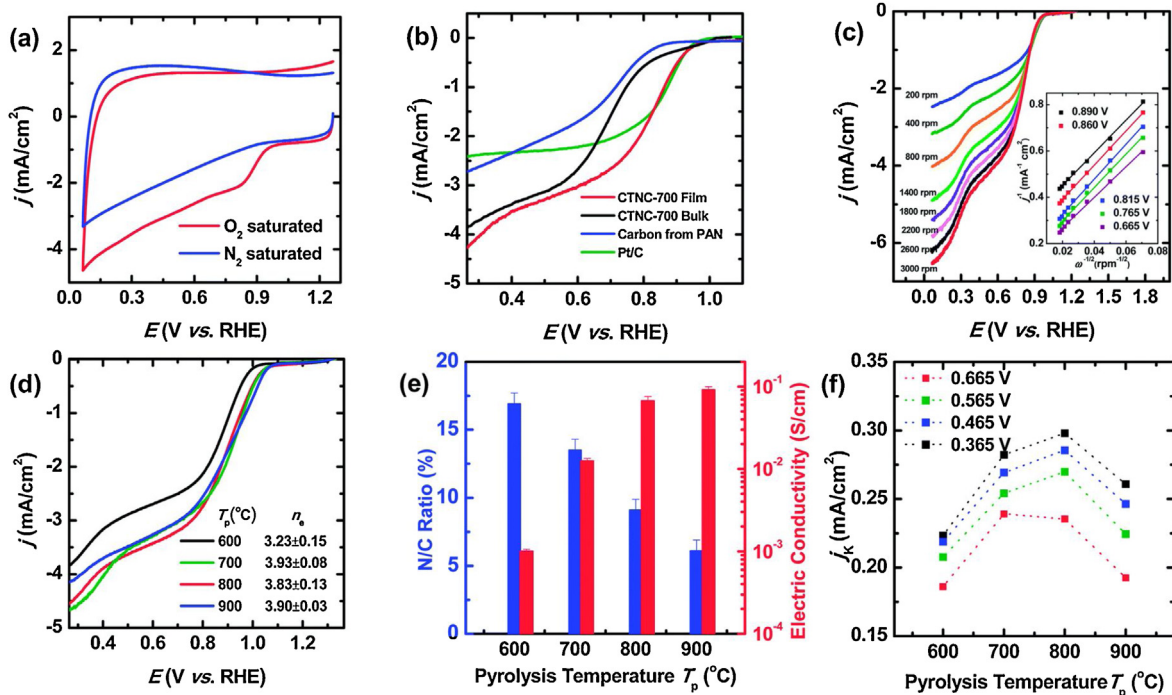
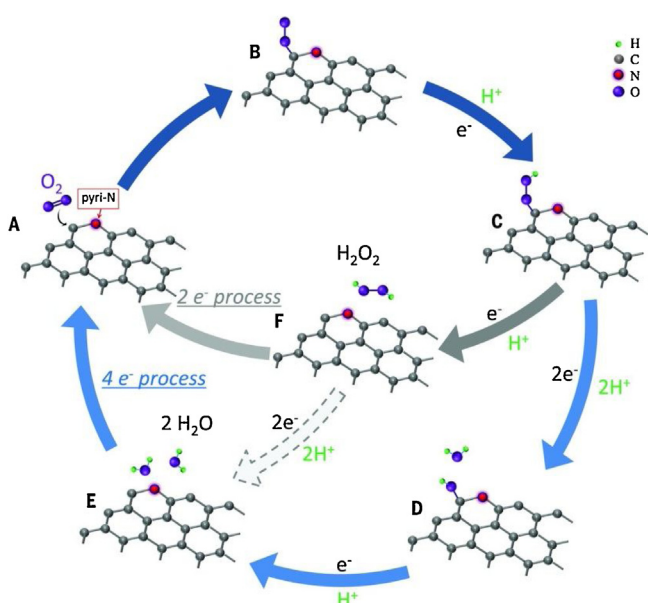


Fig. 44. (A) CV of CTNC in O₂- and N₂-saturated 0.1 mol L⁻¹ KOH solutions; (B) polarization curves at rotating speed of 1400 rpm; (C) polarization curves of CTNC-700 at different rotating speeds and K-L plots derived from (C) (inset). (D) Polarization curves of CTNC pyrolyzed at different temperatures at rotating speed of 1400 rpm; (E) effect of T_p on the N/C ratio (blue bars), electrical conductivity (red bars); (F) kinetic currents at different potentials calculated from the K-L equation. [295], Copyright 2014. Reproduced with permission from Royal Society of Chemistry.



Scheme 12. Two possible pathways for the metal-free ORR catalyzed by N-doped carbons. [26]. Copyright 2015. Reproduced with permission from The American Association for the Advancement of Science.

excellent cycle stabilities. Such performance improvement was attributed to the porous, fibrous morphology, which provides better access to a crack-free cathode coating to both electrons and lithium ions [284].

In addition to cathode materials, PAN is also a suitable polymer for use as a battery separator. A highly porous PAN/GO nanofiber membrane was demonstrated as a sustainable separator and largely suppressed the severe self-discharge phenomena in most Li-S batteries [285]. The improved performance was also partially ascribed to the high binding energy between nitrile group and LiPS.

4.3. Electrocatalysis

4.3.1. Oxygen reduction reaction (ORR)

ORR is a crucial reaction in clean energy technologies such as fuel cells and metal-air batteries. Fuel cells were first developed in the 1960s for the Apollo lunar mission, however their larger scale commercial application has been limited due to high costs of platinum, the most efficient ORR electrocatalyst. Thus, various strategies are being developed to either reduce Pt content, e.g., by alloying or increasing catalyst's porosity [286–288], or replace it with equally-performing non-noble metal or metal-free substitutes [17,289,290].

ORR is a complex, multistep process that can undergo two main pathways, namely 2 or 4 electron (e^-), where the former yields hydrogen peroxide and the latter is desired in fuel cells (Scheme 12). Typical experimental setup involves a familiar three-electrode system with either an alkaline (KOH) or acidic (H_2SO_4) electrolyte. The number n of electrons transferred is usually calculated by performing so-called Koutecky-Levich (K-L) analysis of polarization curves using rotating disk electrode (RDE) measurements, however, there are also other more accurate methods [291].

Interestingly, the first report on PAN as precursor to noble-metal-free ORR electrocatalyst dates back to 1989 [292]. PAN was co-dissolved in DMF with Co(II) or Fe(II) salts and carbonized with small amount of carbon black to enhance SSA. The as-prepared materials catalyzed ORR via the $4 e^-$ mechanism. Furthermore, with no metal added, ORR activity was also observed, although according to the $2 e^-$ mechanism. Pyridinic N atoms in the PAN-derived

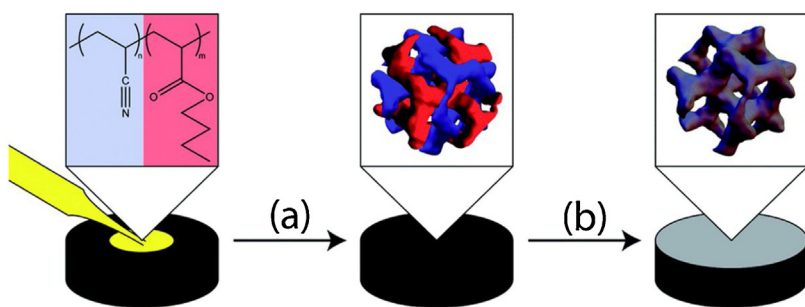
carbon were suggested to coordinate metals and form active sites able to adsorb O_2 molecules. In a following report, various metals co-pyrolyzed with PAN as ORR catalysts were compared. Since the activities recorded in acidic and alkaline electrolytes did not follow the same trend, it was suggested that PAN-derived carbon was itself catalytically active, especially under alkaline conditions [293]. Subsequently, a PAN-derived carbon foam loaded with very low amounts of Pt NPs ($13 \mu g/cm^2$) was reported to exhibit similar ORR activity than a Pt disk in acidic conditions [294].

In recent years NDCs have been widely recognized as superior ORR catalysts, in both standalone, metal-free systems [17,25] or as supports in metal-nitrogen-doped carbons (usually with Co, Fe or Ni) [35,36]. Detailed mechanistic studies revealed that distortion in electron density, caused by doping with more electronegative nitrogen, induces a net positive charge on adjacent carbon atoms, making them capable of adsorbing an oxygen molecule (Scheme 12). Pyridinic and graphitic (quaternary) N-dopants were demonstrated to mainly influence the ORR activity of a model N-doped graphene [26]. On the other hand, in metal-N-doped carbons active sites are porphyrin-like structures comprised of metal ions coordinated with edge-site N atoms [35].

High content of accessible pyridinic N atoms makes CTNCs excellent ORR catalysts. One unique feature of a polymeric precursor is the possibility to drop-cast it from solution onto a glassy carbon (GC) electrode to form a thin film that is then carbonized (Scheme 13). This simple method makes the use of a binder, such as Nafion, unnecessary and thus offers a feasible approach to fabricate thin carbon electrodes for model studies of catalytic activity [295]. Fig. 44 a–c present a comprehensive characterization of CTNC as ORR electrocatalyst in 0.1 M KOH electrolyte. A CTNC film prepared by the binder-free approach and carbonized at $700^\circ C$ was used as working electrode, with Ag/AgCl reference electrode and Pt counter electrode (CE). Emergence of a strong cathodic peak with onset potential of $0.955 V$ vs reversible hydrogen electrode (RHE) was observed in the CV spectrum when the system was purged in oxygen. Remarkably, this overpotential was lower than commercial Pt/C catalysts ($0.87 V$ vs RHE) as confirmed by a direct comparison of linear sweep voltammogram (LSV). Interestingly, the binder-free films performed significantly better than electrodes prepared using the traditional binder approach, i.e. casting of carbon powder dispersed in a Nafion solution. K-L analysis of LSVs recorded using RDE in the potential range of 0.365 – $0.890 V$ confirmed that ORR proceeded via the $4 e^-$ pathway with $n = 3.93$ [295].

Fig. 44 d–f compares the activities of CTNC electrodes prepared at different T_p . As discussed above, the best performance was found for electrodes pyrolyzed at 700 and $800^\circ C$, due to optimal interplay between conductivity and N-content. Pyrolysis at $600^\circ C$ did not provide sufficient conductivity and resulted in sloppy kinetics, with higher onset overpotential and $n = 3.23$. The CTNC-900 exhibited only slightly more negative onset than CTNC-700 and CTNC-800 and $n = 3.90$, since it still possessed relatively high nitrogen content (ca. 5 at.%). Further study revealed dependence of catalytic performance on the film thickness, i.e. catalyst loading [295].

It should be noted that excellent ORR performance of both nitrogen-doped carbons and transition metal-nitrogen carbon materials spurred a debate as to the origin of the 'metal-free' catalytic activity of NDC [296,297]. Specifically, it was suggested that trace metal impurities e.g. from catalysts used to synthesize various types of NDC, were in fact responsible for the observed activity. However, NDC synthesized via metal-free routes performed at the same level [20]. Due to these concerns, and despite Cu is not as active in ORR as Ni, Fe or Co, the PBA-*b*-PAN precursors to CTNC were subjected to a thorough, multistep purification by consecutive precipitation/dissolution in order to reduce the residual copper concentration below 1 ppm, as confirmed by ICP-MS. In order to further minimize this issue, novel techniques to synthe-



Scheme 13. Preparation of binder-free CTNC film on GC disk electrode. (a) Solvent evaporation at ambient conditions and thermal annealing at 160 °C under vacuum; (b) stabilization at 280 °C in air and pyrolysis at 600–900 °C, inert atmosphere. [295], Copyright 2014. Reproduced with permission from Royal Society of Chemistry.

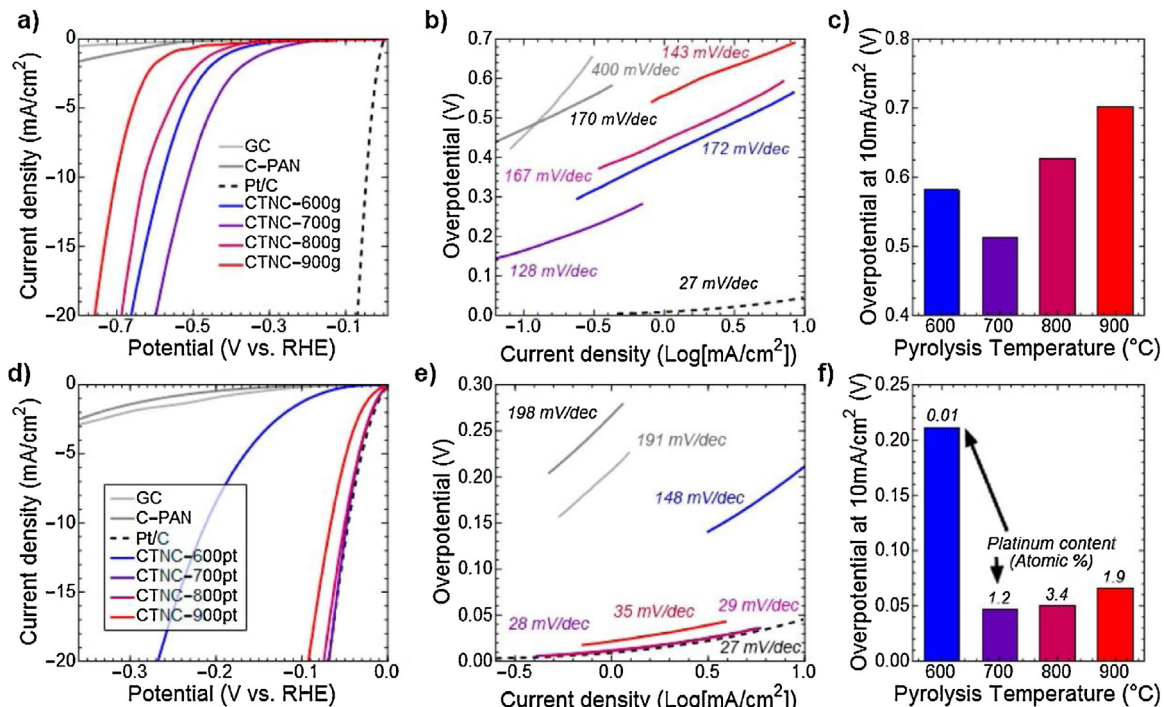


Fig. 45. Electrochemical activity of CTNCs prepared under different T_p . (a) Linear sweep voltammograms (20 mV/s) recorded in 0.5 M H₂SO₄ with a graphite CE after 1000 initial CV scans between 0 and -0.8 V vs SCE (at 100 mV/s). (b) Tafel plots and (c) operating overpotentials as a function of T_p corresponding to polarization curves and in (a). (d) Linear sweep voltammograms (20 mV/s) recorded in 0.5 M H₂SO₄ with a Pt mesh CE after 1000 initial CV scans between 0 and -0.8 V vs SCE (at 100 mV/s). (e) Tafel plots corresponding to polarization curves and in (d). (f) Operating overpotentials and as a function of T_p ; numbers above the bars indicate amount of Pt in the vicinity of the surface measured by XPS. [300], Copyright 2016. Reproduced with permission from American Chemical Society.

size PAN with low catalyst concentrations or even by metal-free systems have been recently developed, as discussed in Section 2. High ORR activity was also confirmed for NDCs prepared from PAN-based bottlebrushes [257] as well as hard-templated from aqueous PAN/ZnCl₂ solutions [250].

4.3.2. Hydrogen evolution reaction (HER)

HER is the cathodic half-reaction of the electrochemical water splitting process. Hydrogen can be used as a clean fuel feedstock in fuel cells, making HER of great technological importance [298]. Since water splitting requires large overpotential of 1.23 V, a heterogeneous electrocatalyst is needed to facilitate the reaction. HER consists of three main steps in acidic media: (1) electrochemical hydrogen adsorption (Volmer step) $H^+ + e^- \rightarrow H_{ads}$; (2) electrochemical desorption (Heyrovsky step) $H_{ads} + H^+ + e^- \rightarrow H_{2(g)}$; (3) chemical desorption (Tafel step) $2H_{ads} \rightarrow H_{2(g)}$ and the reaction may occur either via the Volmer-Heyrovsky or Volmer-Tafel mechanism. The rate limiting steps are determined by evaluating the slopes of plots of overpotential as a function of the logarithm of cur-

rent density in LSV (Tafel plots) [290,299]. However, just as in the case of ORR, the most efficient HER catalyst is Pt, which limits the widespread use of water electrocatalysis as hydrogen source. There has been an intensive search for noble-metal free HER electrocatalyst, with the most promising class of materials being transition metal dichalcogenides, such as MoS₂ [290,298].

Binder-free CTNC films were used to investigate the HER activity of PAN-derived NDC [300]. However, activity of NDC, commonly denoted as an overpotential needed to achieve current density $j = 10 \text{ mA/cm}^2$ (0.5–0.7 V vs RHE, Fig. 45 a, did not approach the activity of Pt (ca. 0.05 V vs RHE). The plausible explanation is the different nature of active sites necessary for proton adsorption. Namely, in the first step of a HER, protons adsorb at N-edge atom sites, unlike ORR, where O₂ molecules adsorb at carbon atoms adjacent to N dopants. Given the relatively low N content in NDC, this makes adsorption the rate limiting step and leads to slow kinetics. This was confirmed by analysis of Tafel slopes, which showed values between 120–143 mV/decade, indicating adsorption as the rate limiting step, Fig. 45 b. Furthermore, this level of activity was

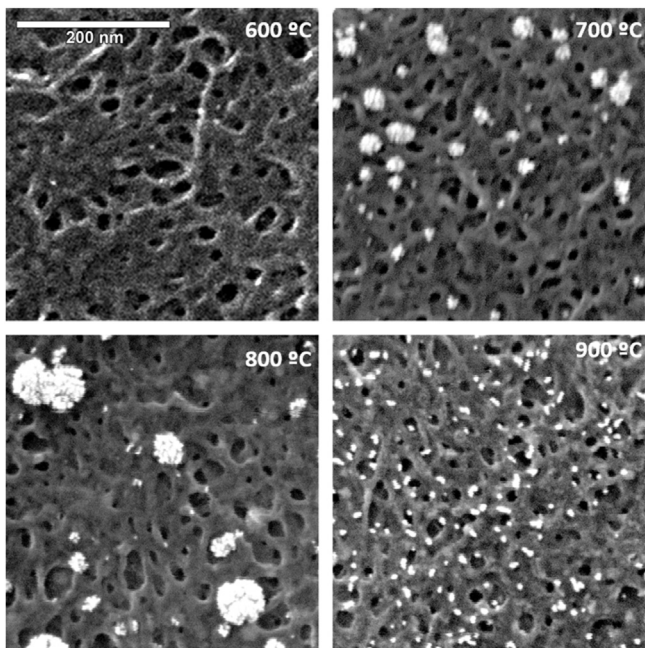


Fig. 46. SEM images of CTNC films fabricated at different temperature after potential cycling with Pt CE in 0.5 M H₂SO₄. [300]. Copyright 2016. Reproduced with permission from American Chemical Society.

in line with previous reports on NDC as metal-free HER catalysts [27,28]. Some methods have been proposed to increase the number of active sites, e.g. creating a composite from NDC which provides good conductivity and electron transfer properties, with g-C₃N₄ which, while being a semiconductor, has high N-content [27,301]. Performance of such composites was demonstrated to be close to Pt. Metal-nitrogen-doped carbon catalysts were also shown to exhibit much better activity than metal-free NDC [37].

Unfortunately, inadvertent Pt incorporation in NDC-based HER catalyst arises from the use of a Pt CE when testing the catalytic properties in acidic media. We have addressed this issue by comparing activities of CTNC films in 0.5 M H₂SO₄ with graphite and platinum CEs. Strikingly, when a Pt electrode was used, an immediate jump of catalytic activity was observed, marked by a decrease of overpotential at 10 mA/cm² to values <0.1 V vs RHE with Tafel slopes in the range of 26–35 mV/dec, i.e. the level of commercial Pt/C catalyst. Post-reaction XPS and SEM measurements revealed that during potential cycling Pt slowly dissolved in H₂SO₄ and deposited on the surface of the working electrode (Fig. 46). This process was efficient for deposition of Pt on NDC due to stabilization of nucleating Pt NPs by pyridinic N atoms, as confirmed by detailed analysis of high resolution N 1 s XPS spectra. 1–3 % of the deposited Pt on the NDC resulted in activity that was comparable with commercial Pt/C. Moreover, CTNC-600, which, due to low conductivity seemed to not adsorb any Pt, also showed slight activity improvement. High resolution XPS demonstrated that as low as 0.01 % of deposited Pt could enhance the performance of the NDC catalyst [300].

4.3.3. Dye-Sensitized Solar Cells (DSSCs)

DSSCs utilize thin film photovoltaic cells that use nanostructured TiO₂ doped with a photosensitive dye to harvest light and create an electronic excited state. The electrons flow through an external circuit to the cathode (i.e. counter electrode) where they are used to reduce a redox pair, usually I⁻/I₃⁻, which subsequently regenerates the photosensitizer. Pt based CEs are commonly used in DSSCs. Thus, based on previous positive results when replacing Pt with CTNC, they were also tested as CEs in DSSCs [262]. CTNCs

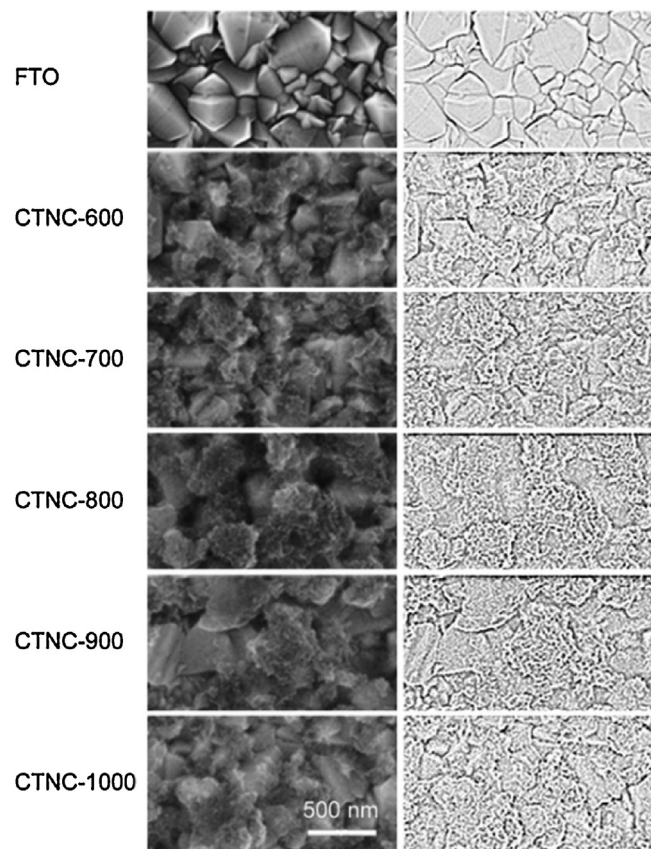


Fig. 47. SEM images (left column) and corresponding high-pass filtered images of CTNCs pyrolyzed at different temperatures and subsequently spray-coated on FTO electrodes. The high-pass images (right column) show the high surface area nanostructure afforded by the CTNC coating. [262]. Copyright 2015. Reproduced with permission from Royal Society of Chemistry.

carbonized at temperatures 600–1000 °C were electrosprayed onto fluorine-doped tin oxide (FTO) glass to prepare uniform, porous electrodes, Fig. 47. A DSSC was then constructed using Co(bpy)₃^{2+/3+} redox couple and JK-306 dye. The CTNCs efficiently reduced the Co(bpy)₃³⁺ due to low charge transfer resistance (R_{CT}). When the CTNC-800 CE was used, the power conversion efficiency (PCE) and fill factor (FF) of the JK-306/Co(bpy)₃^{2+/3+} redox couple increased by 10.32% and 73.5%, respectively, under one sun illumination as compared to 9.80% and 70.1%, respectively, for Pt CE. However, no similar improvement was observed when I⁻/I₃⁻ redox couple and ruthenium-based N719 dye were used. Additionally, after 100 potential cycles with Co(bpy)₃^{2+/3+} in acetonitrile, R_{CT} values for CTNC-800 only slightly increased, while for Pt CEs an increase by nearly 400% was observed, indicating better stability of CTNC-based CE [262].

4.4. CO₂ utilization and heavy metal adsorption

Global efforts to mitigate the climate change are widely acknowledged as one of the major challenges facing science and technology. Carbon dioxide has been unanimously recognized as the largest contributor to the greenhouse effect, however, ca. 500 gigatonnes of CO₂ are projected to be produced between 2010 and 2060 from burning the fossil fuels [302].

There are two main pathways to offset the effects of the continuing vast CO₂ emissions: 1) successive transition to clean energy alternatives, such as solar, wind, geothermal or hydrogen, and 2) utilize the produced CO₂ and prevent it from entering the atmosphere. This, in turn, can be realized either by so-called carbon

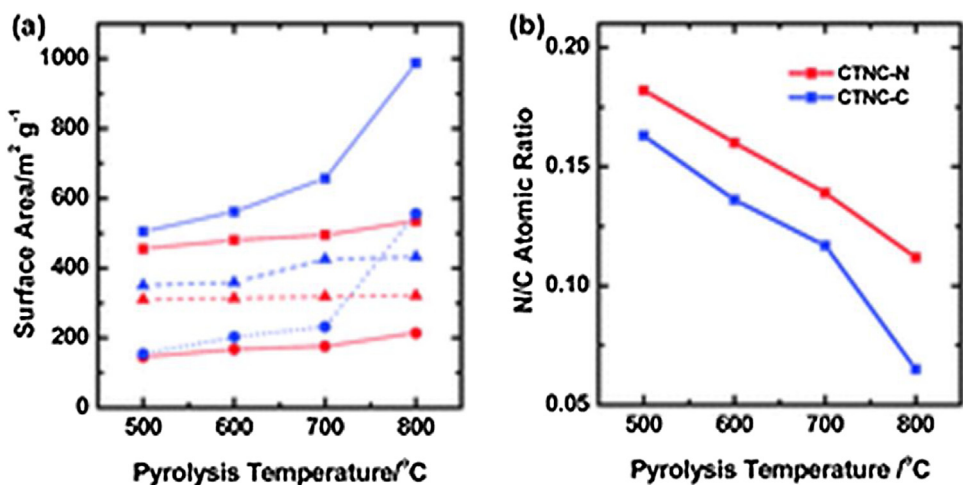


Fig. 48. (a) Effect of T_p on surface area (red: CTNC-N; blue: CTNC-C; solid line-squares: S_{BET} ; dot line-circles: S_{micro} ; dash line-triangles: S_{meso}); (b) Effect of T_p on N/C atomic ratio. [303], Copyright 2012. Reproduced with permission from Royal Society of Chemistry.

capture and storage or by catalytic reduction of CO_2 to useful chemicals, such as CO, hydrocarbons or methanol.

Various porous materials such as zeolites, metal-organic frameworks and nanocarbons have been investigated as CO_2 sorbents with high capacity, fast adsorption/desorption kinetics and good

selectivity over N_2 . The CO_2 adsorption properties of CTNC prepared by pyrolysis under either N_2 or CO_2 atmosphere were investigated [303]. As previously mentioned, using CO_2 during carbonization is known to activate the material by introducing additional microporosity, although simultaneously decreasing the

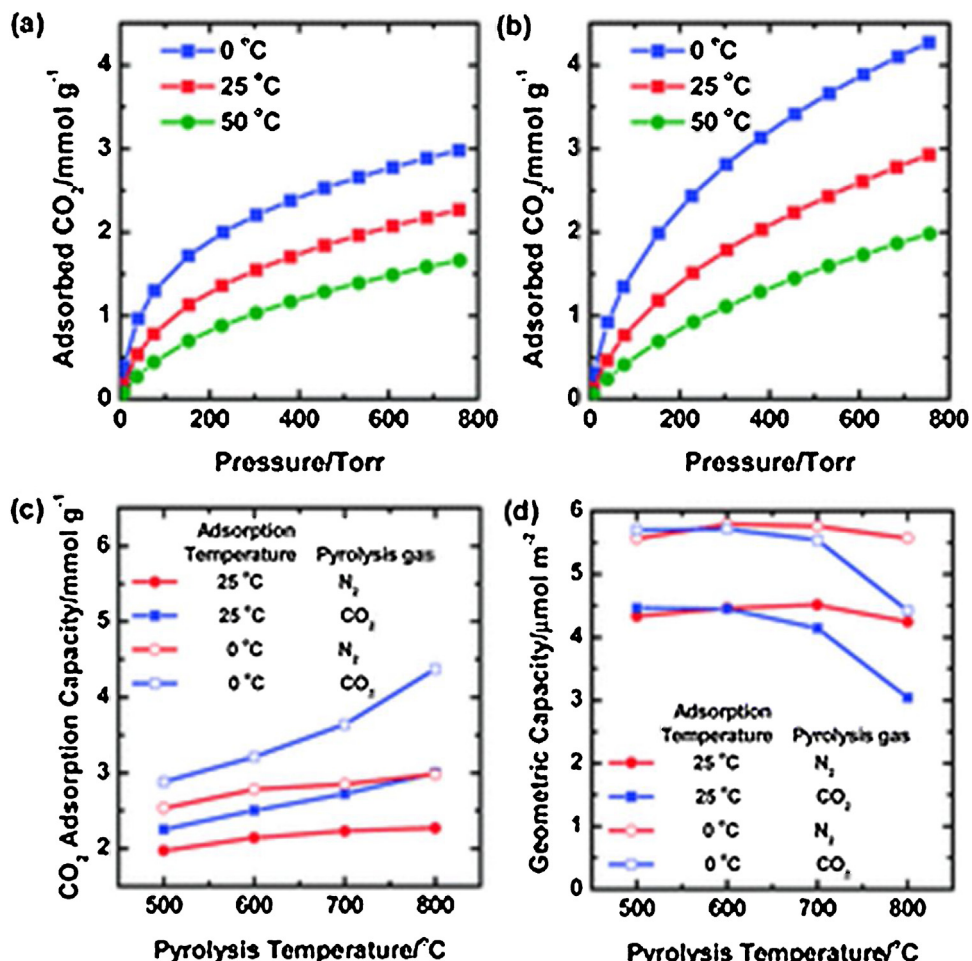


Fig. 49. (a) CO_2 adsorption isotherm of CTNC-N800; (b) CO_2 adsorption isotherm of CTNC-C800; (c) Effect of T_p on CO_2 adsorption capacity of CTNCs (0 and 25 °C, ambient pressure); (d) Effect of T_p on CO_2 adsorption capacity per unit surface area (0 and 25 °C, ambient pressure). [303], Copyright 2012. Reproduced with permission from Royal Society of Chemistry.

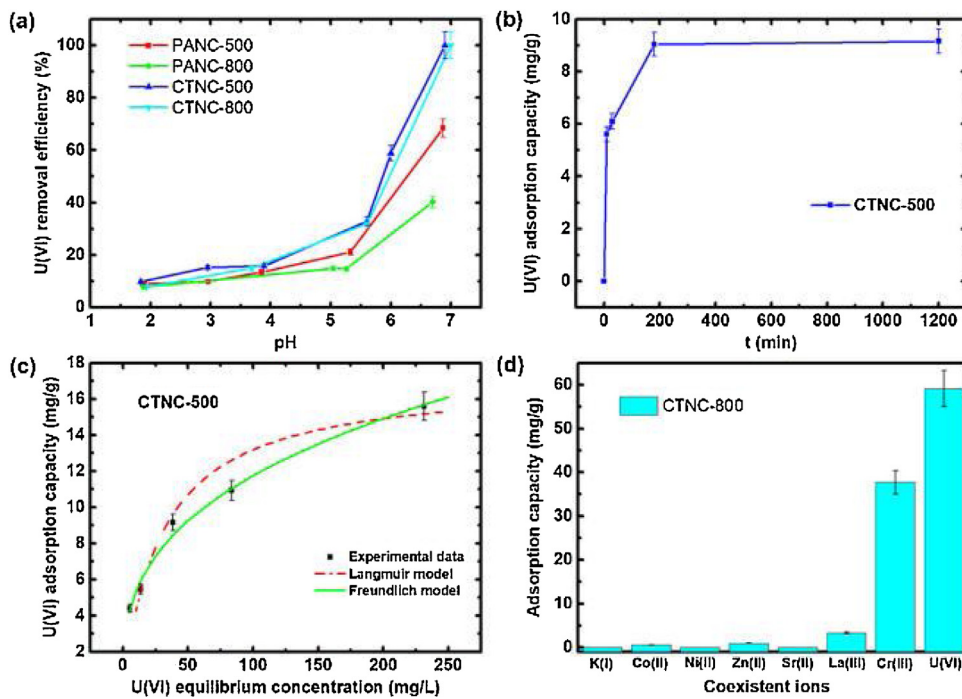


Fig. 50. Adsorption experiments: (a) U(VI) adsorption by PANCs and CTNCs at pH = ~2 – 7 ($M_{\text{carbon}}/V = 1 \text{ g/L}$); (b) U(VI) adsorption rate by CTNC-500 at pH = 5 ($M_{\text{carbon}}/V = 1 \text{ g/L}$); (c) U(VI) adsorption isotherms by CTNC-500 at pH = 5 ($M_{\text{carbon}}/V = 1 \text{ g/L}$); (d) adsorption selectivity of CTNC-800 on U(VI) ($M_{\text{carbon}}/V = 2 \text{ g/L}$). [305]. Copyright 2018. Reproduced with permission from the American Chemical Society.

N-content. However, as shown in Fig. 48, pyrolysis under CO_2 significantly enhanced the SSA only when pyrolysis was performed at 800°C . Namely, S_{micro} increased from 200 to $450 \text{ m}^2/\text{g}$ for 700 and 800°C , respectively. At lower T_p , the S_{BET} and, importantly, S_{micro} values remained similar.

CO_2 adsorption measurements at 0 – 50°C showed that CTNCs carbonized under both conditions exhibited significant sorption capacity, however samples pyrolyzed in CO_2 showed better performance due to higher SSA (Fig. 49 a–b). The T_p also had influence on adsorption capacity, especially for samples pyrolyzed under CO_2 . However, geometric adsorption capacity, that is, adsorption capacity per unit surface area interestingly decreased for the samples with the largest SSA (Fig. 49 d). This points out that the additional micropores created by carbonization under CO_2 at 800°C did not significantly contribute to the total adsorption capacity. The marked capacity decrease was then attributed to the sharp decrease in the N-content of the carbons formed under these conditions. The importance of N atoms was confirmed by correlating selectivity for CO_2 over N_2 with the N-content, which was 7–10 times higher [303]. It should be noted that the influence of N-content on the CO_2 adsorption has been highly debated in the literature, with some reports suggesting no influence of heteroatoms for the overall performance and that CO_2 adsorption depends exclusively on the SSA and porosity of the carbon [304].

Another method to utilize CO_2 is its reduction to useful chemicals, e.g. CO by electro- or photo-chemical means. Since NDC proved to be promising ORR and HER electrocatalysts, they were also tested as CO_2 reduction electrocatalysts. Electrospun PAN nanofibers were stabilized at 350°C and carbonized at 1050°C to obtain a free-standing CNF mat [31]. CO_2 reduction was then studied in a three-electrode setup with a Pt CE, Ag reference electrode and 1-ethyl-3-methylimidazolium tetrafluoroborate (EMIM- BF_4^-) as the electrolyte. A strong cathodic peak was observed at -0.573 V vs SHE which was attributed to CO_2 reduction to CO. The CNF-based catalyst outperformed carbonized PAN film as well as Ag-based catalysts. At larger potentials (-1.14 V vs SHE) typical H_2 evolution

was observed, however a Faradaic efficiency for CO as high as 98% was recorded. The analogical mechanism to ORR was suggested to involve adsorption of CO_2 at a positively charged carbon atom adjacent to pyridinic N dopant, followed by its electrochemical reduction to CO. However, no kinetic studies were provided to confirm this mechanism.

Building on the observed high affinity to Pt and on their performance as CO_2 sorbents, CTNCs were recently tested as sorbents for other heavy metals, namely chromium and uranium. Both metals are of significant environmental concern and, additionally, adsorption of U is important in recycling of used nuclear fuel or in separating uranium from seawater.

CTNCs were found to efficiently remove both Cr(VI) and U(VI) from aqueous solutions with particular pH dependence [305]. The highest adsorption capacity of Cr(VI) was recorded at pH = 2 and reached $59.1 \text{ mg of Cr(VI)/(g of sorbent)}$. At higher pH deprotonation of the nitrogen sites led to weaker interaction between the carbon surface and the HCrO_4^- and CrO_4^{2-} anions and to a decreased adsorption efficiency.

In the case of uranium however, a reverse trend was observed. The highest adsorption capacity was observed at pH = 7. Namely CTNC-500 removed 100% of U(VI) from a 100 mg/mL aqueous solution (Fig. 50) and 75.3% from a 200 mg/mL solution ($M_{\text{CTNC}}/V = 1 \text{ g/L}$). At lower pH protonation of nitrogen active sites decreased the adsorption efficiency of the UO_2^{2+} cations to less than 10%. Comparison of CTNCs with carbonized PAN (PANC) prepared at two different temperatures (500 and 800°C) pointed out to the importance of both surface area and nitrogen content on the adsorption performance. Furthermore, adsorption experiments performed in a simulated wastewater showed good selectivity for complexing U(VI) over other heavy metal ions (Fig. 50d).

Noteworthy, PAN-based materials are often used as efficient uranium adsorbents after transforming the nitrile groups into amidoxime moieties [84,85,206–209].

5. Summary

This review encompassed the recent developments in using polyacrylonitrile as a precursor to nanostructured carbon materials. Attractiveness of PAN results from its commercial availability (i.e. global production of acrylonitrile amounts to 5 M tones/year, half of which is used to produce fibers) and established carbonization chemistry. Furthermore, controlled polymerization techniques such as ATRP and RAFT allow facile synthesis of well-defined PAN and its copolymers, which can be transformed into sophisticated carbon nanostructures with tailored morphologies including films, nanoparticles or mesoporous carbons.

Most importantly, soft-templating of PAN-*b*-PBA block copolymers was developed as a robust way to mesoporous carbons taking advantage of the efficient preservation of self-assembled morphologies. Copolymer-templated nanocarbons (CTNC) combine large surface areas with high nitrogen content of nitrogen, originating from the carbonized PAN block. One distinct feature of CTNC is unique exposition of predominantly pyridinic, nitrogen atoms located on the edge sites of pores generated by removing non-bonded interface between the blocks and simultaneous carbonization of PAN. This gives rise to excellent electrochemical activity and indeed, CTNCs as well as PAN-derived nanocarbons prepared by other methods, e.g. hard templating, have been already demonstrated as promising electrode materials in electrocatalysis and energy conversion/storage applications. Future research will most likely focus on more advanced PAN/carbon architectures enabled by emerging synthetic techniques as well as on still unexplored applications of nitrogen-doped carbons. Also, recent progress in metal-free polymerization methods will enable synthesis of high purity, well-defined PAN as precursor to carbon nanostructures for the next-generation applications in energy and electronics.

Acknowledgements

Support from NSF (DMR 1501324) is gratefully acknowledged. M.K. thanks Polish Ministry of Science and Higher Education ("Mobilnosc Plus" grant no. 1055/MOB/2013/0) for financial support. Extensive excerpts from Ref. [141] were adapted with permission from the American Chemical Society.

References

- [1] Dresselhaus MS. Future directions in carbon science. *Annu Rev Mater Sci* 1997;27:1–34.
- [2] Kroto HW, Heath JR, O'Brien SC, Curl RF, Smalley RE. C₆₀: buckminsterfullerene. *Nature* 1985;318:162–3.
- [3] Iijima S. Helical microtubules of graphitic carbon. *Nature* 1991;354:56–8.
- [4] Geim AK, Novoselov KS. The rise of graphene. *Nat Mater* 2007;6:183–91.
- [5] Thompson BC, Fréchet JMJ. Polymer–fullerene composite solar cells. *Angew Chem Int Ed* 2008;47:58–77.
- [6] Lu L, Zheng T, Wu Q, Schneider AM, Zhao D, Yu L. Recent advances in bulk heterojunction polymer solar cells. *Chem Rev* 2015;115:12666–731.
- [7] Bachtold A, Hadley P, Nakanishi T, Dekker C. Logic circuits with carbon nanotube transistors. *Science* 2001;294:1317–20.
- [8] Brady GJ, Way AJ, Safron NS, Evensen HT, Gopalan P, Arnold MS. Quasi-ballistic carbon nanotube array transistors with current density exceeding Si and GaAs. *Sci Adv* 2016;2, e1601240/1–10.
- [9] Stoller MD, Park S, Zhu Y, An J, Ruoff RS. Graphene-based ultracapacitors. *Nano Lett* 2008;8:3498–502.
- [10] Zhu Y, Murali S, Stoller MD, Ganesh KJ, Cai W, Ferreira PJ, et al. Carbon-based supercapacitors produced by activation of graphene. *Science* 2011;332:1537–41.
- [11] Kim KS, Zhao Y, Jang H, Lee SY, Kim JM, Kim KS, et al. Large-scale pattern growth of graphene films for stretchable transparent electrodes. *Nature* 2009;457:706–10.
- [12] Bae S, Kim H, Lee Y, Xu X, Park JS, Zheng Y, et al. Roll-to-roll production of 30-inch graphene films for transparent electrodes. *Nat Nanotechnol* 2010;5:574–8.
- [13] Jiang DE, Gao X, Nagase S, Chen Z. Properties of π-electrons in graphene nanoribbons and nanographenes. In: Akasaka T, Wudl F, Nagase S, editors. *Chemistry of nanocarbons*. Hoboken: John Wiley and Sons Ltd; 2010. p. 433–61.
- [14] Wang H, Maiyalagan T, Wang X. Review on recent progress in nitrogen-doped graphene: synthesis, characterization, and its potential applications. *ACS Catal* 2012;2:781–94.
- [15] Shen W, Fan W. Nitrogen-containing porous carbons: synthesis and application. *J Mater Chem A Mater Energy Sustain* 2013;1:999–1013.
- [16] Paraknowitsch JP, Thomas A. Doping carbons beyond nitrogen: an overview of advanced heteroatom doped carbons with boron, sulphur and phosphorus for energy applications. *Energy Environ Sci* 2013;6:2839–55.
- [17] Dai L, Xue Y, Qu L, Choi HJ, Baek JB. Metal-free catalysts for oxygen reduction reaction. *Chem Rev* 2015;115:4823–92.
- [18] Deng Y, Xie Y, Zou K, Ji X. Review on recent advances in N-doped carbons. *J Mater Chem A Mater Energy Sustain* 2016;4:1144–73.
- [19] Inagaki M, Toyoda M, Soneda Y, Morishita T. Nitrogen-doped carbon materials. *Carbon* 2018;132:104–40.
- [20] Zhang J, Dai L. Heteroatom-doped graphitic carbon catalysts for efficient electrocatalysis of oxygen reduction reaction. *ACS Catal* 2015;5:7244–53.
- [21] Hu C, Xiao Y, Zou Y, Dai L. Carbon-based metal-free electrocatalysis for energy conversion and storage. *Electrochim Energy Rev* 2018;1:184–112.
- [22] Zhang S, Tsuzuki S, Ueno K, Dokko K, Watanabe M. Upper limit of nitrogen content in carbon materials. *Angew Chem Int Ed* 2015;54:1302–6.
- [23] Li X, Wang H, Robinson JT, Sanchez H, Diankov G, Dai H. Simultaneous nitrogen doping and reduction of graphene oxide. *J Am Chem Soc* 2009;131:15939–44.
- [24] Yu SS, Zheng WT, Wen QB, Jiang Q. First principle calculations of the electronic properties of nitrogen-doped carbon nanoribbons with zigzag edges. *Carbon* 2008;46:537–43.
- [25] Gong K, Du F, Xia Z, Durstock M, Dai L. Nitrogen-doped carbon nanotube arrays with high electrocatalytic activity for oxygen reduction. *Science* 2009;323:760–4.
- [26] Guo D, Shibuya R, Akiba C, Saji S, Kondo T, Nakamura J. Active sites of nitrogen-doped carbon materials for oxygen reduction reaction clarified using model catalysts. *Science* 2016;351:361–5.
- [27] Zheng Y, Jiao Y, Zhu Y, Li LH, Han Y, Chen Y, et al. Hydrogen evolution by a metal-free electrocatalyst. *Nat Commun* 2014;5(3783):1–8.
- [28] Zheng Y, Jiao Y, Li LH, Xing T, Chen Y, Jaroniec M, et al. Toward design of synergistically active carbon-based catalysts for electrocatalytic hydrogen evolution. *ACS Nano* 2014;8:5290–6.
- [29] Jiao Y, Zheng Y, Davey K, Qiao SZ. Activity origin and catalyst design principles for electrocatalytic hydrogen evolution on heteroatom-doped graphene. *Nat Energy* 2016;1(16130):1–9.
- [30] Hu C, Dai L. Carbon-based metal-free catalysts for electrocatalysis beyond the ORR. *Angew Chem Int Ed* 2016;55:11736–58.
- [31] Kumar B, Asadi M, Pisasale D, Sinha-Ray S, Rosen BA, Haasch R, et al. Renewable and metal-free carbon nanofibre catalysts for carbon dioxide reduction. *Nat Commun* 2013;4(2819):1–8.
- [32] Zhang S, Kang P, Ubnske S, Brennaman MK, Song N, House RL, et al. Polyethylenimine-enhanced electrocatalytic reduction of CO₂ to formate at nitrogen-doped carbon nanomaterials. *J Am Chem Soc* 2014;136:7845–8.
- [33] Sharma PP, Wu J, RMT Yadav, Liu M, Wright CJ, Tiwary CS, et al. Nitrogen-doped carbon nanotube arrays for high-efficiency electrochemical reduction of CO₂: on the understanding of defects, defect density, and selectivity. *Angew Chem Int Ed* 2015;54:13701–5.
- [34] Wu J, Yadav RM, Liu M, Sharma PP, Tiwary CS, Ma L, et al. Achieving highly efficient, selective, and stable CO₂ reduction on nitrogen-doped carbon nanotubes. *ACS Nano* 2015;9:5364–71.
- [35] Zitolo A, Goellner V, Armel V, Sougrati MT, Mineva T, Stievano L, et al. Identification of catalytic sites for oxygen reduction in iron- and nitrogen-doped graphene materials. *Nat Mater* 2015;14:937–42.
- [36] Liang HW, Wei W, Wu ZS, Feng X, Müllen K. Mesoporous metal–Nitrogen-Doped carbon electrocatalysts for highly efficient oxygen reduction reaction. *J Am Chem Soc* 2013;135:16002–5.
- [37] Liang HW, Bruller S, Dong R, Zhang J, Feng X, Müllen K. Molecular metal-Nx centres in porous carbon for electrocatalytic hydrogen evolution. *Nat Commun* 2015;6(7992):1–8.
- [38] Lota G, Grzyb B, Machnikowska H, Machnikowski J, Frackowiak E. Effect of nitrogen in carbon electrode on the supercapacitor performance. *Chem Phys Lett* 2005;404:53–8.
- [39] Frackowiak E, Lota G, Machnikowski J, Vix-Guterl C, Béguin F. Optimisation of supercapacitors using carbons with controlled nanotexture and nitrogen content. *Electrochim Acta* 2006;51:2209–14.
- [40] Lin T, Chen IW, Liu F, Yang C, Bi H, Xu F, et al. Nitrogen-doped mesoporous carbon of extraordinary capacitance for electrochemical energy storage. *Science* 2015;350:1508–13.
- [41] Lai L, Potts JR, Zhan D, Wang L, Poh CK, Tang C, et al. Exploration of the active center structure of nitrogen-doped graphene-based catalysts for oxygen reduction reaction. *Energy Environ Sci* 2012;5:7936–42.
- [42] Hoffman WP, Naskar AK. Polymer precursor-derived carbon. *ACS Symp Ser* 2014;243.
- [43] Chuenchom L, Krahnert R, Smarsly BM. Recent progress in soft-templating of porous carbon materials. *Soft Matter* 2012;8:10801–12.
- [44] Kowalewski T, Tsarevsky NV, Matyjaszewski K. Nanostructured carbon arrays from block copolymers of Polyacrylonitrile. *J Am Chem Soc* 2002;124:10632–3.

- [45] Liang C, Hong K, Guiochon GA, Mays JW, Dai S. Synthesis of a large-scale highly ordered porous carbon film by self-assembly of block copolymers. *Angew Chem Int Ed* 2004;43:5785–9.
- [46] Zhang J, Deng Y, Wei J, Sun Z, Gu D, Bongard H, et al. Design of amphiphilic ABC triblock copolymer for templating synthesis of large-pore ordered mesoporous carbons with tunable pore wall thickness. *Chem Mater* 2009;21:3996–4005.
- [47] Werner JG, Hoheisel TN, Wiesner U. Synthesis and characterization of gyroidal mesoporous carbons and carbon monoliths with tunable ultralarge pore size. *ACS Nano* 2014;8:731–43.
- [48] Hesse SA, Werner JG, Wiesner U. One-pot synthesis of hierarchically macro- and mesoporous carbon materials with graded porosity. *ACS Macro Lett* 2015;4:477–82.
- [49] Liu C, Yu M, Li Y, Li J, Wang J, Yu C, et al. Synthesis of mesoporous carbon nanoparticles with large and tunable pore sizes. *Nanoscale* 2015;7:11580–90.
- [50] Tanaka S, Nishiyama N, Egashira Y, Ueyama K. Synthesis of ordered mesoporous carbons with channel structure from an organic–organic nanocomposite. *Chem Commun* 2005;2125–7.
- [51] Wan Y, Shi Y, Zhao D. Designed synthesis of mesoporous solids via nonionic-surfactant-templating approach. *Chem Commun* 2007;897–926.
- [52] Meng Y, Gu D, Zhang F, Shi Y, Yang H, Li Z, et al. Ordered mesoporous polymers and homologous carbon frameworks: amphiphilic surfactant templating and direct transformation. *Angew Chem Int Ed* 2005;44:7053–9.
- [53] Wang Y, Liu J, Christiansen S, Kim DH, Gösele U, Steinhart M. Nanopatterned carbon films with engineered morphology by direct carbonization of UV-Stabilized block copolymer films. *Nano Lett* 2008;8:3993–7.
- [54] Jang YH, Xin X, Byun M, Jang YJ, Lin Z, Kim DH. An unconventional route to high-efficiency dye-sensitized solar cells via embedding graphitic thin films into TiO₂ nanoparticle photoanode. *Nano Lett* 2012;12:479–85.
- [55] Sun Y, Huang W, Liou J, Lu Y, Shih K, Lin C, et al. Conversion from self-assembled block copolymer nanodomains to carbon nanostructures with well-defined morphology. *RSC Adv* 2015;5:105774–84.
- [56] Sun YS, Huang WH, Lin CF, Cheng SL. Tailoring carbon nanostructure with diverse and tunable morphology by the pyrolysis of self-assembled lamellar nanodomains of a block copolymer. *Langmuir* 2017;33:2003–10.
- [57] Xu F, Wu D, Fu R, Wei B. Design and preparation of porous carbons from conjugated polymer precursors. *Mater Today* 2017;20:629–56.
- [58] Zhang J, Zhao Z, Xia Z, Dai L. A metal-free bifunctional electrocatalyst for oxygen reduction and oxygen evolution reactions. *Nat Nanotechnol* 2015;10:444–52.
- [59] Xu F, Tang Z, Huang S, Chen L, Liang Y, Mai W, et al. Facile synthesis of ultrahigh-surface-area hollow carbon nanospheres for enhanced adsorption and energy storage. *Nat Commun* 2015;6(7221):1–12.
- [60] Tang Z, Liu S, Lu Z, Lin X, Zheng B, Liu R, et al. A simple self-assembly strategy for ultrahigh surface area nitrogen-doped porous carbon nanospheres with enhanced adsorption and energy storage performances. *Chem Commun* 2017;53:6764–7.
- [61] Chand S. Review carbon fibers for composites. *J Mater Sci* 2000;35:1303–13.
- [62] Morris EA, Matthew CW. Solution spinning of PAN-based polymers for carbon fiber precursors. In: Naskar A, Hoffman W, editors. *Polymer precursor-derived carbon*. Washington DC: American Chemical Society; 2014. p. 189–213.
- [63] Bashir Z. The hexagonal mesophase in atactic polyacrylonitrile: a new interpretation of the phase transitions in the polymer. *J Macromol Sci B* 2001;40:41–67.
- [64] Bashir Z, Rastogi S. The explanation of the increase in slope at the *t_{gin}* the plot of d-Spacing versus temperature in Polyacrylonitrile. *J Macromol Sci B* 2005;44:55–78.
- [65] Kaji H, Schmidt-Rohr K. Conformation and dynamics of atactic poly(acrylonitrile). 2. Torsion angle distributions in meso dyads from two-dimensional solid-state double-quantum ¹³C NMR. *Macromolecules* 2001;34:7368–81.
- [66] Iovleva M, Smirnova V, Budnitskii G. The solubility of polyacrylonitrile. *Fibre Chem* 2001;33:262–4.
- [67] Eom Y, Kim BC. Solubility parameter-based analysis of polyacrylonitrile solutions in N,N-dimethyl formamide and dimethyl sulfoxide. *Polymer* 2014;55:2570–7.
- [68] Huang X. Fabrication and properties of carbon fibers. *Materials* 2009;2:2369–403.
- [69] Frank E, Steudle LM, Ingildeev D, Sporl JM, Buchmeiser MR. Carbon fibers: precursor systems, processing, structure, and properties. *Angew Chem Int Ed* 2014;53:5262–98.
- [70] Bajaj P, Roopanwal AK. Thermal stabilization of acrylic precursors for the production of carbon fibers: an overview. *J Macromol Sci Polym Rev* 1997;37:97–147.
- [71] Liu X, Makita Y, Yi Hong, Nishiyama Y, Miyoshi T. Chemical reactions and their kinetics of atactic-polyacrylonitrile As revealed by solid-state ¹³C NMR. *Macromolecules* 2017;50:244–53.
- [72] Wang Y, Xu L, Wang M, Pang W, Ge X. Structural identification of Polyacrylonitrile during thermal treatment by Selective ¹³C labeling and Solid-State ¹³C NMR spectroscopy. *Macromolecules* 2014;47:3901–8.
- [73] Liu X, Chen W, Hong YL, Yuan S, Kuroki S, Miyoshi T. Stabilization of Atactic-Polyacrylonitrile under nitrogen and air as studied by solid-state NMR. *Macromolecules* 2015;48:5300–9.
- [74] Park SJ, Heo GY. Precursors and manufacturing of carbon fibers. In: Park SJ, editor. *Precursors and manufacturing of carbon fibers*. carbon fibers. Dordrecht: Springer; 2015. p. 31–66.
- [75] Yamazaki H, Miyazaki Y, Kamide K. Stereospecific polymerization of acrylonitrile using acrylonitrile–urea canal complex initiated by gamma-ray irradiation: roles of radical chain transfer reagents. *Polym J* 1991;23:765–79.
- [76] Minagwa M, Yamada H, Yamaguchi K, Yoshi F. Gamma-ray irradiation canal polymerization conditions ensuring high stereoregular (& 80%) poly(acrylonitrile). *Macromolecules* 1992;25:503–10.
- [77] Minagwa M, Nouchi K, Tozuka M, Chujo R, Yoshi F. Isotactic poly(acrylonitrile) via ultraviolet irradiation of Acrylonitrile–urea canal complex. *J Polym Sci Part A: Polym Chem* 1995;33:665–71.
- [78] Minagwa M, Okada Y, Nouchi K, Sato Y, Tacticity Yoshi F. Molecular weight and molecular-weight-distribution relationships in stereoregular polyacrylonitrile prepared by Electron beam irradiation canal polymerization. *Colloid Polym Sci* 2000;278:757–63.
- [79] Zou JT, Wang YS, Pang WM, Shi L, Lu F. Radiation-induced inclusion polymerization of acrylonitrile in urea canals: toward synthesis of completely isotactic polyacrylonitrile with controlled molecular weight. *Macromolecules* 2013;46:1765–71.
- [80] Sui K, Gu L. Preparation and characterization of amphiphilic block copolymer of polyacrylonitrile-block-Poly(ethylene oxide). *J Appl Polym Sci* 2003;89:1753–9.
- [81] Boguslavsky L, Baruch S, Margel S. Synthesis and characterization of polyacrylonitrile nanoparticles by dispersion/emulsion polymerization process. *J Colloid Interface Sci* 2005;289:71–85.
- [82] Cho DW, Oh KS, Bae W, Kim H, Lee YW. Synthesis of monodispersed poly(acrylonitrile) microspheres by dispersion polymerization in compressed liquid dimethyl ether. *Colloid Polym Sci* 2008;287:179–88.
- [83] Sui K, Liang H, Zhao X, Ma Y, Zhang Y, Xia Y. Synthesis of amphiphilic poly(ethylene oxide-co-glycidol)-graft-polyacrylonitrile brush copolymers and their self-assembly in aqueous media. *Macromol Chem Phys* 2012;213:1717–24.
- [84] Das S, Oyola Y, Mayes RT, Janke CJ, Kuo LJ, Gill G, et al. Extracting uranium from seawater: promising AF series adsorbents. *Ind Eng Chem Res* 2016;55:4110–7.
- [85] Kuo LJ, Janke CJ, Wood JR, Strivens JE, Das S, Oyola Y, et al. Characterization and testing of amidoxime-based adsorbent materials to extract uranium from natural seawater. *Ind Eng Chem Res* 2016;55:4285–93.
- [86] Khisti RS, Sivaram S, Dhal PK. Polymer-bound Metal-free carbanion as initiator for controlled grafting of acrylic polymers. *Macromolecules* 1994;27:2883–5.
- [87] Jiang Y, Zhang H, Du L, Zhang K, Wang J. Synthesis and characterization of novel star polymer with β-cyclodextrin core and its metal complexes. *J Appl Polym Sci* 2007;106:28–33.
- [88] Ca Cao, Zhuang X, Su Y, Zhang Y, Zhang F, Wu D, et al. 2D polyacrylonitrile brush derived nitrogen-doped carbon nanosheets for high-performance electrocatalysts in oxygen reduction reaction. *Polym Chem* 2014;5:2057–64.
- [89] Shirai H, Nagatomo Y, Inaki Y, Takemoto K. Vinyl polymerization by metal complexes. IV. Polymerization of acrylonitrile initiated by imidazole–copper(II) complex. *J Macromol Sci A* 1974;8:935–47.
- [90] Saegusa T, Horiguchi S, Tsuda T. Vinyl polymerization by cyclooctadienyl/copper (I) complexes. *Macromolecules* 1975;8:112–4.
- [91] Siemeling U, Kölling L, Stammiller A, Stammiller HG, Kaminski E, Fink G. Polymerisation of acrylonitrile with di(organoimido)chromium(vi) complexes. *Chem Commun* 2000;1177–8.
- [92] Shono T, Mori M, Shinra K. Polymerization of an catalyzed by methoxy-B-diketone nickel chelates. *J Polym Sci Part A1 Polym Chem* 1970;8:1981–6.
- [93] Tsuchihara K, Suzuki Y, Asai M, Soga K. Polymerization of polar vinyl monomers with novel cobalt-based catalyst. *Chem Lett* 1999;28:891–2.
- [94] Sivaram S, Dhal PK, Kashikar SP, Khisti RS, Shinde BM, Baskaran D. Tailoring carbanion strutures for controlled anionic polymerization of acrylonitrile. *Macromolecules* 1991;24:1697–8.
- [95] Nakano Y, Hisatani K. Highly isotactic polyacrylonitriles prepared using Dialkylmagnesium/water systems as initiators. *Polym Int* 1994;35:249–55.
- [96] Schapen F, Foley SR, Jordan RF. Acrylonitrile polymerization by Cy3CuMe and (Bipy)₂FeEt₂. *J Am Chem Soc* 2004;126:2114–24.
- [97] Ono H, Hisatani K, Kamide K. NMR spectroscopic study of side reactions in anionic polymerization of acrylonitrile. *Polym J* 1993;25:245–65.
- [98] Matyjaszewski K. Introduction to living polymerization. Living and/or controlled polymerization. *J Phys Org Chem* 1995;8:197–207.
- [99] Matyjaszewski K, Gaynor S, Greszta D, Mardare D, Shigemoto T. ‘Living’ and controlled radical polymerization. *J Phys Org Chem* 1995;8:306–15.
- [100] Matyjaszewski K, Davis TP. *Handbook of radical polymerization*. Hoboken, NJ: John Wiley and Sons Inc.; 2003. p. 935.
- [101] Matyjaszewski K, Xia J. Atom transfer radical polymerization. *Chem Rev* 2001;101:2921–90.
- [102] Matyjaszewski K, Tsarevsky NV. Nanostructured functional materials prepared by atom transfer radical polymerization. *Nat Chem* 2009;1:276–88.
- [103] Ouchi M, Terashima T, Sawamoto M. Transition-metal catalyzed living radical polymerization: toward perfection in catalysis and precision polymer synthesis. *Chem Rev* 2009;109:4963–5050.
- [104] Matyjaszewski K. Atom transfer radical polymerization (ATRP): current status and future perspectives. *Macromolecules* 2012;45:4015–39.

- [105] Golas PL, Mueller LA, Coote ML, Matyjaszewski K. Atom transfer radical polymerization. In: Mark HF, editor. Encyclopedia of polymer science and technology. 4 ed. Hoboken: John Wiley and Sons Inc; 2014. p. 720–45.
- [106] Matyjaszewski K, Tsarevsky NV. Macromolecular engineering by atom transfer radical polymerization. *J Am Chem Soc* 2014;136:6513–33.
- [107] Moad G, Rizzardo E, Thang SH. Radical addition-fragmentation chemistry in polymer synthesis. *Polymer* 2008;49:1079–131.
- [108] Moad G, Rizzardo E, Thang SH. Living radical polymerization by the RAFT process – a third update. *Aust J Chem* 2012;65:985–1076.
- [109] Hill MR, Carmean RN, Sumerlin BS. Expanding the scope of RAFT polymerization: recent advances and new horizons. *Macromolecules* 2015;48:5459–69.
- [110] Hawker CJ. LivingFree Radical Polymerization: A Unique Technique for the Preparation of Controlled Macromolecular Architectures. *Acc Chem Res* 1997;30:373–82.
- [111] Benoit D, Chiplinski V, Braslau R, Hawker CJ. Development of a universal alkoxamine for Livingfree radical polymerization. *J Am Chem Soc* 1999;121:3904–20.
- [112] Nicolas J, Guillaneuf Y, Lefay C, Bertin D, Gigmes D, Charleux B. Nitroxide-mediated polymerization. *Prog Polym Sci* 2013;38:63–235.
- [113] Patten TE, Matyjaszewski K. ATRP and the synthesis of polymeric materials. *Adv Mater* 1998;10:900–15.
- [114] Coessens V, Pintauer T, Matyjaszewski K. Functional polymers by atom transfer radical polymerization. *Prog Polym Sci* 2001;26:337–77.
- [115] Grishin DF, Grishin JD. Radical-initiated controlled synthesis of homo- and copolymers based on acrylonitrile. *Russ Chem Rev* 2015;84:712–36.
- [116] Kranz D, Baumann H, Pohl HU. Structure and properties of abs polymers.8 elution technique of homopolymers and copolymers from styrene and acrylonitrile in Gel Chromatography – assembly of calibration for solvents of different quality. *Angew Makromol Chem* 1972;26:67–84.
- [117] Mori S. Calibration of size exclusion chromatography columns for molecular weight determination of poly(acrylonitrile) and poly(vinylpyrrolidone) in N,N-dimethylformamide. *Anal Chem* 1983;55:2414–6.
- [118] Dong H, Tang W, Matyjaszewski K. Well-defined high-molecular-weight polyacrylonitrile via activators regenerated by electron transfer ATRP. *Macromolecules* 2007;40:2974–7.
- [119] Pan X, Lamson M, Yan J, Matyjaszewski K. Photoinduced metal-free atom transfer radical polymerization of acrylonitrile. *ACS Macro Lett* 2015;4:192–6.
- [120] Pietrasik J, Dong H, Matyjaszewski K. Synthesis of high molecular weight poly(styrene-co-acrylonitrile) copolymers with controlled architecture. *Macromolecules* 2006;39:6384–90.
- [121] Lamson M, Kopeć M, Ding H, Zhong M, Matyjaszewski K. Synthesis of well-defined polyacrylonitrile by ICAR ATRP with low concentrations of catalyst. *J Polym Sci Part A: Polym Chem* 2016;54:1961–8.
- [122] Matyjaszewski K, Jo SM, Paik H, Gaynor SG. Synthesis of well-defined polyacrylonitrile by atom transfer radical polymerization. *Macromolecules* 1997;30:6398–400.
- [123] Matyjaszewski K, Jo SM, Paik H, Shipp DA. An investigation into the CuX/2,2'-Bipyridine (X=Br or Cl) mediated atom transfer radical polymerization of acrylonitrile. *Macromolecules* 1999;32:6431–8.
- [124] Barbiou B, Percec V. Metal catalyzed living radical polymerization of acrylonitrile initiated by sulfonyl chlorides. *Macromolecules* 2001;34:8626–36.
- [125] Brar AS, Kaur S. Tetramethylguanidino-tris(2-aminoethyl)amine: a novel ligand for copper-based atom transfer radical polymerization. *J Polym Sci Part A: Polym Chem* 2005;43:5906–22.
- [126] Lazzari M, Chiantore O, Mendichi R, López-Quintela MA. Synthesis of polyacrylonitrile-block-polystyrene copolymers by atom transfer radical polymerization. *Macromol Chem Phys* 2005;206:1382–8.
- [127] Hou C, Ji C, Wang C, Qu R. A copper-based reverse atom-transfer radical polymerization process for the living radical polymerization of polyacrylonitrile. *J Polym Sci Part A: Polym Chem* 2006;44:226–31.
- [128] Hou C, Liu J, Wang C. Reverse atom-transfer radical polymerization of acrylonitrile catalyzed by FeCl₃/iminodiacetic acid. *Polym Int* 2006;55:171–5.
- [129] Hou C, Qu R, Ji C, Wang C, Wang C. Synthesis of polyacrylonitrile via reverse atom transfer radical polymerization catalyzed by FeCl₃/isophthalic acid. *J Polym Sci Part A: Polym Chem* 2006;44:219–25.
- [130] Hou C, Qu R, Liu J, Guo Z, Wang C, Ji C, et al. Reverse ATRP of acrylonitrile with diethyl 2,3-dicyano-2,3-diphenyl succinate/FeCl₃/iminodiacetic acid. *Polymer* 2006;47:1505–10.
- [131] Hou C, Qu R, Ji C, Wang C, Wang C. Synthesis of polyacrylonitrile via reverse atom transfer radical polymerization (ATRP) initiated by diethyl 2,3-dicyano-2,3-diphenylsuccinate, FeCl₃, and triphenylphosphine. *Polym Int* 2006;55:326–9.
- [132] Tang C, Kowalewski T, Matyjaszewski K. Preparation of polyacrylonitrile-block-Poly(n-butyl acrylate) using atom transfer radical polymerization and nitroxide mediated polymerization process. *Macromolecules* 2003;36:1465–73.
- [133] Chen H, Liu D, Song Y, Qu R, Wang C. ARGET ATRP of acrylonitrile with ionic liquid as reaction media and 1,1,4,7,7-pentamethyldiethylenetriamine as both ligand and reducing agent in the presence of air. *Polym Adv Technol* 2012;22:1513–7.
- [134] Yu YH, Liu XH, Jia D, Cheng BW, Ren YL, Zhang FJ, Li HN, et al. Ambient temperature copper-mediated living radical polymerization of acrylonitrile with Me6TREN as the reducing agent. *J Polym Sci Part A: Polym Chem* 2013;51:1690–4.
- [135] Liu XH, Wang J, Zhang FJ, An SL, Ren YL, Yu YH, Chen P, et al. Copper-mediated initiators for continuous activator regeneration atom transfer radical polymerization of acrylonitrile. *J Polym Sci Part A: Polym Chem* 2012;50:4358–64.
- [136] Liu XH, Wang J, Yang JS, An SL, Ren YL, Yu YH, Chen P. Fast copper catalyzed living radical polymerization of acrylonitrile utilizing a high concentration of radical initiator. *J Polym Sci Part A: Polym Chem* 2012;50:1933–40.
- [137] Yu YH, Liu XH, Jia D, Cheng BW, Zhang FJ, Li HN, Chen P, et al. “Nascent” Cu(0) nanoparticles-mediated single electron transfer living radical polymerization of acrylonitrile at ambient temperature. *J Polym Sci Part A: Polym Chem* 2013;51:1468–74.
- [138] Chen Q, Zhang Z, Zhou N, Cheng C, Tu Y, Zhu Y. Copper(0)-Mediated living radical polymerization of acrylonitrile at room temperature. *J Polym Sci Part A: Polym Chem* 2011;49:1183–9.
- [139] Liu XH, Zhang GB, Li BX, Bai YG, Li YS. Copper(0)-Mediated living radical polymerization of acrylonitrile: SET-LRP or AGET-ATRP. *J Polym Sci Part A: Polym Chem* 2010;48:5439–45.
- [140] Konkolewicz D, Wang Y, Krys P, Zhong M, Isse AA, Gennaro A, et al. SARA ATRP or SET-LRP. End of controversy? *J Polym Chem* 2014;5:4409–17.
- [141] Kopeć M, Yuan R, Gottlieb E, Abreu CMR, Song Y, Wang Z, et al. Polyacrylonitrile-b-poly(butyl acrylate) block copolymers as precursors to mesoporous nitrogen-doped carbons: synthesis and nanostructure. *Macromolecules* 2017;50:2759–67.
- [142] Junkers T, Koo SPS, Barner-Kowollik C. Determination of the propagation rate coefficient of acrylonitrile. *Polym Chem* 2010;1:438–41.
- [143] Tang W, Tsarevsky NV, Matyjaszewski K. Determination of equilibrium constants for atom transfer radical polymerization. *J Am Chem Soc* 2006;128:1598–604.
- [144] Tang W, Kwak Y, Braunecker W, Tsarevsky NV, Coote ML, Matyjaszewski K. Understanding atom transfer radical polymerization: effect of ligand and initiator structures on the equilibrium constants. *J Am Chem Soc* 2008;130:10702–13.
- [145] Matyjaszewski K, Jakubowski W, Min K, Tang W, Huang J, Braunecker WA, et al. Diminishing catalyst concentration in atom transfer radical polymerization with reducing agents. *Proc Natl Acad Sci U S A* 2006;103:15309–14.
- [146] Krys P, Matyjaszewski K. Kinetics of atom transfer radical polymerization. *Eur Polym J* 2017;89:482–523.
- [147] Trevisanello E, De Bon F, Daniel G, Lorandi F, Durante C, Isse AA, et al. Electrochemically mediated atom transfer radical polymerization of acrylonitrile and poly(acrylonitrile-*b*-butyl acrylate) copolymer as a precursor for N-doped mesoporous carbons. *Electrochim Acta* 2018;285:344–54.
- [148] Treat NJ, Sprafke H, Kramer JW, Clark PG, Barton BE, Read de Alaniz J, et al. Metal-free atom transfer radical polymerization. *J Am Chem Soc* 2014;136:16096–101.
- [149] Pan X, Fang C, Fantin M, Malhotra N, So WY, Peteanu LA, et al. Mechanism of photoinduced metal-free atom transfer radical polymerization: experimental and computational studies. *J Am Chem Soc* 2016;138:2411–25.
- [150] Tang C, Kowalewski T, Matyjaszewski K. RAFT polymerization of acrylonitrile and preparation of block copolymers using 2-cyanoethyl dithiobenzoate as the transfer agent. *Macromolecules* 2003;36:8587–9.
- [151] Chiehari J, Chong YK, Ercole F, Krstina J, Jeffery J, Le TPT, et al. Living free-radical polymerization by reversible addition-fragmentation chain transfer: the RAFT process. *Macromolecules* 1998;31:5559–62.
- [152] Chiehari J, Mayadunne RTA, Moad CL, Moad G, Rizzardo E, Postma A, et al. Thiocarbonylthio compounds ($S=C(Z)S-R$) in free radical polymerization with reversible addition-fragmentation chain transfer (RAFT polymerization). Effect of the Activating Group Z. *Macromolecules* 2003;36:2273–83.
- [153] Chong YK, Krstina J, Le TPT, Moad G, Postma A, Rizzardo E, Thang SH. Thiocarbonylthio compounds [$S=C(Ph)S-R$] in free radical polymerization with reversible addition-fragmentation chain transfer (RAFT polymerization). Role of the Free-Radical Leaving Group (R). *Macromolecules* 2003;36:2256–72.
- [154] An Q, Qian J, Yu L, Luo Y, Liu X. Study on kinetics of controlled/living radical polymerization of acrylonitrile by RAFT technique. *J Polym Sci Part A: Polym Chem* 2005;43:1973–7.
- [155] Liu XH, Zhang GB, Lu XF, Liu JY, Pan D, Li YS. Dibenzyl trithiocarbonate mediated reversible addition-fragmentation chain transfer polymerization of acrylonitrile. *J Polym Sci Part A: Polym Chem* 2006;44:490–8.
- [156] Liu XH, Li YG, Lin Y, Li YS. 2-Cyanoprop-2-yl dithiobenzoate mediated reversible addition-fragmentation chain transfer polymerization of acrylonitrile targeting a polymer with a higher molecular weight. *J Polym Sci Part A: Polym Chem* 2007;45:1272–81.
- [157] Niu S, Zhang L, Zhu J, Zhang W, Cheng Z, Zhu X. Synthesis of high molecular weight and narrow molecular weight distribution poly(acrylonitrile) via RAFT polymerization. *J Polym Sci Part A: Polym Chem* 2013;51:1197–204.
- [158] Moskowitz JD, Abel BA, McCormick CL, Wiggins JS. High molecular weight and low dispersity polyacrylonitrile by low temperature RAFT polymerization. *J Polym Sci Part A: Polym Chem* 2016;54:553–62.
- [159] Li J, Ding C, Zhang Z, Zhu J, Zhu X. Photo-induced reversible addition-fragmentation chain transfer (RAFT) polymerization of

- acrylonitrile at ambient temperature: a simple system to obtain high-molecular-weight polyacrylonitrile. *React Funct Polym* 2017;113:1–5.
- [160] Kopeć M, Krys P, Yuan R, Matyjaszewski K. Aqueous RAFT polymerization of acrylonitrile. *Macromolecules* 2016;49:5877–83.
- [161] Liu XH, Zhang GB, Li BX, Bai YG, Pan D, Li YS. Well-defined higher-molecular-weight polyacrylonitrile via RAFT technique in the presence of disulfide compounds as a source of chain transfer agent. *Eur Polym J* 2008;44:1200–8.
- [162] Kain A, Megiel E. Transition states for deactivation reactions in the modeled 2,2,6,6-tetramethyl-1-piperidinyloxy-mediated free-radical polymerization of acrylonitrile. *J Polym Sci Part A: Polym Chem* 2006;44:914–27.
- [163] Debigneau A, Michaux C, Jérôme C, Jérôme R, Poli R, Detrembleur C. Cobalt-mediated radical polymerization of acrylonitrile: kinetics investigations and DFT calculations. *Chem Eur J* 2008;14:7623–37.
- [164] Buchmeiser MR, Marino MG. Co(acac)₂-mediated radical polymerization of acrylonitrile: control over molecular weights and copolymerization with methyl methacrylate. *Macromol Mater Eng* 2012;297:894–901.
- [165] Acar MH, Matyjaszewski K. Block copolymers by transformation of living anionic polymerization into controlled/Living atom transfer radical polymerization. *Macromol Chem Phys* 1999;200:1094–100.
- [166] Chong BYK, Ercole F, Moad G, Rizzardo E, Thang SH. Imidazolidinone Nitroxide-mediated Polymerization. *Macromol* 1999;32:6895–902.
- [167] Baumann M, Schmidt-Naake G. Acetic anhydride-accelerating agent for nitroxide-controlled free-radical copolymerization of styrene and acrylonitrile. *Macromol Chem Phys* 2001;202:2727–31.
- [168] Taube C, Schmidt-Naake G. TEMPO-controlled radical suspension polymerization in oil/water system in and autoclave. *Chem Eng Technol* 2001;10:1013–7.
- [169] Tsarevsky NV, Sarbu T, Gobelt B, Matyjaszewski K. Synthesis of styrene-acrylonitrile copolymers and related block copolymers by atom transfer radical polymerization. *Macromolecules* 2002;35:6142–8.
- [170] Consolante V, Maric M, Penlidis A. Routes to carboxylic acid functional acrylonitrile copolymers via N-tert-butyl-N-(1-diethylphosphono-2,2-dimethylpropyl) free nitroxide based nitroxide-mediated polymerization. *J Appl Polym Sci* 2012;125:3963–76.
- [171] Wang GX, Lu M, Hou ZH, Wu H. Reactivity ratios of controlled/living copolymerization of styrene and acrylonitrile in ionic liquid microemulsion. *J Polym Res* 2013;20(80):1–6.
- [172] Wu D, Dong H, Pietrasik J, Kim EK, Hui CM, Zhong M, et al. Novel nanoporous carbons from well-defined poly(styrene-co-acrylonitrile)-grafted silica nanoparticles. *Chem Mater* 2011;23:2024–6.
- [173] Spörli JM, Ota A, Beyer R, Lehr T, Müller A, Hermannutz F, et al. Carbon fibers prepared from tailored reversible-addition-fragmentation transfer copolymerization-derived poly(acrylonitrile)-co-poly(methylmethacrylate). *J Polym Sci Part A: Polym Chem* 2014;52:1322–33.
- [174] Brar AS, Saini T. Atom transfer radical copolymerization of acrylonitrile and ethyl methacrylate at ambient temperature. *J Polym Sci Part A: Polym Chem* 2006;44:1975–84.
- [175] Niu S, Ding M, Chen M, Feng T, Zhang L, Wei L, et al. Synthesis of well-defined copolymer of acrylonitrile and maleic anhydride via RAFT polymerization. *J Polym Sci Part A: Polym Chem* 2013;51:5263–9.
- [176] Nguyen-Thai NU, Hong SC. Controlled architectures of poly(acrylonitrile-co-itaconic acid) for efficient structural transformation into carbon materials. *Carbon* 2014;69:571–81.
- [177] Chernikova EV, Poteryaeva ZA, Plutalova AV. Controlled copolymerization of acrylonitrile in bulk via the reversible addition-fragmentation chain-transfer mechanism. *Polym Sci Ser B* 2014;56:109–17.
- [178] Chernikova EV, Kishilov SM, Plutalova AV, Kostina YV, Bondarenko GN, Baskakov AA, et al. Specific features of the copolymerization of acrylonitrile and acrylamide in the presence of low-molecular-mass and polymeric triethiocarbonates and properties of the obtained copolymers. *Polym Sci Ser B* 2014;56:553–65.
- [179] Moskowitz JD, Wiggins JS. Semibatch RAFT copolymerization of acrylonitrile and N-isopropylacrylamide: effect of comonomer distribution on cyclization and thermal stability. *Polymer* 2016;84:311–8.
- [180] Cai JV, McDonnell J, Brackley C, O'Brien L, Church JS, Millington K, et al. Polyacrylonitrile-based precursors and carbon fibers derived from advanced RAFT technology and conventional methods – the 1st comparative study. *Mater Today Commun* 2016;9:22–9.
- [181] Kaiser A, Brandau S, Klimpel M, Barner-Kowollik C. Acrylonitrile-butadiene rubber (NBR) prepared via living/controlled radical polymerization (RAFT). *Macromol Rapid Commun* 2010;31:1616–21.
- [182] Dürr CJ, Emmerling SGJ, Kaiser A, Brandau S, Habicht AKT, Klimpel M, et al. A Detailed investigation of the experimental conditions for the reversible addition fragmentation chain transfer-mediated copolymerization of acrylonitrile and butadiene. *J Polym Sci Part A: Polym Chem* 2012;50:174–80.
- [183] Dürr CJ, Halele L, Kaiser A, Brandau S, Barner-Kowollik C. Mild and efficient modular synthesis of poly(acrylonitrile-co-butadiene) block and miktoarm star copolymer architectures. *Macromolecules* 2013;46:49–62.
- [184] Keddie DJ. A guide to the synthesis of block copolymers using reversible-addition fragmentation chain transfer (RAFT) polymerization. *Chem Soc Rev* 2014;43:496–505.
- [185] Matyjaszewski K, Shipp DA, McMurtry GP, Gaynor SG, Pakula T. Simple and effective one-pot synthesis of (Meth)acrylic block copolymers through atom transfer radical polymerization. *J Polym Sci Part A: Polym Chem* 2000;38:2023–31.
- [186] Matyjaszewski K, Shipp DA, Wang J, Grimaud T, Patten TE. Utilizing halide exchange to improve control of atom transfer radical polymerization. *Macromolecules* 1998;31:6836–40.
- [187] Shipp DA, Wang J, Matyjaszewski K. Synthesis of acrylate and methacrylate block copolymers using atom transfer radical polymerization. *Macromolecules* 1998;31:8005–8.
- [188] Peng CH, Kong J, Seeliger F, Matyjaszewski K. Mechanism of halogen exchange in ATRP. *Macromolecules* 2011;44:7546–57.
- [189] Lin Y, Wang X, Qian G, Watkins JJ. Additive-driven self-assembly of well-ordered mesoporous carbon/iron oxide nanoparticle composites for supercapacitors. *Chem Mater* 2014;26:2128–37.
- [190] Brar AS, Saini T. Atom transfer radical polymerization of 2-methoxy ethyl acrylate and its block copolymerization with acrylonitrile. *Eur Polym J* 2007;43:1046–54.
- [191] Nguyen CT, Kim DP. Direct preparation of mesoporous carbon by pyrolysis of poly(acrylonitrile-b-methylmethacrylate) diblock copolymer. *J Mater Chem* 2011;21:14226–30.
- [192] Yan K, Kong LB, Dai YH, Shi M, Shen KW, Hu B, et al. Design and preparation of highly structure-controllable mesoporous carbons at the molecular level and their application as electrode materials for supercapacitors. *J Mater Chem A Mater Energy Sustain* 2015;3:22781–93.
- [193] Yan K, Kong LB, Shen KW, Dai YH, Shi M, Hu B, et al. Facile preparation of nitrogen-doped hierarchical porous carbon with high performance in supercapacitors. *Appl Surf Sci* 2016;364:850–61.
- [194] Moad G. Mechanism and kinetics of dithiobenzoate-mediated RAFT polymerization – status of the dilemma. *Macromol Chem Phys* 2014;215:9–26.
- [195] Aqil A, Detrembleur C, Gilbert B, Jerome R, Jerome C. Controlled RAFT synthesis of Polyacrylonitrile-b-poly(acrylic acid) diblocks as precursors of carbon nanocapsules with assistance of gold nanoparticles. *Chem Mater* 2007;19:2150–4.
- [196] Oschmann B, Tahir MN, Mueller F, Bresser D, Lieberwirth I, Tremel W, et al. Precursor polymers for the carbon coating of Au@ZnO multipods for application as active material in lithium-ion batteries. *Macromol Rapid Commun* 2015;36:1075–82.
- [197] Wan L, Lei H, Ding Y, Fu L, Li J, Xu Z. Linear and comb-like acrylonitrile/n-isopropylacrylamide copolymers synthesized by the combination of RAFT polymerization and ATRP. *J Polym Sci Part A: Polym Chem* 2008;46:92–101.
- [198] Kruk M, Dufour B, Celer EB, Kowalewski T, Jaroniec M, Matyjaszewski K. Synthesis of mesoporous carbons using ordered and disordered mesoporous silica templates and polyacrylonitrile as carbon precursor. *J Phys Chem B* 2005;109:9216–25.
- [199] Kruk M, Kohlhaas KM, Dufour B, Celer EB, Jaroniec M, Matyjaszewski K, et al. Partially graphitic, high-surface-area mesoporous carbons from polyacrylonitrile templated by ordered and disordered mesoporous silicas. *Microporous Mesoporous Mater* 2007;102:178–87.
- [200] Kruk M, Dufour B, Celer EB, Kowalewski T, Jaroniec M, Matyjaszewski K. Grafting monodisperse polymer chains from concave surfaces of ordered mesoporous silicas. *Macromolecules* 2008;41:8584–91.
- [201] Cao L, Kruk M. Ordered arrays of hollow carbon nanospheres and nanotubes from polyacrylonitrile grafted on ordered mesoporous silicas using atom transfer radical polymerization. *Polymer* 2015;72:356–60.
- [202] Tang C, Bombalski L, Kruk M, Jaroniec M, Matyjaszewski K, Kowalewski T. Nanoporous carbon films from "Hairy" polyacrylonitrile-grafted colloidal silica nanoparticles. *Adv Mater* 2008;20:1516–22.
- [203] Wu D, Li Z, Zhong M, Kowalewski T, Matyjaszewski K. Templated synthesis of nitrogen-enriched nanoporous carbon materials from porogenic organic precursors prepared by ATRP. *Angew Chem Int Ed* 2014;53:3957–60.
- [204] Niu S, Zhang L, Wang N, Zhu J, Zhang W, Cheng Z, et al. Fabrication of magnetic nanofibers via surface-initiated RAFT polymerization and coaxial electrospinning. *React Funct Polym* 2013;73:1447–54.
- [205] Zhang X, Tay SW, Liu Z, Hong L. Restructure proton conducting channels by embedding starburst POSS-g-acrylonitrile oligomer in sulfonic perfluoro polymer matrix. *J Membr Sci* 2009;329:228–35.
- [206] Chen Y, He M, Wang C, Wei Y. A novel polyvinyltetrazole-grafted resin with high capacity for adsorption of Pb(ii), Cu(ii) and Cr(iii) ions from aqueous solutions. *J Mater Chem A Mater Energy Sustain* 2014;2:10444–53.
- [207] Yue Y, Zhang C, Tang Q, Mayes RT, Liao WP, Liao C, et al. A poly(acrylonitrile)-Functionalized porous aromatic framework synthesized by atom-transfer radical polymerization for the extraction of uranium from seawater. *Ind Eng Chem Res* 2016;55:4125–9.
- [208] Yue Y, Mayes RT, Kim J, Fulvio PF, Sun XG, Tsouris C, et al. Seawater uranium sorbents: preparation from a mesoporous copolymer initiator by atom-transfer radical polymerization. *Angew Chem Int Ed* 2013;52:13458–62.
- [209] Brown S, Yue Y, Kuo LJ, Mehio N, Li M, Gill G, et al. Uranium adsorbent fibers prepared by atom-transfer radical polymerization (ATRP) from poly(vinyl chloride)-co-chlorinated poly(vinyl chloride) (PVC-co-CPVC) Fiber. *Ind Eng Chem Res* 2016;55:4130–8.
- [210] Liu Z, Xu Z, Hu X, Gao C. Lyotropic liquid crystal of polyacrylonitrile-grafted graphene oxide and its assembled continuous strong nacre-mimetic fibers. *Macromolecules* 2013;46:6931–41.

- [211] Kyotani T, Sonobe N, Tomita A. Formation of highly orientated graphite from polyacrylonitrile by using a two-dimensional space between montmorillonite lamellae. *Nature* 1988;331:331–3.
- [212] Sonobe N, Kyotani T, Tomita A. Carbonization of polyacrylonitrile in a two-dimensional space between montmorillonite lamellae. *Carbon* 1988;26:573–8.
- [213] Sonobe N, Kyotani T, Hishiyama Y, Shiraishi M, Tomita A. Formation of highly oriented graphite from poly(acrylonitrile) prepared between the lamellae of montmorillonite. *J Phys Chem* 1988;92:7029–34.
- [214] Bates FS. Polymer-Polymer phase behavior. *Science* 1991;251:898–905.
- [215] Tang C. Nanostructured carbon prepared from well-defined polyacrylonitrile block copolymers: from synthesis and characterization to devices. PhD thesis. Pittsburgh PA: Carnegie Mellon University; 2006. p. 198.
- [216] Leibler L. Theory of microphase separation in block copolymers. *Macromolecules* 1980;13:1602–17.
- [217] Zhong M, Tang C, Kim EK, Kruck M, Celer EB, Jaroniec M, et al. Preparation of porous nanocarbons with tunable morphology and pore size from copolymer templated precursors. *Mater Horiz* 2014;1:121–4.
- [218] Tang C, Tracz A, Kruck M, Zhang R, Smilgies D, Matyjaszewski K, et al. Long-range ordered thin films of BCP prepared by zone-casting. *J Am Chem Soc* 2005;127:6918–9.
- [219] Belanger JM, Penelle J, Russel TP. Synthesis and microphase separation of poly(styrene-b-acrylonitrile) prepared by sequential anionic and ATRP techniques. *Macromolecules* 2006;39:1766–70.
- [220] Ho R, Wang T, Lin C, Yu T. Mesoporous carbons from poly(acrylonitrile)-b-poly(E-caprolactone) block copolymers. *Macromolecules* 2007;40:2814–21.
- [221] Zhou Z, Liu G. Controlling the pore size of mesoporous carbon thin films through thermal and solvent annealing. *Small* 2017;13(1603107):1–9.
- [222] Tang C, Qi K, Wooley KL, Matyjaszewski K, Kowalewski T. Well-defined carbon nanoparticles prepared from water-soluble shell cross-linked micelles that contain polyacrylonitrile cores. *Angew Chem Int Ed* 2004;43:2783–7.
- [223] Lazzari M, Scalare D, Hoppe CE, Vazquez-Vazquez C, Lopez-Quintela MA. Tunable polyacrylonitrile-based micellar aggregates as a potential tool for the fabrication of carbon nanofibers. *Chem Mater* 2007;19:5818–20.
- [224] Lazzari M, Scalare D, Vazquez-Vazquez C, López-Quintela MA. Cylindrical micelles from the self-assembly of polyacrylonitrile-based diblock copolymers in nonpolar selective solvents. *Macromol Rapid Commun* 2008;29:352–7.
- [225] Tang C, Dufour B, Kowalewski T, Matyjaszewski K. Synthesis of molecular brushes with polyacrylonitrile block copolymer side chains and their conversion into nanostructured carbons. *Macromolecules* 2007;40:6199–205.
- [226] Chen S, Koshy DM, Tsao Y, Pfaffner R, Yan X, Feng D, et al. Highly tunable and facile synthesis of uniform carbon flower particles. *J Am Chem Soc* 2018;140:10297–304.
- [227] Wang Y, Serrano S, Santiago-Avilés JJ. Raman characterization of carbon nanofibers prepared using electrospinning. *Synth Met* 2003;138:423–7.
- [228] Gu SY, Ren J, Wu QL. Preparation and structures of electrospun PAN nanofibers as a precursor of carbon nanofibers. *Synth Met* 2005;155:157–61.
- [229] Zussman E, Chen X, Ding W, Calabri L, Dikin DA, Quintana JP, et al. Mechanical and structural characterization of electrospun PAN-derived carbon nanofibers. *Carbon* 2005;43:2175–85.
- [230] Kim C, Ngoc BTN, Yang KS, Kojima M, Kim YA, Kim YJ, et al. Self-sustained thin webs consisting of porous carbon nanofibers for supercapacitors via the electrospinning of polyacrylonitrile solutions containing zinc chloride. *Adv Mater* 2007;19:2341–6.
- [231] Jang J, Bae J. Fabrication of polymer nanofibers and carbon nanofibers by using a salt-assisted microemulsion polymerization. *Angew Chem Int Ed* 2004;43:3803–6.
- [232] Fernández-Saavedra R, Aranda P, Ruiz-Hitzky E. Templated synthesis of carbon nanofibers from polyacrylonitrile using sepiolite. *Adv Funct Mater* 2004;14:77–82.
- [233] Chen JT, Shin K, Leiston-Belanger JM, Zhang M, Russell TP. Amorphous carbon nanotubes with tunable properties via template wetting. *Adv Funct Mater* 2006;16:1476–80.
- [234] Thomassin JM, Debuigne A, Jérôme C, Detrembleur C. Design of mesoporous carbon fibers from a poly(acrylonitrile) based block copolymer by a simple templating compression moulding process. *Polymer* 2010;51:2965–71.
- [235] Hou H, Ge JJ, Zeng J, Li Q, Reneker DH, Greiner A, et al. Electrospun polyacrylonitrile nanofibers containing a high concentration of well-aligned multiwall carbon nanotubes. *Chem Mater* 2005;17:967–73.
- [236] Ryu S, Lee C, Park J, Lee JS, Kang S, Seo YD, et al. Three-dimensional scaffolds of carbonized polyacrylonitrile for bone tissue regeneration. *Angew Chem Int Ed* 2014;53:9213–7.
- [237] Marsh H, Rodríguez-Reinoso F. Activated carbon. Oxford: Elsevier Science Ltd; 2006. p. 13–86.
- [238] Ryoo R, Joo SH, Jun S. Synthesis of highly ordered carbon molecular sieves via template-mediated structural transformation. *J Phys Chem B* 1999;103:7743–6.
- [239] Lee J, Yoon S, Hyeon T, Oha SM, Kimb KB. Synthesis of a New Mesoporous Carbon and its application to electrochemical double-layer capacitors. *Chem Commun* 1999;2177–8.
- [240] Jun S, Joo SH, Ryoo R, Kruck M, Jaroniec M, Liu Z, et al. Synthesis of new, nanoporous carbon with hexagonally ordered mesostructure. *J Am Chem Soc* 2000;122:10712–3.
- [241] Joo SH, Choi SJ, Oh I, Kwak J, Liu Z, Terasaki O, et al. Ordered nanoporous arrays of carbon supporting high dispersions of platinum nanoparticles. *Nature* 2001;412:169–72.
- [242] Lee J, Kim J, Hyeon T. Recent progress in the synthesis of porous carbon materials. *Adv Mater* 2006;18:2073–94.
- [243] Lu A, Kiefer A, Schmidt W, Schuth F. Synthesis of polyacrylonitrile-based ordered mesoporous carbon with tunable pore structures. *Chem Mater* 2004;16:100–3.
- [244] Jang J, Lim B, Choi M. A simple synthesis of mesoporous carbons with tunable mesopores using a colloidal template-mediated vapor deposition polymerization. *Chem Commun* 2005;4214–6.
- [245] Zhang J, Song Y, Zhao Y, Zhao S, Yan J, Lee J, et al. Organosilica with grafted polyacrylonitrile brushes for high surface area nitrogen-enriched nanoporous carbons. *Chem Mater* 2018;30:2208–12.
- [246] Chang Y, Hong F, Liu J, Xie M, Zhang Q, He C, et al. Nitrogen/sulfur dual-doped mesoporous carbon with controllable morphology as a catalyst support for the methanol oxidation reaction. *Carbon* 2015;87:424–33.
- [247] Kruck M, Dufour B, Celer EB, Kowalewski T, Jaroniec M, Matyjaszewski K. Well-defined poly(ethylene oxide)-polyacrylonitrile diblock copolymers as templates for mesoporous silicas and precursors for mesoporous carbons. *Chem Mater* 2006;18:1417–24.
- [248] Stefk M, Lee J, Wiesner U. Nanostructured carbon-crystalline titania composites from microphase separation of poly(ethylene oxide-b-acrylonitrile) and titania sols. *Chem Commun* 2009;2532–4.
- [249] Stefk M, Sai H, Sauer K, Gruner SM, DiSalvo FJ, Wiesner U. Three-component porous-carbon-titania nanocomposites through self-assembly of ABCBA block terpolymers with titania sols. *Macromolecules* 2009;42:6682–7.
- [250] Zhang J, Song Y, Kopeć M, Lee J, Wang Z, Liu S, et al. Facile aqueous route to nitrogen-doped mesoporous carbons. *J Am Chem Soc* 2017;139:12931–4.
- [251] Kruck M, Tang C, Dufour B, Matyjaszewski K, Kowalewski T. Nanostructured carbons from block copolymers. In: Lazzari M, Liu G, Lecommandoux S, editors. *Block copolymers in nanoscience*. Weinheim, Germany: Wiley; 2006. p. 233–5.
- [252] McGann JP, Zhong M, Kim EK, Natesakhawat S, Jaroniec M, Whitacre JF, et al. Block copolymer templating as a path to porous nanostructured carbons with highly accessible nitrogens for enhanced (Electro)chemical performance. *Macromol Chem Phys* 2012;213:1078–90.
- [253] Zhong M, Kim EK, McGann JP, Chun SE, Whitacre JF, Jaroniec M, et al. Electrochemically active nitrogen-enriched nanocarbons with well-defined morphology synthesized by pyrolysis of self-assembled block copolymer. *J Am Chem Soc* 2012;134:14846–57.
- [254] Yuan R, Wang H, Gottlieb E, Sun M, Kopeć M, Wang Z, Li S, Whitacre J, Matyjaszewski K, Kowalewski T. Well-Controlled N/S Co-Doped Nanocarbons from Sulfurized PAN-b-PBA Block Copolymers for Supercapacitors. unpublished 2018 n/a.
- [255] Kashiwagi T, Hirata T, Brown JE. Thermal and oxidative degradation of poly(methyl methacrylate): molecular weight. *Macromolecules* 1985;18:131–8.
- [256] Rahaman MSA, Ismail AF, Mustafa A. A review of heat treatment on polyacrylonitrile fiber. *Polym Degrad Stab* 2007;92:1421–32.
- [257] Yuan R, Kopeć M, Xie G, Gottlieb E, Mohin JW, Wang Z, et al. Mesoporous nitrogen-doped carbons from PAN-based molecular bottlebrushes. *Polymer* 2017;126:352–9.
- [258] Conway BE. *Electrochemical supercapacitors: scientific fundamentals and technological applications*. Boston, MA: Springer US; 1999. p. 698.
- [259] Frackowiak E. Carbon materials for supercapacitor application. *Phys Chem Chem Phys* 2007;9:1774–85.
- [260] Pels JR, Kapteijn F, Moulijn JA, Zhu Q, Thomas KM. Evolution of nitrogen functionalities in carbonaceous materials during pyrolysis. *Carbon* 1995;33:1641–53.
- [261] Yang X, Wu D, Chen X, Fu R. Nitrogen-enriched nanocarbons with a 3-D continuous mesopore structure from PAN for supercapacitor. *J Phys Chem C* 2010;114:8581–6.
- [262] Ju MJ, Choi IT, Zhong M, Lim K, Ko J, Mohin J, et al. Copolymer-templated nitrogen-enriched nanocarbons as a low charge-transfer resistance and highly stable alternative to platinum cathodes in dye-sensitized solar cells. *J Mater Chem A* 2015;3:4413–9.
- [263] Wang Y, Fugetsu B, Wang Z, Gong W, Sakata I, Morimoto S, et al. Nitrogen-doped porous carbon monoliths from polyacrylonitrile (PAN) and carbon nanotubes as electrodes for supercapacitors. *Sci Rep* 2017;7(40259):1–11.
- [264] Kim BH, Yang KS, Ferraris JP. Highly conductive, mesoporous carbon nanofiber web as electrode material for high-performance supercapacitors. *Electrochim Acta* 2012;75:325–31.
- [265] Tran C, Kalra V. Fabrication of porous carbon nanofibers with adjustable pore sizes as electrodes for supercapacitors. *J Power Sources* 2013;235:289–96.
- [266] Huang K, Li M, Chen Z, Yao Y, Yang X. Nitrogen-enriched porous carbon nanofiber networks for binder-free supercapacitors obtained by using a reactive surfactant as a porogen. *Electrochim Acta* 2015;158:306–13.
- [267] Huang K, Yao Y, Yang X, Chen Z, Li M. Fabrication of flexible hierarchical porous nitrogen-doped carbon nanofiber films for application in binder-free supercapacitors. *Mater Chem Phys* 2016;169:1–5.

- [268] Yan X, Yu Y, Ryu SK, Lan J, Jia X, Yang X. Simple and scalable synthesis of phosphorus and nitrogen enriched porous carbons with high volumetric capacitance. *Electrochim Acta* 2014;136:466–72.
- [269] Gottlieb E, Matyjaszewski K, Kowalewski T. Polymer-based synthetic routes to carbon-based metal-free catalysts. *Adv Mater* 2018, 00:1804626/1–16.
- [270] Ma L, Hendrickson KE, Wei SY, Archer LA. Nanomaterials: science and applications in the lithium-sulfur battery. *Nano Today* 2015;10:315–38.
- [271] Manthiram A, Fu Y, Chung SH, Zu C, Su YS. Rechargeable Lithium-Sulfur batteries. *Chem Rev* 2014;114:11751–87.
- [272] Wang JL, Yang J, Xie JY, Xu NX. A novel conductive polymer-sulfur composite cathode material for rechargeable lithium batteries. *Adv Mater* 2002;14:963–5.
- [273] Wang JL, Yang J, Wan CR, Du K, Xie JY, Xu NX. Sulfur composite cathode materials for rechargeable lithium batteries. *Adv Funct Mater* 2003;13:487–92.
- [274] Yu XG, Xie JY, Yang J, Huang HJ, Wang K, Wen ZS. Lithium storage in conductive sulfur-containing polymers. *J Electroanal Chem* 2004;573:121–8.
- [275] Fanous J, Wegner M, Grimminger J, Andresen A, Buchmeiser MR. Structure-related electrochemistry of sulfur-poly(acrylonitrile) composite cathode materials for rechargeable lithium batteries. *Chem Mater* 2011;23:5024–8.
- [276] Fanous J, Wegner M, Grimminger J, Rolff M, Spera MBM, Tenzer M, et al. Correlation of the electrochemistry of poly(acrylonitrile)-sulfur composite cathodes with their molecular structure. *J Mater Chem* 2012;22:23240–5.
- [277] Fanous J, Wegner M, Spera MBM, Buchmeiser MR. High energy density poly(acrylonitrile)-sulfur composite-based lithium-sulfur batteries. *J Electrochem Soc* 2013;160:A1169–70.
- [278] Wei SY, Ma L, Hendrickson KE, Tu ZY, Archer LA. Metal-sulfur battery cathodes based on PAN sulfur composites. *J Am Chem Soc* 2015;137:12143–52.
- [279] Wang L, He XM, Sun WT, Li JJ, Gao J, Tian GY, et al. Organic polymer material with a multi-electron process redox reaction: towards ultra-high reversible lithium storage capacity. *RSC Adv* 2013;3:3227–31.
- [280] Guo JC, Yang ZC, Yu YC, Abruna HD, Archer LA. Lithium-sulfur battery cathode enabled by lithium-nitrile interaction. *J Am Chem Soc* 2013;135:763–7.
- [281] Yin LC, Wang JL, Yang J, Nuli YN. A novel pyrolyzed polyacrylonitrile-sulfur@MWCNT composite cathode material for high-rate rechargeable lithium/sulfur batteries. *J Mater Chem* 2011;21:6807–10.
- [282] Yin LC, Wang JL, Lin FJ, Yang J, Nuli Y. Polyacrylonitrile/graphene composite as a precursor to a sulfur-based cathode material for high-rate rechargeable Li-S batteries. *Energy Environ Sci* 2012;5:6966–72.
- [283] Li Q, Liu M, Qin XY, Wu JX, Han WJ, Liang GM, et al. Cyclized-polyacrylonitrile modified carbon nanofiber interlayers enabling strong trapping of polysulfides in lithium-sulfur batteries. *J Mater Chem A* 2016;4:12973–80.
- [284] Frey M, Zenn RK, Warneke S, Müller K, Hintennach A, Dinnebier RE, et al. Easily accessible, textile fiber-based sulfurized poly(acrylonitrile) as Li/S cathode material: correlating electrochemical performance with morphology and structure. *ACS Energy Lett* 2017;2:595–604.
- [285] Zhu J, Chen C, Lu Y, Zang J, Jiang M, Kim D, et al. Highly porous polyacrylonitrile/graphene oxide membrane separator exhibiting excellent anti-self-discharge feature for high-performance lithium-sulfur batteries. *Carbon* 2016;101:272–80.
- [286] Huang X, Zhao Z, Cao L, Chen Y, Zhu E, Lin Z, et al. High-performance transition metal-doped Pt3Ni octahedra for oxygen reduction reaction. *Science* 2015;348:1230–4.
- [287] Li M, Zhao Z, Cheng T, Fortunelli A, Chen CY, Yu R, et al. Ultrafine jagged platinum nanowires enable ultrahigh mass activity for the oxygen reduction reaction. *Science* 2016;354:1414–9.
- [288] Bu L, Zhang N, Guo S, Zhang X, Li J, Yao J, et al. Biaxially strained PtPb/Pt core/shell nanoplate boosts oxygen reduction catalysis. *Science* 2016;354:1410–4.
- [289] Nie Y, Li L, Wei Z. Recent advancements in Pt and Pt-free catalysts for oxygen reduction reaction. *Chem Soc Rev* 2015;44:2168–201.
- [290] Seh ZW, Kibsgaard J, Dickens CF, Chorkendorff I, Nørskov JK, Jaramillo TF. Combining theory and experiment in electrocatalysis: insights into materials design. *Science* 2017, 355:eaad4998/1–14.
- [291] Zhou R, Zheng Y, Jaroniec M, Qiao SZ. Determination of the Electron transfer number for the oxygen reduction reaction: from theory to experiment. *ACS Catal* 2016;6:4720–8.
- [292] Gupta S, Tryk D, Bae I, Aldred W, Yeager E. Heat-treated polyacrylonitrile-based catalysts for oxygen electroreduction. *J Appl Electrochem* 1989;19:19–27.
- [293] Ohms D, Herzog S, Franke R, Neumann V, Wiesener K, Gamburcev S, et al. Influence of metal ions on the electrocatalytic oxygen reduction of carbon materials prepared from pyrolyzed polyacrylonitrile. *J Power Sources* 1992;38:327–34.
- [294] Ye S, Vijih AK, Dao LH. A new fuel cell electrocatalyst based on highly porous carbonized polyacrylonitrile foam with very low platinum loading. *J Electrochem Soc* 1996;143:L7–9.
- [295] Zhong M, Jiang S, Tang Y, Gottlieb E, Kim EK, Star A, et al. Block copolymer-templated nitrogen-enriched nanocarbons with morphology-dependent electrocatalytic activity for oxygen reduction. *Chem Sci* 2014;5:3315–9.
- [296] Wang L, Ambrosi A, Pumera M. Metal-free catalytic oxygen reduction reaction on heteroatom-doped graphene is caused by trace metal impurities. *Angew Chem Int Ed* 2013;52:13818–21.
- [297] Masa J, Xia W, Muhler M, Schuhmann W. On the role of metals in nitrogen-doped carbon electrocatalysts for oxygen reduction. *Angew Chem Int Ed* 2015;54:10102–20.
- [298] Vesborg PCK, Seger B, Chorkendorff I. Recent development in hydrogen evolution reaction catalysts and their practical implementation. *J Phys Chem Lett* 2015;6:951–7.
- [299] Conway BE, Tilak BV. Interfacial processes involving electrocatalytic evolution and oxidation of H₂, and the role of chemisorbed H. *Electrochim Acta* 2002;47:3571–94.
- [300] Gottlieb E, Kopeć M, Banerjee M, Mohin J, Yaron D, Matyjaszewski K, et al. In-situ platinum deposition on nitrogen-doped carbon films as a source of catalytic activity in a hydrogen evolution reaction. *ACS Appl Mater Interfaces* 2016;8:21531–8.
- [301] Duan J, Chen S, Jaroniec M, Qiao SZ. Porous C₃N₄ nanolayers@N-Graphene films as catalyst electrodes for highly efficient hydrogen evolution. *ACS Nano* 2015;9:931–40.
- [302] Davis SJ, Caldeira K, Matthews HD. Future CO₂ emissions and climate change from existing energy infrastructure. *Science* 2010;329:1330–3.
- [303] Zhong M, Natesakhawat S, Baltrus JP, Luebke D, Nulwala H, Matyjaszewski K, et al. Copolymer-templated nitrogen-enriched porous nanocarbons for CO₂ capture. *Chem Commun* 2012;48:11516–8.
- [304] Adeniran B, Mokaya R. Is N-doping in porous carbons beneficial for CO₂ storage? Experimental demonstration of the relative effects of pore size and N-doping. *Chem Mater* 2016;28:994–1001.
- [305] Song Y, Wei G, Kopeć M, Rao L, Zhang Z, Gottlieb E, et al. Copolymer-templated synthesis of nitrogen-doped mesoporous carbons for enhanced adsorption of hexavalent chromium and uranium. *ACS Appl Nano Mater* 2018;1:2536–43.